



Development and optimization of a formable sandwich sheet

Camille Besse

► To cite this version:

Camille Besse. Development and optimization of a formable sandwich sheet. Materials and structures in mechanics [physics.class-ph]. Ecole Polytechnique X, 2012. English. NNT: . tel-00691246

HAL Id: tel-00691246

<https://pastel.archives-ouvertes.fr/tel-00691246>

Submitted on 25 Apr 2012

HAL is a multi-disciplinary open access archive for the deposit and dissemination of scientific research documents, whether they are published or not. The documents may come from teaching and research institutions in France or abroad, or from public or private research centers.

L'archive ouverte pluridisciplinaire **HAL**, est destinée au dépôt et à la diffusion de documents scientifiques de niveau recherche, publiés ou non, émanant des établissements d'enseignement et de recherche français ou étrangers, des laboratoires publics ou privés.

DEVELOPMENT AND OPTIMIZATION OF A FORMABLE SANDWICH SHEET

Thèse présentée pour l'obtention du titre de
DOCTEUR DE L'ÉCOLE POLYTECHNIQUE
Spécialité : Mécanique

par

Camille Besse

Soutenue le 6 avril 2012 devant le jury composé de

Vincent GROLLEAU
Geneviève INGLEBERT
Gérard GARY
Dirk MOHR
Nicolas AUFRAY

Président - Rapporteur
Rapporteur
Directeur de thèse
Co-directeur de thèse
Examineur

Abstract

This thesis investigates the mechanical behavior of a new type of formable all-metal bi-directionally corrugated sandwich sheet material. Unlike conventional flat sandwich panel materials, this type of sandwich sheet material can be formed into three-dimensional shapes using traditional sheet metal forming techniques. In a first step, the core structure geometry is optimized such as to offer the highest shear stiffness-to-weight ratio. The post yielding behavior of the “optimal” sandwich structure is investigated using finite elements simulations of multi-axial experiments. A phenomenological constitutive model is proposed using an associative flow rule and distortional hardening. An inverse procedure is outlined to describe the sandwich material model parameter identification based on uniaxial tension and four-point bending experiments. In addition, simulations of a draw bending experiment are performed using a detailed finite element model as a well as a computationally-efficient composite shell element model. Good agreement of both simulations is observed for different forming tool geometries which is seen as a partial validation of the proposed constitutive model.

Contents

CONTENTS	I
LIST OF FIGURES	IV
LIST OF TABLES	VII
INTRODUCTION	1
Existing core structures	2
Forming of sandwich panels	4
Modeling the behavior of cellular solids	5
Overview of the thesis	6
CHAPTER I : DESCRIPTION AND MODEL OF THE BI-DIRECTIONALLY CORRUGATED SANDWICH STRUCTURE.....	9
1.1. The bi-directionally corrugated core structure	10
1.1.1 Core architecture and stamping tool.....	10
1.1.2 Basis material	11
1.2. Stamping experiments	13
1.2.1 Experimental set-up.....	13
1.2.2 Experimental results	14
1.3. Computational models for “virtual experiments”	16
1.3.1 Important modeling assumptions	16
1.3.2 Manufacturing simulations.....	18
1.1.1.1. Stamping.....	18
1.1.1.2. Forming of the bonding land, springback and joining of the core layers and face sheets.....	19
CHAPTER II : OPTIMIZATION OF THE EFFECTIVE SHEAR PROPERTIES OF THE BI- DIRECTIONALLY CORRUGATED SANDWICH CORE STRUCTURE.....	22
2.1. Estimation of the effective shear stiffness	23
2.2. Parametric study of the effective shear stiffness	24
2.2.1 Input parameters	24
2.2.2 Results	25
2.2.2 Comment on the optimal design of formable sandwich sheets	32

2.3. Experimental validation.....	33
2.3.1 Four-point bending experiment.....	34
2.3.2 Model for the bending of the sandwich structure.....	35
2.4. Conclusions	37
CHAPTER III : PLASTICITY OF FORMABLE ALL-METAL SANDWICH SHEETS: VIRTUAL EXPERIMENTS AND CONSTITUTIVE MODELING	39
3.1. Models for virtual experiments.....	40
3.1.1 Out-of-plane compression	40
3.1.2 Out-of-plane shear.....	41
3.1.3 Uniaxial in-plane loading	42
3.1.4 Combined in-plane loading	44
3.2. Results from virtual experiments.....	45
3.2.1 Uniaxial out-of plane compression	45
3.2.2 Out-of-plane shear.....	45
3.2.3 Uniaxial in-plane tension	48
3.2.4 Uniaxial in-plane compression.....	50
3.2.5 Biaxial in-plane behavior	51
3.2.6 Volume change of core structure	53
3.3. Phenomenological macroscopic constitutive model.....	56
3.3.1 Modeling approach.....	56
3.3.2 Notation and kinematics.....	56
3.3.3 Elastic constitutive equation.....	56
3.3.4 Macroscopic yield surface.....	57
3.3.5 Distortional-isotropic hardening	59
3.3.6 Flow rule and volume change	60
3.3.7 Summary of material model parameters	63
3.4. Validation and discussion.....	65
3.4.1 Comparison: macroscopic model versus virtual experiments.....	65
3.4.2 Discussion	66
3.5. Conclusions	67
CHAPTER IV : MODEL PARAMETER IDENTIFICATION AND APPLICATION TO DRAW BENDING.....	70
4.1. Calibration experiments.....	71
4.1.1 Calibration experiment #1: Uniaxial tension	71

4.1.2	Calibration experiment #2: Four-point bending	71
4.2.	Material model parameter identification	73
4.2.1	Summary of material model parameters	73
4.2.2	Elastic constants and thickness change parameter	73
4.2.3	Isotropic-distortional hardening functions	74
4.2.4	Composite shell element models.....	76
4.2.4.1.	Shell model for uniaxial tension	76
4.2.4.2.	Shell element model for four-point bending.....	76
4.2.5	Inverse model parameter identification.....	78
4.3.	Structural validation: draw bending	80
4.3.1	Virtual experiment.....	80
4.3.2	Composite shell model predictions and discussion.....	82
4.4.	Conclusions	83
CONCLUSION		85
FUTURE WORK		87
JOURNAL PUBLICATIONS RELATED TO THIS WORK		88
REFERENCES.....		90

List of Figures

Fig. 1 : Sandwich structures.	1
Fig. 2 : Photographs of (a) aluminum honeycomb structure, (b) aluminum foam (Baumeister et al, 1997), (c) sandwich structure with aluminum alloy truss core (Deshpande et al,2001), (d) aluminum eggbox structure (Zupan et al, 2003).....	3
Fig. 3 : Experiment of bi-directional draw bending of a sandwich prototype.....	7
Fig. 1.1 : (a) Side view of the four layer sandwich structure, (b) top view of a single core layer.	10
Fig. 1.2 : Engineering stress-strain curves for the 0.2mm thick low carbon steel sheet for. loading along different in-plane directions.....	12
Fig. 1.3 : (a) Photograph of the stamping tool comprising a male die (part 1) and a female die (part 2); (b) side view of before stamping,	14
Fig. 1.4 : Stamping pressure versus displacement.....	15
Fig. 1.5 : Side view of a single corrugated layer: comparison of the computed geometry .. (top) with a scanning electron micrograph of a prototype (bottom).....	15
Fig. 1.6 : The manufacturing steps.	17
Fig. 1.7 : Sequence of computed geometries during the stamping of a unit cell of a single core layer.	19
Fig. 2.1 : Unit cell model of the sandwich structure for estimating the transverse shear stiffness.	23
Fig. 2.2 : (a) Macroscopic shear modulus as a function of the height-to-thickness ratio αh ; the black crosses represents the simulation results for different stamping tool geometries; (b) cross-sectional views of four selected geometries. The numbered labels indicate the corresponding data points in (a).	27
Fig. 2.3 : Optimal configurations for different values of each αh	30
Fig. 2.4 : Influence of the parameters αD and αd on the elastic shear modulus.....	31
Fig. 2.5 : Elastic shear modulus as a function of the relative density for the proposed core structure (solid lines) and hexagonal honeycomb (dashed lines). Note that the shear modulus of the proposed material is the same for both in-plane directions, while the honeycomb stiffness is direction dependent.	32
Fig. 2.6 : Shear-lap test experiment specimen.....	33
Fig. 2.7 : Four-point bending of wide sandwich beams: (a) photograph of the experimental set-up, (b) schematic of the finite element model. The detail depicts a small portion of the deformed finite element mesh.	36
Fig. 3.1 : The colored dashed lines mark the boundary of the unit cell used for selected virtual experiments.	40

Fig. 3.2 : Illustration of the displacement boundary conditions for uniaxial tension (a) in the L-direction and (b) in the W-direction.	44
Fig. 3.3 : Out-of-plane compression: (a) macroscopic engineering stress-strain curve; (b) deformed configurations corresponding to the points labeled in the stress-strain curve.....	46
Fig. 3.4 : Out-of-plane shear: (a) macroscopic engineering shear stress-strain curves; (b) side views of deformed configurations corresponding to the points labeled in the stress-strain curves.	47
Fig. 3.5 : Uniaxial in-plane tension: engineering stress-strain curves for (a) entire sandwich cross-section, (b) the core structure, and (c) the face sheets; (d) 3D views of the deformed configurations corresponding to the points labeled in the stress-strain curves.	48
Fig. 3.6 : (a) Decomposition of the section force (per unit width) for uniaxial tension along the L-direction into the contributions of the core structure (black) and the face sheets (red); (b) Engineering strain along the width direction as a function of the axial engineering strain for uniaxial tension along the L- and W-directions.	49
Fig. 3.7 : Uniaxial in-plane compression: engineering stress-strain curves for (a) entire sandwich cross-section, (b) the core structure, and (c) the face sheets; (d) 3D views of the deformed configurations corresponding to the points labeled in the stress-strain curves.	51
Fig. 3.8 : Biaxial in-plane loading: (a) Engineering normal stress-strain curves for the L-direction (left column) and W-direction (right column) for the full sandwich cross-section (first row), the core structure (second row), and the face sheets (third row); the label β indicates the bi-axial loading angle; (b) 3D views of the deformed configurations corresponding to the points labeled in the stress-strain curves.	55
Fig. 3.9 : Plastic volume change during in-plane loading for all virtual experiments performed as a function of the plastic work per initial volume. The red dashed line shows the model approximation according to Eq. (3.23).	57
Fig. 3.10 : Envelopes of equal plastic work (per unit initial volume) for the face sheets in the true stress plane (σ_w, σ_L). The open dots present the results from virtual experiments, the black solid lines in (a) and (d) represent the least square fit of the yield function given by Eq. (3.16). The solid envelopes in (b) and (c) have been computed based on the isotropic-distortional hardening model given by Eq. (3.24).	61
Fig. 3.11 : Envelopes of equal plastic work (per unit initial volume) for the core structure in the true stress plane (σ_w, σ_L). The open dots present the results from virtual experiments, the black solid lines in (a) and (d) represent the least square fit of the yield function given by Eq. (3.16). The solid envelopes in (b) and (c) have been computed based on the isotropic-distortional hardening model given by Eq. (3.25).	62
Fig. 3.12 : Comparison of the force (per unit width) versus engineering strain curves for all virtual experiments. Different colors show the force for the entire sandwich section (blue), the face sheets (red) and the core structure (black). Dashed lines depict the results from virtual experiments, while the solid lines correspond to the macroscopic models.....	68

Figure 4.1 : Technical drawing of the experimental set-ups: (a) four-point bending experiment, (b) draw bending experiment.....	72
Figure 4.2 : (a) Stress-strain curves for the uniaxial tensile experiment (in black the “virtual” experiment results, in blue the model results) along with (b) the plastic volume change as a function of the plastic work density.	74
Figure 4.3 : (a) Force per unit width-displacement curves for the four-point bending experiment (in black the “virtual” experiment results, in blue the model results) along with (b) sequence of the “virtual” experiment.....	77
Figure 4.4 : Distortional hardenings function as a function of the plastic work per initial volume for the core structure (a) and the face sheet (b). Note that the curves start near the origin (0,0) since the plastic work densities W_{pl1} are almost zero (see Table 3.1).	79
Figure 4.5 : (a) Force per unit width-displacement curves for the draw bending experiments (in black the “virtual” experiment results, in blue the model results) along with (b) sequence of the first “virtual” experiment.....	81
Figure 4.6 : Draw bending of a prototype sandwich sheet demonstrating the formability of the sandwich sheet material.	83

List of Tables

Table 1.1 : Yield stress ratios.	13
Table 2.1 : Geometric parameters values.	25
Table 2.2 : Four point bending experiment results. K_1 and K_2 respectively the stiffness per unit width for the cylinders spacing b_1 and b_2	35
Table 3.1 : Yield function parameters.	64
Table 3.2 : Isotropic-distortional hardening function parameters	64
Table 4.1 : Calibrated hardening parameters.	78

Introduction

There is a constant pressure on the automotive industry to come up with lightweight structural solutions to improve vehicle fuel efficiency without sacrificing structural performance. In addition, the design choices are subject to stringent cost constraints as innovations in automotive engineering are seldom successful unless both performance and cost advantages prevail. Fiber-reinforced composite materials provide excellent weight-specific stiffness and strength properties, but their use is mostly limited to low volume production because of high production costs. Advanced high strength steels appear to be today's material of choice in automotive engineering as these feature a higher strength-to-weight ratio as conventional steels at a rather modest price premium. However, the stiffness of advanced high strength steels is the same as that of conventional steels. Thus, these materials do not provide a lightweight solution when the structural design is driven by stiffness requirements.

Sandwich structures are known for their exceptionally-high bending stiffness-to-weight ratio. The underlying design concept is the separation of two flat sheets by a much thicker core layer of low density (Fig. 1).

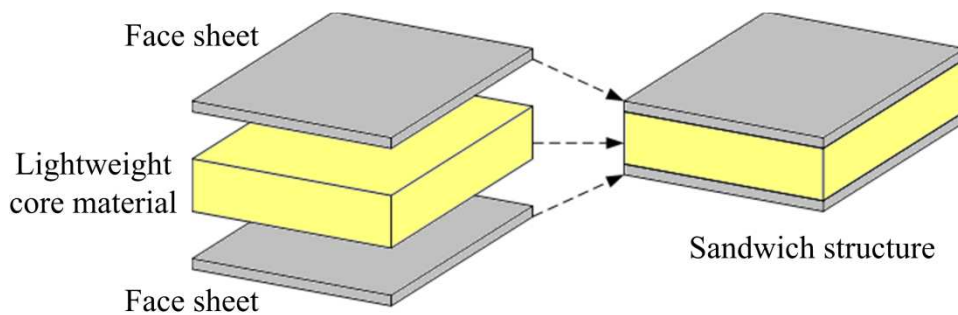


Fig. 1 : Sandwich structures.

Sheet metal and fiber reinforced plastics are typically chosen as face sheet materials, while the choice of the low density core layer material is far more complex. In addition to basic elastic and weight properties of the core layer, multi-functionality (e.g. thermal, acoustic

and energy absorption properties) as well as manufacturing considerations come into play (Evans et al., 1998).

Existing core structures

To satisfy the requirement of low density (as compared to the face sheet material) lightweight bulk materials such as balsa wood (Cantwell and Daview, 1996, Vural and Ravichandran, 2003) or polymers may be used directly in combination with steel or aluminum skins (Palkowski and Lange, 2007). As an alternative to low density bulk materials, man-made porous materials find wide spread use.

Hexagonal honeycombs (fig. 2a) are still the most widely used constructed sandwich core material. The elastic structure-property relationships for honeycombs are known for several decades (Kelsey et al., 1960; Gibson and Ashby, 1988) and most research on honeycombs focused on understanding and modeling their large deformation behavior (McFarland, 1960, Wierzbicki, 1983, Papka and Kyriakides, 1994, Mohr and Doyoyo, 2004). Kevlar reinforced paper honeycombs are widely used in aerospace and aeronautical engineering with aluminum or composite face sheets (Mahinfalah et al. 2007). All-aluminum honeycomb panels are employed in architectural applications. The manufacturing of metallic honeycomb structures involves several semi-manual steps (Bitzer, 1997, Wadley et al., 2003) and is hence not suitable for economic mass production.

Extensive research has been performed during the past two decades on the mechanical behavior of polymeric and metallic foams (fig. 2b) and their use in sandwich structures (Gibson and Ashby, 1988, Baumeister et al, 1997, Bart-Smith et al. 1998, 2001, Ashby et al., 2000, Bastawros et al., 2000, Dillard et al., 2005, Gong et al., 2005, Tan et al., 2005, Demiray, 2007, Ridhar and Shim, 2008, Luxner et al. 2009). However, their use in automotive applications is still inhibited by cost barriers as well as limited structural performance advantages.

More recent developments are concerned with truss core sandwich materials (fig. 2c) (Deshpande et al., 2001, Evans et al., 2001, Chiras et al. 2002, Liu and Lu, 2004, Queheillalt and Wadley, 2005, Mohr, 2005, Hutchinson and Fleck, 2006, Liu et al., 2006). Wicks and Hutchinson (2001) have shown that an optimized geometry of truss core will offer a sandwich structure comparable to honeycombs in terms of shear and bending strength-to-weight ratio

and comparable to hat-stiffened plate in term of compression strength-to-weight ratio. However, the performance advantages of truss core structures are mostly limited to small deformations. Under large deformations, the individual truss members lose their axial load carry capacity due to buckling (Gibson et al., 1997).

Egg-box structures (fig. 2d) present another type of architecture that can be used as core later for sandwich materials (Hale, 1960). Zupan et al (2003) investigated the through-thickness compression response of egg-box structures, focusing on the collapse of the structure by bending of the side walls. A comparison with metal foams revealed that egg-box panels present the best energy absorption properties. Tokura and Hagiwara (2010) investigated the stiffness and strength of a two-layer panel material. They made use of a multi-stage stamping technique to introduce a periodic array of domes of pyramidal shape and triangular base into initially flat sheets. After stamping, the layers are then joined together at the apexes of the pyramids through spot-welding. Tokura and Hagiwara (2010) found that it is critically important to account for local thickness changes and work hardening during stamping when estimating the bending strength of the two layer panel material.

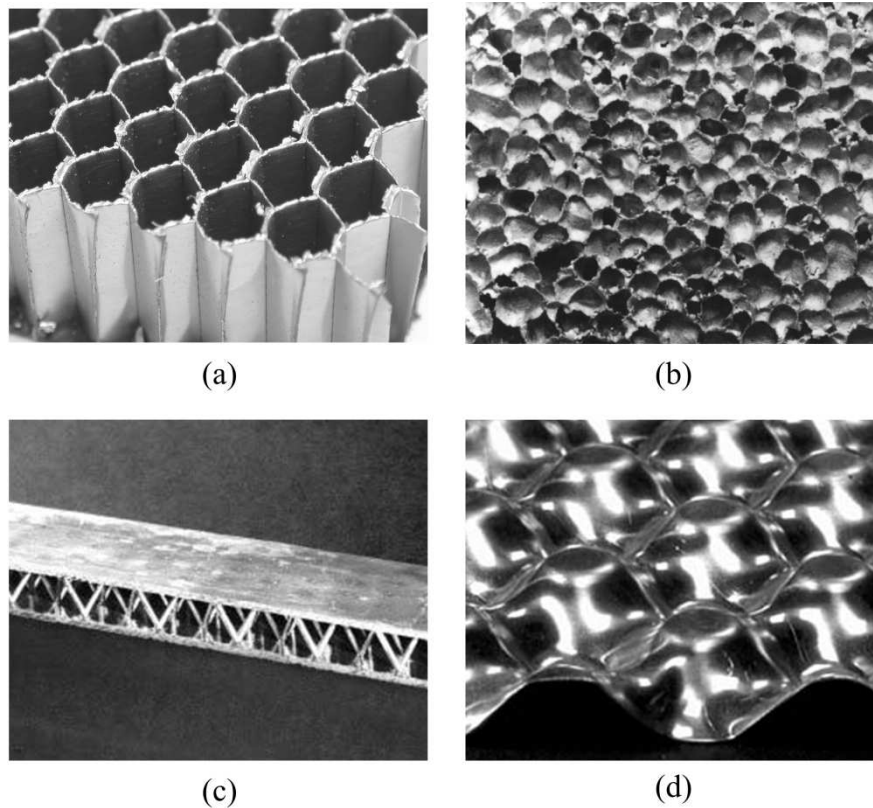


Fig. 2 : Photographs of (a) aluminum honeycomb structure, (b) aluminum foam (Baumeister et al, 1997), (c) sandwich structure with aluminum alloy truss core (Deshpande et al, 2001), (d) aluminum eggbox structure (Zupan et al, 2003)

Finally, folded cores are promising structures as new production means emerge. In particular, the chevron folded core has received interest for its impact energy absorption properties (Basily and Elsayed, 2004) or its transverse shear and compression behavior (Heimbs et al., 2006, Kintscher et al., 2007, Lebée et al, 2010).

Forming of sandwich panels

Sandwich structures with curved mid-planes are difficult to make. As a result, sandwich constructions are mostly limited to flat panel-type of structures reducing their scope of applications. In the automotive industry for instance, complex three-dimensional shapes are manufactured by converting flat blanks via various sheet metal forming operations. Thus, the development of a new formable sandwich sheet material that could be used with traditional sheet metal forming technology is of great interest.

There are two main approaches for forming sandwich structures into three-dimensional shapes: building the different component parts into the required shape and assemble them to create the sandwich (Blitzer, 2000), or forming the sandwich structure directly. Jackson et al. (2008), explored the applicability of incremental sheet forming to different type of sandwich panels with metal faces. Only the panels with a ductile and incompressible core, polymer cores, could survive the deformation introduced by the local indentations during the process. Numerous investigations were made on the forming of sandwich panels composed of metallic face sheets with a polymer core (Miller 1981, Pearce 1991, Kim et al. 2003, Carrado et al. 2006, Parsa et al. 2010). However, sandwich sheets with polymer cores cannot be welded, limiting their potential use in the automotive industry. Most research on the large deformation behavior of metallic sandwich plates focus on the response to three-point bending loadings (Bart-Smith 2001, Desphande et al. 2001, Rathbun 2004, Rubino et al. 2010, Valdevit et al. 2006). The main failure modes that are observed include face buckling, face thinning, core struts buckling, core shear failure and delamination.

Mohr and Straza (2005) showed that unlike conventional flat sandwich panels, sandwich sheets, with a thickness of about 2mm, can be formed into three-dimensional shapes using traditional sheet metal forming techniques such as stamping or draw bending. Mohr (2005) studied the formability of two different sandwich plates with stainless steel face sheets, with

stainless steel fibers and steel perforated cores. Deep drawing experiments and a detailed numerical and theoretical analysis of the bending and unbending behavior of the sandwich sheet revealed that cellular core structures of high relative density ($>20\%$) are required to withstand the high shear loads during forming.

With these results in mind, Seong et al. (2010) elaborated a design map to create a bendable all-metal sandwich structure with a sheared dimple core. They show that the core shear strength is increased as the gap between bonding points between the core and the face sheet decreases. An analytic investigation was performed on the suitable experimental set-up and geometric conditions for avoiding delamination failure during U-bending experiments on a welded sandwich plate (Seong et al. 2010). Seong et al. (2010) also investigated the bending response of sandwich sheets with adhesively bonded bi-directionally corrugated core layers. Considerations on the core geometry to avoid face sheet buckling were thought of to design an optimal sandwich sheet and carry on bending experiment.

The formability of two types of sandwich sheets with metal faces and stainless steel fiber cores have been established. Gustafsson (2000) proposed the Hybrid Stainless Steel Assembly (HSSA) where the core fibre are oriented perpendicular to the face sheets and are bonded by epoxy resin or rubber. Markaki and Clyne (2003) presented the Cambridge Bonded Steel Sheets (CAMBOSS) and the Cambridge Brazed Steel Sheets (CAMBASS) where the stainless steel fibers are arranged in a network with solid joints between contacting fibers in order to increase the shear stiffness and strength of the core material.

Modeling the behavior of cellular solids

Engineering design requires a good understanding of the material behavior in order to perform numerical simulations. When sandwich structures are involved, the numerical analysis is preferably performed, for numerical efficiency, in terms of effective properties rather than using a detailed model of the given microstructure. In other words, phenomenological macroscopic constitutive models are needed to describe the effective behavior of cellular materials with a complex microstructure.

Deshpande and Fleck (2000) developed an isotropic yield function for foams where the square of the mean stress is added to the square of the von Mises equivalent stress. They made use of an associated flow rule along with a stress-state dependant isotropic hardening law.

Xue and Hutchinson (2004) proposed an anisotropic constitutive model for metallic sandwich cores by adding three square normal stress terms to the Hill'48 equivalent stress definition. Note that similar to the physics-based Gurson (1977) model for porous metals, the phenomenological Deshpande-Fleck and Xue-Hutchinson models incorporate the effect of the mean stress on yield through even terms.

Based on the assumption that the effect of in-plane stresses may be neglected in sandwich structures, Mohr and Doyoyo (2004) proposed a non-associated plasticity model to describe the large deformation response of low density honeycombs. A generalized anisotropic plasticity model for sandwich plate cores has been presented by Xue et al. (2005). They normalized all stress tensor components to define an elliptical yield function (which is an even function of the stress tensor). Due to the normalization, it is easy to introduce yield surface shape changes (distortional hardening) in addition to isotropic hardening. Xue et al. (2005) also show extensive results from unit cell simulations which support the introduction of distortional hardening. Micromechanical models of truss-lattice materials (Mohr, 2005) and hexagonal honeycombs (Mohr, 2005b) explain distortional hardening at the macroscopic level through the evolution of the unit cell geometry as the material is subjected to finite strains. In sheet metal plasticity, changing Lankford coefficients which are an indicator for texture changes (e.g. Savoie, 1995) can be related to distortional hardening. A general kinematic-distortional hardening modeling framework can be found in Ortiz and Popov (1983). Aretz (2008) proposed a simple isotropic-distortional hardening model, where the shape coefficients of a non-quadratic plane stress yield surface (Aretz, 2004) are expressed as a function of the equivalent plastic strain. To account for the direction dependent strain hardening with constant r -values, Stoughton and Yoon (2009) made use of a non-associated flow rule and integrated four stress-strain functions to control the evolution of the shape and size of a Hill'48 yield criterion.

Overview of the thesis

The thesis investigates the mechanical behavior of an all-metal formable sandwich sheet material with a core structure composed of two bi-directionally corrugated steel layers. The core layers are composed of a periodic array of domes which are introduced into an initially flat sheet through stamping and brazed together to form a core structure. The core structure is thus

conceptually similar to that investigated by Tokura and Hagiwara (2010). In contrast to conventional egg-box structures, the contact areas between the core structure and the sandwich face sheets are ring shaped which reduces the risk of face sheet wrinkling or dimpling when the sandwich material is subject to bending. Figure 3 shows an illustration of the successful draw bending of a prototype made from this material.



Fig. 3 : Experiment of bi-directional draw bending of a sandwich prototype.

The thesis mainly focuses on:

- Presentation of this new sandwich sheet material along with simulations of the manufacturing of the core structure;
- Determination of the core structure geometry offering the highest shear stiffness-to-weight ratio;
- Understanding of the multi-axial loading response and development of a macroscopic phenomenological constitutive model of the sandwich structure;
- Identification of the material model parameters and structural validation for draw bending.

Chapter I : Description and Model of the Bi-directionally Corrugated Sandwich Structure

The great motivation of this thesis is the understanding of the behavior of a new type of formable all-metal sandwich sheet: the bi-directionally corrugated sandwich structure. However, it was not possible to carry on all the physical experiments required to have an overview of the sandwich behavior. Analytical analyses are also restricted by the complex shape of the core structure. As an alternative, and thanks to the periodic and symmetric nature of the core geometry, numerical simulations of a representative unit cell of the sandwich material are performed to investigate the effective behavior of the material under different loading conditions. These simulations are referred as “virtual” experiments.

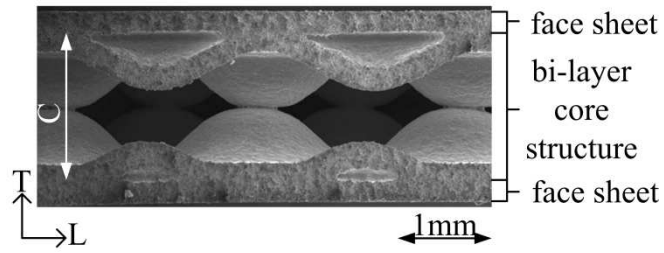
Predicting the effective behavior of cellular materials based on FE analysis of the underlying unit cell (for periodic media) has been successfully used by several research groups. For example, Mohr and Doyoyo (2004) investigated the crushing response of aluminum honeycomb using a detailed shell element model of the hexagonal cell structure; Youseff et al. (2005) built a finite element model of a PU foam based on X-ray tomography images; while Caty et al. (2008) developed a microstructural FE model of a sintered stainless steel sphere assembly (similar to closed-cell foam) based on X-ray tomography images. It is worth mentioning that the unit cell computations are only representative for the material behavior of the microstructures remain mechanically stable. In the case of instabilities (which are frequent in cellular materials of low relative density), a careful analysis of the type of instabilities is needed to check the validity of the homogenized material description (Triantafyllidis and Schraad, 1998).

This chapter starts by a detailed description of the physical core structure. Then, the finite-element model of a unit cell is presented. Since the exact geometry of the dimples of the bi-directionally corrugated core layers depends on the strain distribution after stamping, we perform numerical simulations of the all manufacturing process.

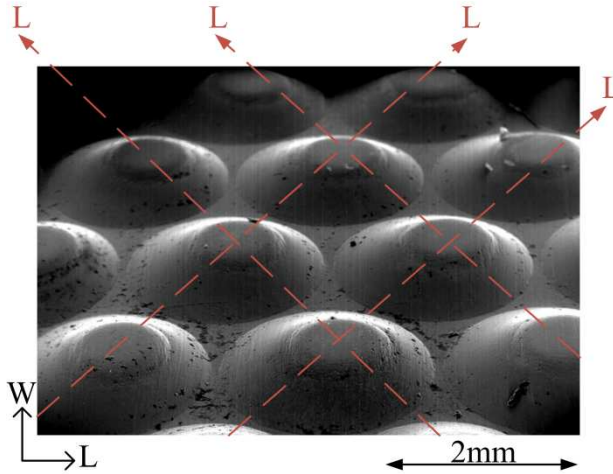
1.1. The bi-directionally corrugated core structure

1.1.1 Core architecture and stamping tool

The core architecture is made of two bi-directionally corrugated layers brazed together. Each layer is composed of a periodic array of domes (Fig. 1.1) which are introduced into an initially flat sheet through stamping.



(a)



(b)

Fig. 1.1 : (a) Side view of the four layer sandwich structure, (b) top view of a single core layer.

The material coordinate system ($\mathbf{e}_L, \mathbf{e}_W, \mathbf{e}_T$) as shown in Fig. 1.1 is introduced to describe the microstructure. The coordinate axis \mathbf{e}_T is aligned with the thickness direction of the sandwich sheet material (out-of-plane direction) whereas \mathbf{e}_W and \mathbf{e}_L denote the so-called in-plane directions. The L-direction is parallel to the connecting line of two neighboring domes while the W-direction is defined as $\mathbf{e}_W = \mathbf{e}_T \times \mathbf{e}_L$. The core structure features seven

symmetry planes; the bi-layer assembly is symmetric with respect to the central (W,L)– plane (Fig. 1.1). Furthermore, each layer is symmetric with respect to the (W,T)– and (L,T)– planes.

In the manufacturing process, we can control the geometry of the stamping tools, while the final geometry of a core layer after stamping depends also on the plastic properties of the basis sheet material. The stamping tool consists of a male and a female die. The male die comprises a periodic array of pins that are positioned on a triangular pattern at a spacing D (Fig. 1.3). All pins have the same diameter d_m and feature a corner radius r_m (Fig. 1.3). The receiving female die features the corresponding periodic array of holes of a diameter d_f along with a corner radius r_f (Fig.1.3).

The relative density ρ^* of the core structure describes the ratio of the overall mass density of the core structure to the density of the basis sheet material. In the case of incompressible sheet materials, the relative density is given by

$$\rho^* = \frac{2t}{C} \quad (1.1)$$

where t denotes the initial sheet thickness and $C/2$ is the effective height of a single core layer after stamping.

1.1.2 Basis material

The bi-layer core structure can be made of any sheet material that provides sufficient formability. Here, we focus on dimpled layers that are made from a tin mill product of the type “black plate” which is a light gage low-carbon, cold-reduced steel. According to ASTM A623-05, it features a maximum carbon and manganese content of 0.13% and 0.6% respectively. The material has been supplied by ArcelorMittal in the T4 temper.

Uniaxial tensile tests are performed under static loading conditions to characterize the anisotropic plastic properties of this sheet material. Dogbone shaped ASTM-E8 specimens are extracted from the sheets along the rolling direction, the cross-rolling direction and the 45° direction. We make use of a universal testing machine (MTS Model 318.10) with a 100kN load cell. The specimens are loaded at a constant cross-head velocity of 2mm/min. A random speckle pattern is applied to the specimen surface and monitored throughout testing using a digital camera (Allied Vision, PIKE) with 10mm Nikon Nikkor lenses. The axial and width

strains are determined based on a series of 500-1000 pictures using digital image correlation; the virtual extensometer lengths are 15mm and 9mm for the axial and width directions, respectively.

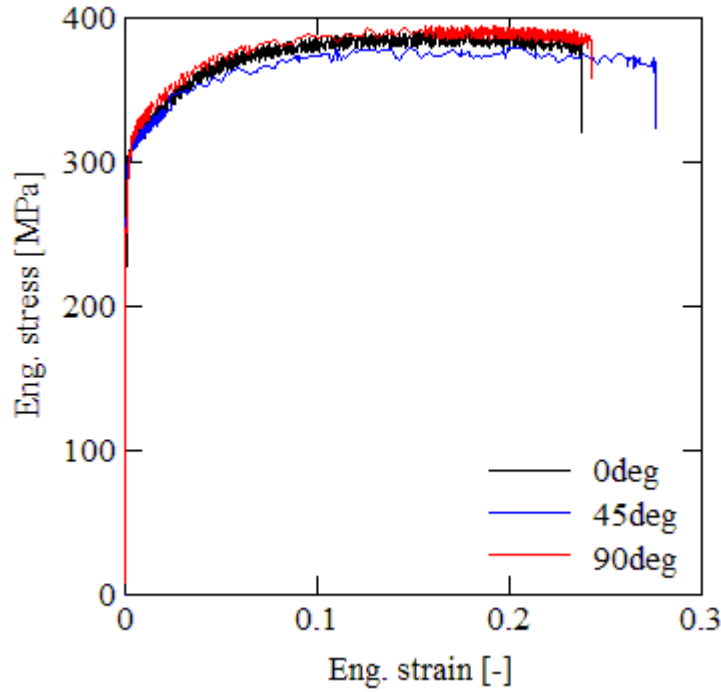


Fig. 1.2 : Engineering stress-strain curves for the 0.2mm thick low carbon steel sheet for loading along different in-plane directions.

The measured engineering stress-strain curves are presented in Fig. 1.2. Assuming a Young's modulus of 210GPa and an elastic Poisson's ratio of 0.3, we determined a yield stress of about 310MPa at 0.2% plastic strain for all loading directions. The Lankford ratios are determined from the average slope of a plot of the logarithmic plastic width strain versus logarithmic plastic thickness strain (assuming plastic incompressibility). Upon evaluation, we find $r_0 = 0.69$, $r_{45} = 1.15$ and $r_{90} = 0.76$. In our simulations, we make use of the Hill (1948) yield function along with an associated flow rule and isotropic hardening to model the sheet material behavior. The corresponding yield stress ratios are given in Table 1.1.

All specimens fractured at an engineering strain of about 0.25. Here, we extrapolate the measured true stress versus logarithmic plastic strain curve using the modified Swift law

$$\sigma = K(\varepsilon_p + \varepsilon_0)^n \quad (1.2)$$

with the parameters $K = 570 \text{ MPa}$, $\varepsilon_0 = 0.01$ and $n = 0.13$.

R_{LL}	R_{WW}	R_{TT}	R_{LW}	R_{LT}	R_{WT}
1.00	1.03	0.94	0.90	1.00	1.00

Table 1.1 : Yield stress ratios.

1.2. Stamping experiments

1.2.1 Experimental set-up

A stamping experiment is performed to provide an experimental basis for the validation of the computational model that is used for the subsequent parametric study. We manufactured a set of dies with $D = 2.2\text{mm}$. The male tool had the dimensions $d_m = 1.2\text{mm}$ and $r_m = 0.2\text{mm}$, while $d_f = 1.8\text{mm}$ and $r_f = 0.2\text{mm}$ have been used for the female die. The stamping tool features a matrix of 572 pins and dies over an area of 25×25 mm. A four-column low friction guidance system guaranteed the alignment of the die and punch matrices throughout stamping.

The tool is set up at the center of a universal testing machine. The force is applied via a cylinder on the upper clamping block (part #3 in Fig. 1.3). The oil lubricated sheet is positioned between the upper and lower clamping block of the tool (part #1 and #2). Throughout stamping, a 250kN load cell measures the total stamping force, while an LVDT inside the vertical actuator recorded the applied displacement. Each stamping experiment is performed under displacement control at an actuator velocity of 0.33mm/min.

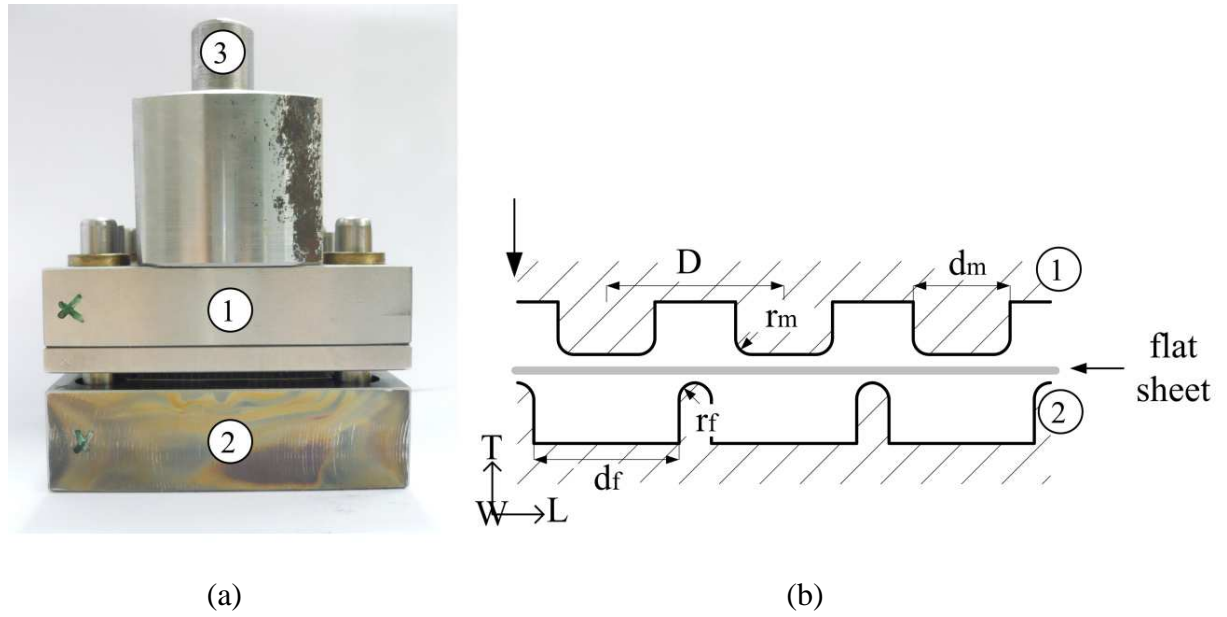


Fig. 1.3 : (a) Photograph of the stamping tool comprising a male die (part 1) and a female die (part 2); (b) side view of before stamping,

1.2.2 Experimental results

The measured force-displacement curves throughout stamping are shown in Fig. 1.4. The superposition of the results from two experiments (red and black curves) demonstrates good repeatability.

After an initial linear response, the slope of the force-displacement curve decreases at a measured displacement of about 0.2mm. The stamping force continues to increase up to a displacement of about 1mm until the sheet fractures. The second experiment is stopped prior to fracture at a displacement of about 0.75mm. The slope of the corresponding loading branch of the force-displacement curve at the beginning of the experiments is smaller than for unloading. This is explained by the evolution of the specimen geometry throughout stamping. At the beginning of the experiment, the sheet material is predominantly subjected to bending, while the state of loading is more membrane-dominated once the sheet has formed its characteristic dimple shape.

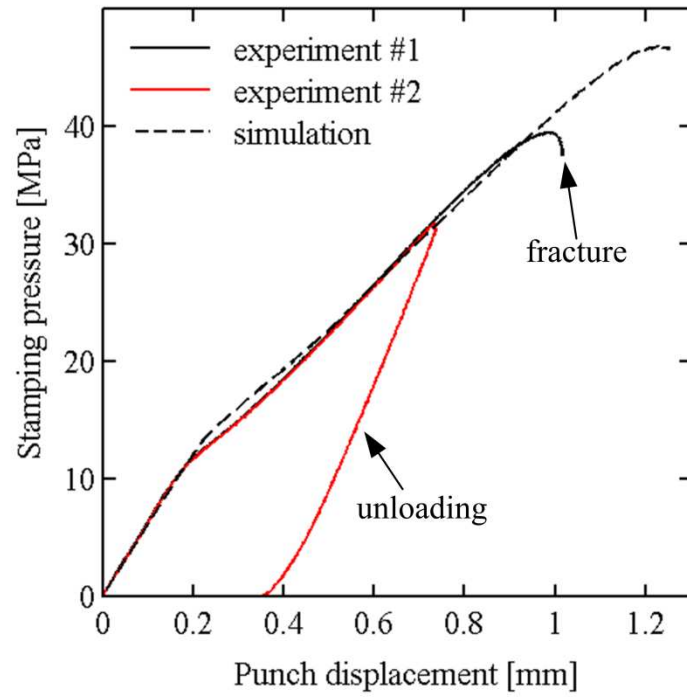


Fig. 1.4 : Stamping pressure versus displacement.

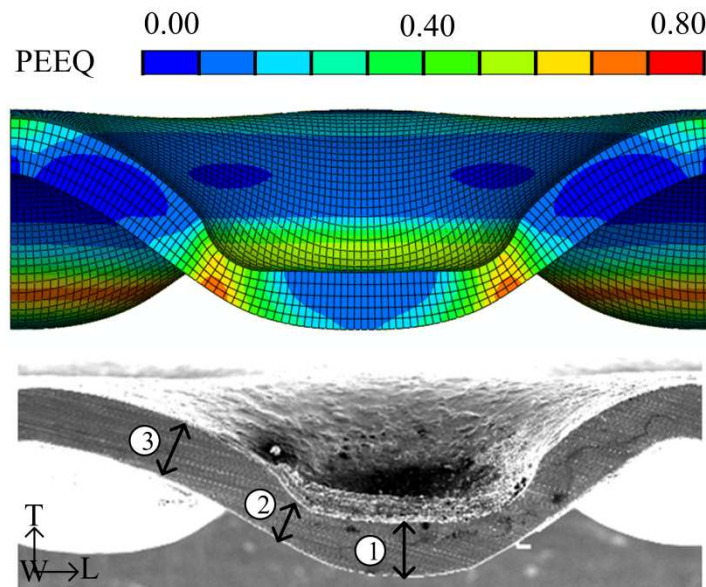


Fig. 1.5 : Side view of a single corrugated layer: comparison of the computed geometry (top) with a scanning electron micrograph of a prototype (bottom).

A SEM picture of a dimpled layer after stamping is shown in Fig. 1.5. The corresponding cross-sectional cut through a single dimple elucidates pronounced necking in a region where the sheet material leaves the punch radius (near cross-section label 2 in Fig. 1.5). Optical thickness measurements indicate that the sheet thickness is reduced to 0.16mm right below the punch while its thickness remains more or less unchanged near the die contact areas. Within the neck region, we observe thicknesses as low as 0.11mm which corresponds to a thickness reduction of 45%.

1.3. Computational models for “virtual experiments”

A finite element model is built to simulate the making of a core layer using Abaqus 6.8.3. The unit cell model of the material microstructure is subsequently used for all the virtual experiments on the bi-layer core structure. Thus, the size of the periodic unit cell and the boundary conditions are chosen according to the symmetry of the experimental set-up. Note that the detailed modeling approach is only feasible with reasonable computational effort at the unit cell level, whereas a macroscopic model is required for the design of structures made from sandwich materials.

1.3.1 Important modeling assumptions

The mechanical behavior of sheet materials in forming and crash simulations can be predicted with remarkably high accuracy using state-of-the-art computational models. Since the proposed sandwich material corresponds to a sheet metal assembly, it is expected that the virtual experiments will provide representative estimates of its effective behavior. The key simplifications with respect to representing the real sandwich structure are:

- (1) Assumption of perfect alignment of the two core layers; when manufacturing the sandwich material, it is very difficult to guarantee the perfect alignment of the core layers. It can be seen from the micrograph shown in Fig. 1.1 that small misalignment errors are present in the real material, while perfect alignment will be assumed in the virtual experiments;

- (2) Negligence of property changes due to brazing; in reality, the four constituent layers of the sandwich material are brazed together; the temperature history throughout brazing may change the steel properties (preliminary experiments have shown this); this effect will be neglected in the present study;
- (3) Assumption of rigid braze joints; it is assumed that the braze joints are very thin and strong, such that the deformation in these joints is negligibly small with respect to the deformation of the core layers.

An attempt was made to confront the results from virtual experiments with experiments on real prototypes. It was found that point #2 presents a first order effect which makes it almost impossible to achieve good agreement.

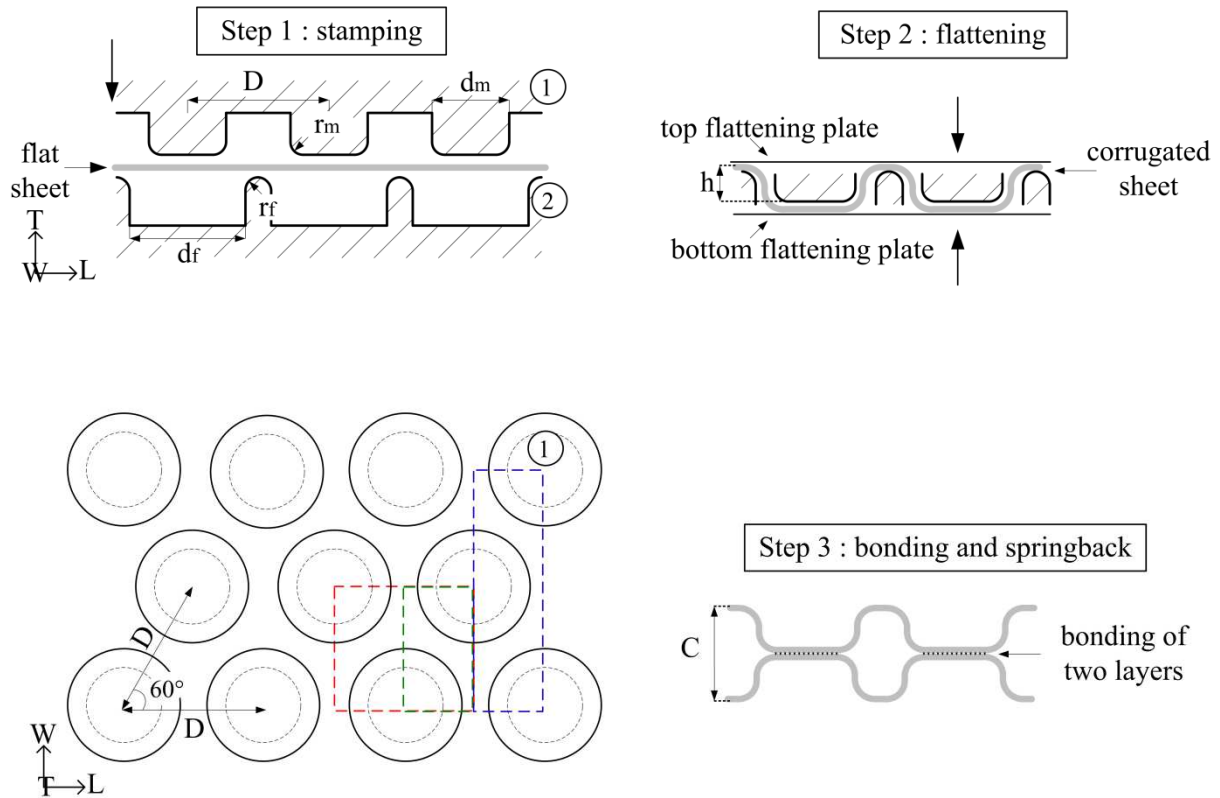


Fig. 1.6 : The manufacturing steps.

1.3.2 Manufacturing simulations

A finite element model of a unit cell of the core structure is obtained after simulating three manufacturing steps:

- (1) the stamping of flat sheets to create the dimpled shaped layers,
- (2) the forming of flat bonding lands on each layer, and
- (3) elastic springback.

The residual plastic strain fields are imported from one step to the next one. Once the core structure is created, flat face sheets are added to form the sandwich structure.

1.1.1.1 Stamping

The dashed rectangles in Fig. 1.6 indicate the size of the unit cell models which are used to perform the virtual experiments. The green lines define the smallest model; the model defined by the red rectangle is twice as long as the green model, while the blue model is twice as wide. The different dimensions are needed to facilitate the definition of periodic boundary conditions (which depend on the specific loading case to be studied). In the case of the small green model, two punches (male die) along with their receiving female dies are needed for the stamping of this unit cell. All forming tools are modeled as analytical rigid surfaces. A mesh with five first-order solid elements (type C3D8R from the Abaqus element library) in the thickness direction is chosen to account for high through-thickness stresses as well as through-thickness necking. The receiving dies are fixed in space while the punches move along the T-direction (Fig. 1.7). To guarantee quasi-static conditions throughout the stamping simulations, the punch velocity increases linearly from 0 to 1m/s over a time interval of 40 μ s. Subsequently, it is kept constant until the maximum stamping depth is reached. A kinematic contact formulation with a friction coefficient of 0.1 is employed to model the contact between the tools and the sheet surfaces. Throughout stamping, the in-plane displacement component u_L is set to zero for all nodes on the boundary surface of normal \mathbf{e}_L , while $u_W = 0$ on all boundaries of normal vector \mathbf{e}_W .

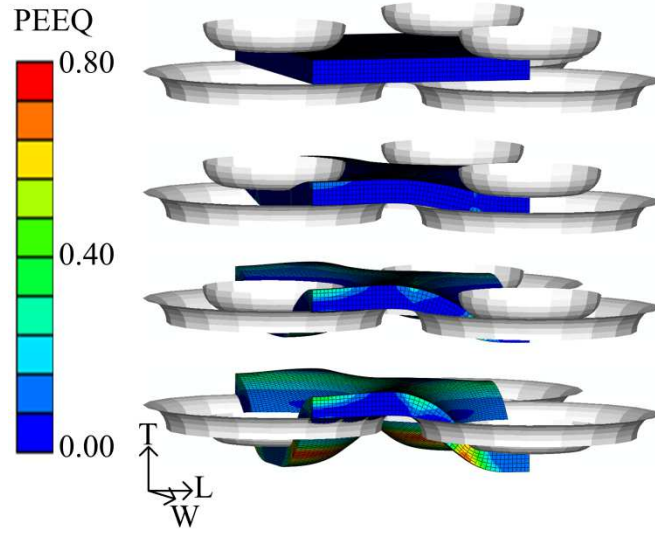


Fig. 1.7 : Sequence of computed geometries during the stamping of a unit cell of a single core layer.

The results from the stamping experiments are compared with the numerical predictions to validate the model assumptions. We define the stamping pressure as the total stamping force per unit area of the stamped sheet. The initial slope of the simulation curve ($K_{simu} = 2363 \text{ MPa/mm}$) is much higher than that of the experiment ($K_{exp} = 65 \text{ MPa/mm}$). This is attributed to the finite stiffness of K_{ma} of the universal testing machine and the forming tool. Considering the forming tool as a spring in series with the work piece, we find a machine stiffness of $K_m = 67 \text{ MPa/mm}$. Figure 1.4 shows the comparison of the simulation and the experimentally-measured stamping pressure versus displacement curves. Note that both curves are initially identical since we added the displacement associated with finite machine stiffness, $\Delta u = P/K_m$, to the simulation result (stiffness correction). The agreement between the two responses is remarkably good. Note that the simulations are performed without any fracture criterion. Consequently, the maximum load in the simulation is determined by the post-necking behavior of the simulation model, whereas the fracture initiates at an earlier point in the experiment.

1.1.1.2. *Forming of the bonding land, springback and joining of the core layers and face sheets*

The four-layer sandwich material needs to be virtually joined together in order to estimate the effective shear properties. A tie contact model (Abaqus, 2008) is used to join the core layers to each other as well as to the respective top and bottom face sheets. After completing

the previous stamping simulations (step #1, explicit time integration), an additional forming step is introduced (step #2, explicit time integration) where flat rigid plates are used to flatten the bonding lands (Fig. 1.6). A first rigid plate applies a pressure to the bottom surface of the corrugated sheet until the resulting material thickness below the centers of the punches equals about 80% of the initial sheet thickness. Similarly, a second rigid plate is used to apply a pressure to the top surface of the corrugated sheet. Here, the simulation is stopped as the initial sheet thickness above the dies equals about 90% of the initial sheet thickness. The flatness of the bonding lands (contact areas) is important to avoid an artificial mesh distortion when using the tie contact model. In reality, the flatness of the bonding lands is also important as it enhances braze joint strength. The flattened bonding lands of two opposing core layers are bonded to each other using the tie option with a position tolerance of 0.001mm.

After joining all layers together with the tie contact, a spring back analysis is performed (step #3). Since springback analyses are simply static simulations without external loading, Abaqus/Standard is preferred for that step whereas all the others were performed using Abaqus/Explicit. The final shape and dimensional changes associated with spring back are negligibly small for the present design, but it is still important to compute a macroscopically stress-free configuration before starting any virtual experiments on this unit cell model. Note that this last step is omitted for virtual experiments in the elastic range of the material as residual strains do not influence the elastic behavior.

Two 0.2mm thick face sheets are created and bonded onto the core layers to form the sandwich structure. A tie contact with a position tolerance of 0.002mm is used to create the virtual bond between the face sheets and the core structure.

Chapter II : Optimization of the Effective Shear Properties of the Bi-directionally Corrugated Sandwich Core Structure

Mohr (2005) investigated the forming by draw bending of sandwich sheets. The results revealed that the core shear failure is the dominant failure mechanism and that high relative density ($>20\%$) core structures are required to withstand the high shear loads throughout forming. Hence, for our material to be formable, it is necessary that it offers great shear strength. Based on the working assumption that sandwich core structures of high transverse shear stiffness will also feature high transverse shear strength, the transverse shear stiffness of the newly-developed all-metal sandwich core structure is investigated numerically using the unit cell model defined in chapter I. Four-point bending experiments are used to validate the finite element model. A parametric study is performed to identify the material architectures that provide the highest shear stiffness-to-weight ratio for relative core densities ranging from 0.2 to 0.35.

The main results of the chapter have been summarized in the form of a journal paper under the title “Optimization of the Effective Shear Properties of a Bi-directionally Corrugated Sandwich Core Structure”, *Journal of Applied Mechanics (in press)*.

2.1. Estimation of the effective shear stiffness

The computational model, corresponding to the red square in Fig 1.6, comprised of two core layers and two face sheets is used for estimating the shear stiffness of the core structure. While an explicit time integration scheme is used for all forming simulations, shear experiments are performed using implicit time integration. The load is applied to the structure via the face sheets (Fig. 2.1).

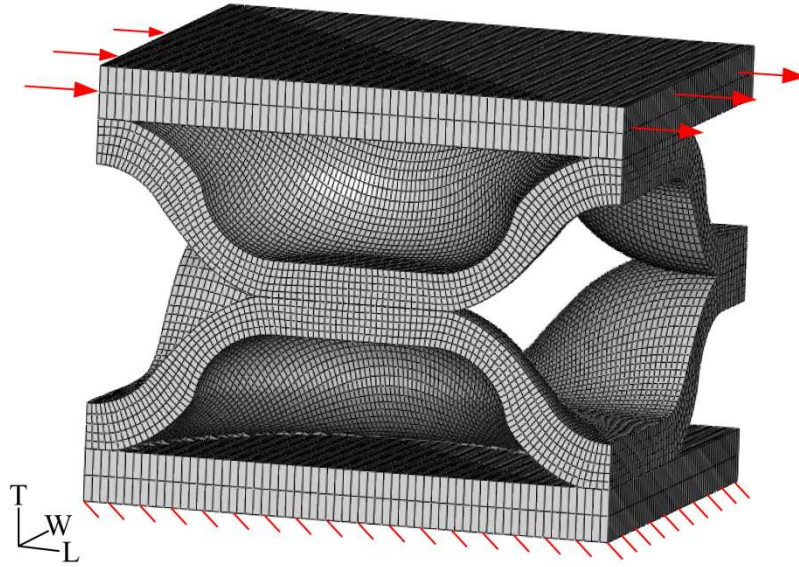


Fig. 2.1 : Unit cell model of the sandwich structure for estimating the transverse shear stiffness.

The boundary conditions estimating the shear stiffness are:

- Periodicity of the structure along the L-direction: the displacements of a node on a first (W,T)-boundary plane are identical to the displacements of the corresponding node with the same x_w and x_T coordinate on the second (W,T)-boundary plane.
- Symmetry of the mechanical problem along the W-direction: the in-plane displacement u_w of all nodes on the (L,T)-boundary planes is set to zero.
- Simple shear loading: A uniform displacement u_L along the L-direction is applied to all nodes on the top (W,L)-boundary plane, while it is set to zero for the bottom

boundary plane. The displacement along the T-direction is set to zero for both the top and bottom (W,L)-boundary planes.

The shear modulus G_{TL} is determined from the slope of the computed linear relationship between the shear force F_L and the applied shear displacement u_L ,

$$G_{TL} = \left(\frac{dF_L}{du_L} \right) \frac{2C}{\sqrt{3}D^2} \quad (2.1)$$

2.2. Parametric study of the effective shear stiffness

2.2.1 Input parameters

The computational model is used to perform a parametric study on the shear stiffness of the proposed sandwich material. In particular, we are interested in finding the “optimal” core geometries that provide the highest out-of-plane shear stiffness for a given relative density. Throughout our simulations, the initial sheet thickness is fixed to $t = 0.2mm$ which corresponds to the lowest gage for low carbon sheet material that is available for large coil widths. The following geometric parameters are varied:

- Stamping depth parameter $\alpha_h = t/(t + h)$. As illustrated in Fig. 1.6, h denotes the punch displacement.
- Dimple geometry parameter $\alpha_D = D/h$. This parameter describes the dimple width to height ratio.
- Bonding land parameter $\alpha_d = d/D$. The diameter α_d determines the size of the dimple's top, i.e. it is closely linked to the bonding land on top of each dimple.
- The corner radii for the punches and dies are always set to $r = d/4$.

The range of parameters is shown in Tab. 2.1.

Geometric parameters						
α_h	0.20	0.22	0.24	0.26	0.28	0.30
α_D	4	5	6	7		
α_d	0.3	0.4	0.5	0.6		

Table 2.1 : Geometric parameters values.

The parameter α_h is varied from 0.2 to 0.3 which corresponds to the lower range of relative densities for which optimal cellular core structures are expected to provide sufficient shear strength for sandwich sheet forming applications (e.g. Mohr and Straza, 2005). Since the initial sheet thickness t is kept constant, the variations of α_h translate also into a variation of the overall thickness of the core structure from about 1.3mm (for $\alpha_h = 0.3$) to 2.0mm (for $\alpha_h = 0.2$). α_D is varied from 4 to 7. A large α_D describes rather shallow cells, while the lowest value is chosen with forming limits in mind. The forming limits of the low carbon steel are not known (as it is not only subject to plane stress, but also substantial through-thickness stresses). However, some preliminary experimental work had shown that the forming of cell geometries with $\alpha_D < 4$ will probably be impossible to achieve in reality because of premature material fracture during stamping. The bonding land parameter α_d is varied from 0.3 to 0.6 which corresponds to a variation of the bonding land area fraction from 8% to 33%. The full permutation of all parameter combinations $(\alpha_h, \alpha_D, \alpha_d)$ resulted in $6 \times 4 \times 4 = 96$ simulation runs.

2.2.2 Results

A summary of all simulation results is shown in Fig. 2.2. It depicts the shear modulus as a function of the parameter α_h . The results reveal that for a given α_h (i.e. the same stamping depth), the shear modulus of the “optimal¹” configuration can be up to three times higher than that of the worst configuration. Figure 2.3 shows the “optimal” configurations for the six α_h that are considered in this study. It is interesting to observe that these feature the same

¹ Here, the adjective “optimal” is used to make reference to the configuration that provides the highest shear modulus among all or a sub-group of configurations considered in this study.

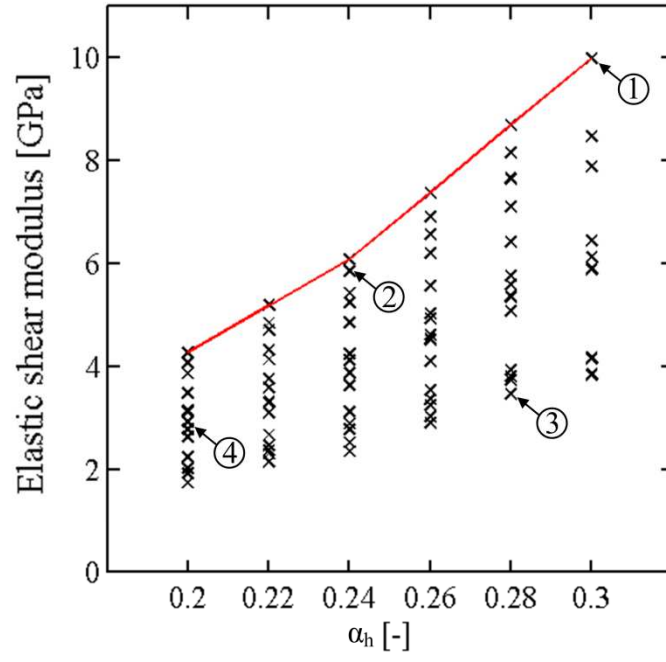
geometric parameters $\alpha_D = 4$ (smallest width to height ratio) and $\alpha_d = 0.6$ (largest bonding land area fraction). Recall that the initial sheet thickness is the same for all configurations. However, the average thickness after stamping decreases as α_h decreases. It may be expected that this decrease in average thickness will also increase the likelihood of fracture during stamping. Note that the through-thickness necking is more pronounced for small values of α_h .

In Fig. 2.4, we show selected results of this parameter study to elucidate the influence of α_D . Observe that the shear modulus is a decreasing monotonic function of the width to height ratio α_D . Truncated cones can be used to represent the dimples of the structure as a simple think model. For constant α_h and α_d , decreasing α_D implies a steeper cell wall angle which makes each “cone” of the core structure less stiff under shear loading.

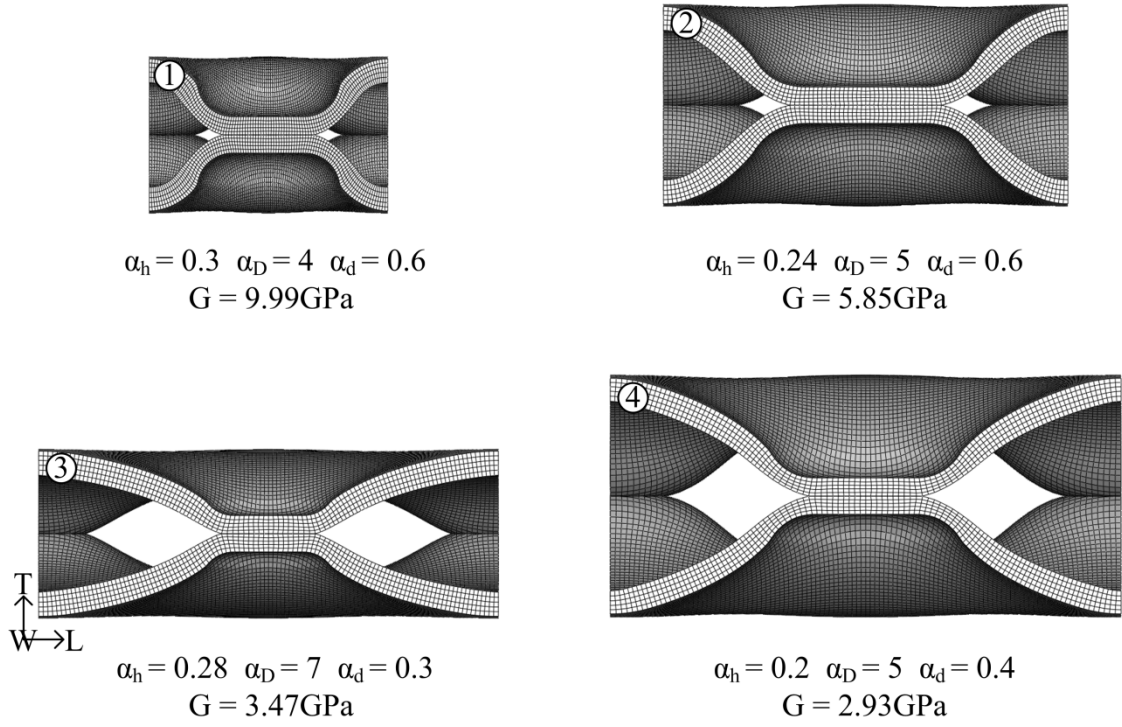
Moreover, the average wall thickness of the cones decreases as α_D decreases, which would also decrease the cones shear stiffness. However, when calculating the macroscopic shear stresses, the stiffness of each cone is normalized by the representative area of $1.8D^2$. The effect of increasing representative area per cone appears to be dominant which explains that the effective shear stiffness decreases as the width to height ratio α_D increases. This model is also validated by a previous numerical study of the effective shear behavior of an idealized core structure with uniform wall thickness that is made from truncated cones. Using the same definitions for the geometry parameters as for the dimpled layers, we find the same result as far as the effect of α_D is concerned.

Akisanya and Fleck (2006) considered that thin-walled frustra may be considered as the basic mechanical element of egg-box structures. They analyzed their response to shear and normal loading both experimentally and numerically. Their results reveal that the effective shear modulus of structures composed of frustra is nearly independent of the cell wall angle (for the same relative density).

The effect of α_d is highlighted in Fig. 2.4. Changing α_d from 0.3 to 0.6 (without changing the height or width of the sandwich core structure unit cell) can increase the effective shear stiffness by more than 100%. The average cell wall thickness decreases and the cell wall inclination angle increases as α_d increases. Both effects suggest that the effective shear stiffness should decrease as α_d increases, which is in contradiction with the simulation result. It is speculated that the low stiffness for small values of α_d is due to the combination of local indentation and necking of the sheet material when using punches of small diameter. The imprint of the punch is clearly visible for all configurations, but the local thickness reduction



(a)



(b)

Fig. 2.2 : (a) Macroscopic shear modulus as a function of the height-to-thickness ratio α_h ; the black crosses represents the simulation results for different stamping tool geometries; (b) cross-sectional views of four selected geometries. The numbered labels indicate the corresponding data points in (a).

is most pronounced in the case of the smallest punch ($\alpha_d = 0.3$, image (2) in Fig. 2.4b). The conical shape of the core structures causes a stress concentration towards the top of each dimple (i.e. the center of the symmetric core structure). This stress concentration is amplified further through the local indentation of the sheet material. Thus, the overall deformation of the core structure under macroscopic shear loading is not only due to the membrane deformation of the cone walls, but also due to the local shear deformation of the zones of stress concentration. A more uniform accumulation of shear deformation can be found for large values of α_d .

Given the observed monotonic relationships between the elastic shear stiffness and the respective geometric parameters, it may be concluded that the tools for forming a single corrugated layer should feature:

- a small dimple width to dimple height ratio α_D
- a large bonding land diameter to width ratio α_d

The final choice of the parameters α_D and α_d is determined by the formability of the sheet material. It is interesting to note that the “optimal” configuration for shear stiffness appears to converge towards a geometry with vertical cell walls which is similar to that of a honeycomb.

2.2.1 Comparison with hexagonal honeycomb

Metallic honeycombs are known to provide excellent shear stiffness when used in sandwich construction. Here, we compare the shear stiffness of the proposed dimpled bi-layer sandwich core structure with that of hexagonal honeycombs. Metallic honeycombs usually feature both single and double-thickness walls which is due to the manufacturing process. Thus, the shear modulus is a function of the loading direction. For shear loading in the T-W-plane, the exact analytical solution for the shear modulus reads

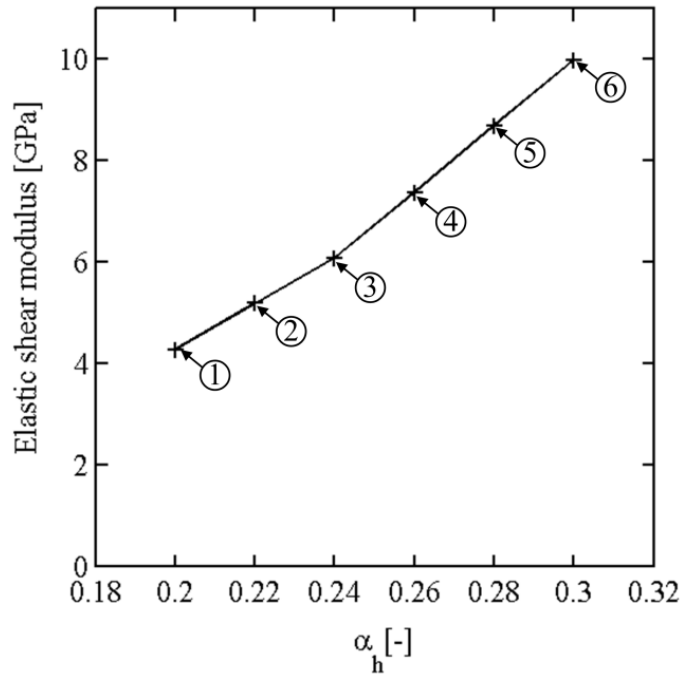
$$\frac{G_{TW}}{G_S} = \frac{3}{8} \left(\frac{\rho}{\rho_s} \right) \cong 0.375 \rho^* \quad (2.2)$$

with G_s denoting the shear modulus of the cell wall basis material. The relative density is defined by the ratio of the effective honeycomb density ρ to the basis material density ρ_s which corresponds to the relative density ρ^* for the dimpled core material. The theoretical bounds for the shear modulus of a honeycomb in the L-T-plane (Kelsey et al., 1958) are

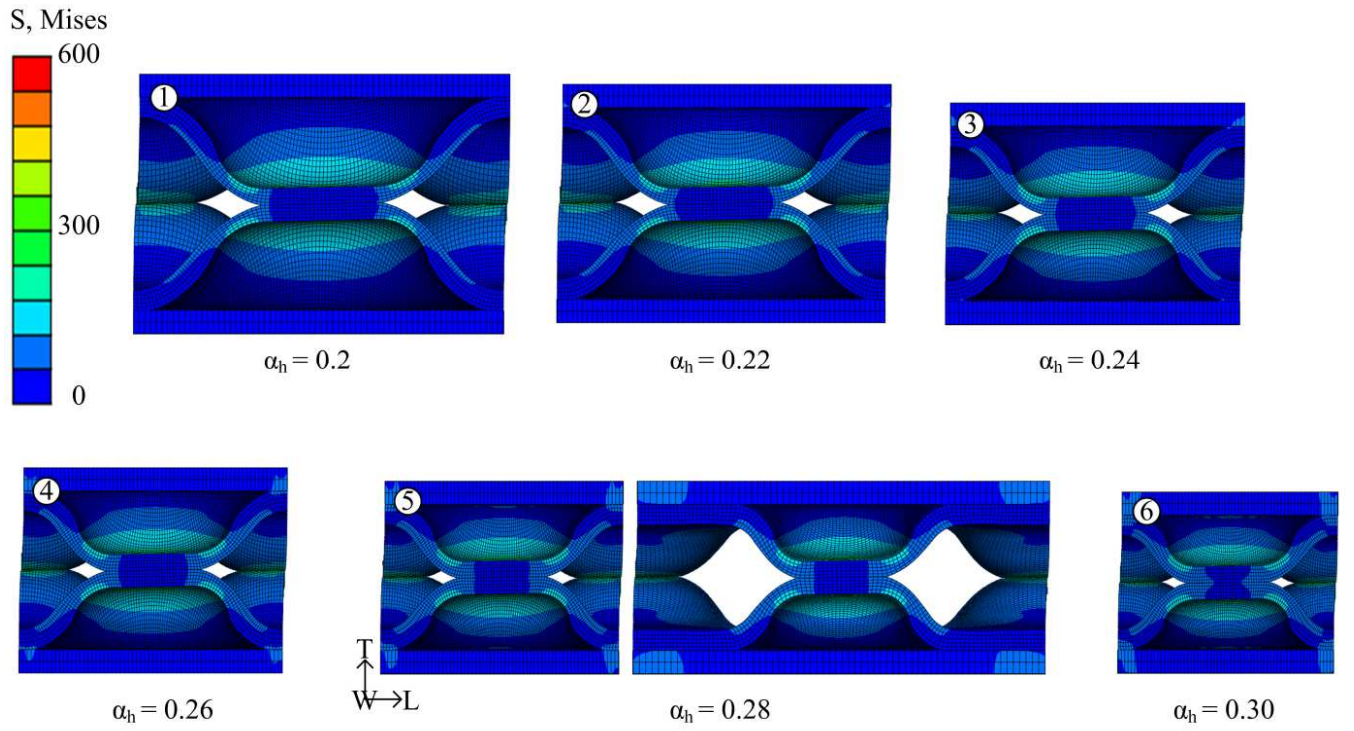
$$\frac{9}{16} \left(\frac{\rho}{\rho_s} \right) \leq \frac{G_{TL}}{G_s} \leq \frac{5}{8} \left(\frac{\rho}{\rho_s} \right) \quad (2.3)$$

As shown by Grediac (1993), the shear modulus G_{LT} is closer to its upper bound of $G_{LT} \cong 0.625\rho/\rho_s G_s$ when used in sandwich structures where the honeycomb cell size is similar to the core height.

The dashed lines in Fig. 2.5 show the theoretical estimates of the shear moduli G_{TW} and G_{TL} (upper bound). The comparison with the computational estimates of the shear modulus for the dimpled material reveals that the weight specific stiffness of honeycomb in the T-W plan, is slightly higher than that of the “optimal” structure. For a relative density of about 0.35, the shear modulus of the dimpled material is 10.0GPa while the one for honeycomb is 10.3GPa. It has to be enlightened that the same shear modulus is found for all in plane-direction of the corrugated core structure (Fig. 2.5).



(a)



(b)

Fig. 2.3 : Optimal configurations for different values of each α_h .

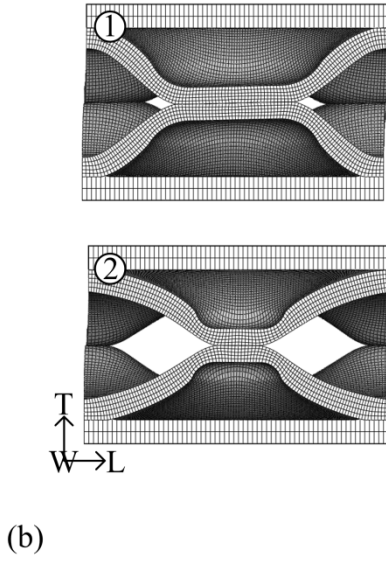
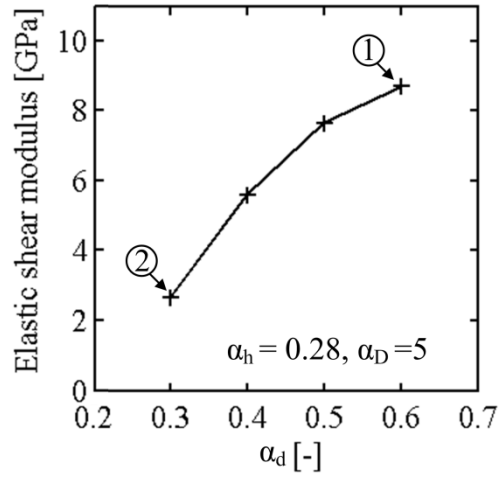
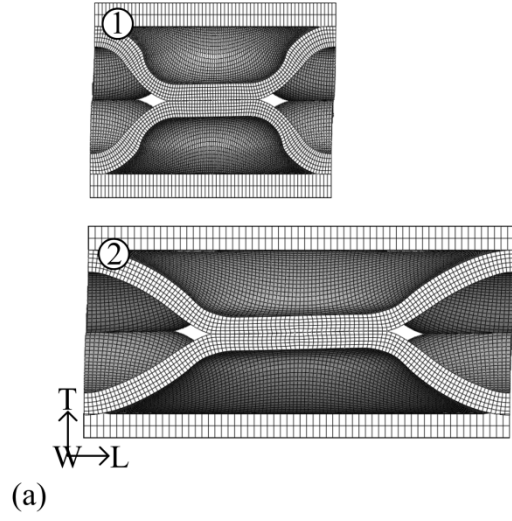
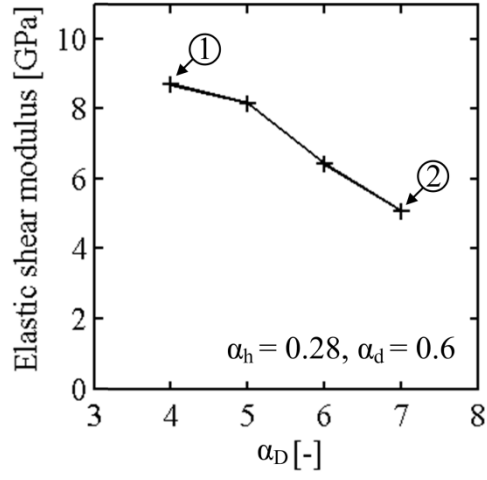


Fig. 2.4 : Influence of the parameters α_D and α_d on the elastic shear modulus.

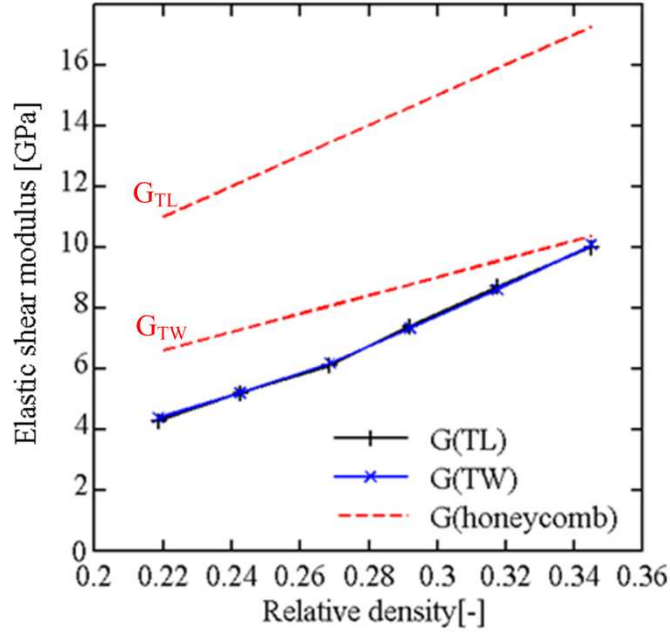


Fig. 2.5 : Elastic shear modulus as a function of the relative density for the proposed core structure (solid lines) and hexagonal honeycomb (dashed lines). Note that the shear modulus of the proposed material is the same for both in-plane directions, while the honeycomb stiffness is direction dependent.

2.2.2 Comment on the optimal design of formable sandwich sheets

The present work focuses on the optimization of the shear stiffness only. As indicated earlier, it is expected that the optimal design for shear stiffness will also be close to the optimal design for shear strength. In practice, premature failure of the bonding between the two core layers as well as of the bonding between the core structure and the face sheets (delamination) might become critical. An ideal sandwich material is designed such that all possible failure modes occur simultaneously. The reader is referred to the textbooks of Allen (1969), Zenkert (1995) or Ashby et al. (2000) for more details on the design of sandwich structures. With regards to the present work, it is worth noting that preliminary draw bending experiments on prototypes demonstrated that the core structure deforms plastically before braze joint failure initiates.

2.3. Experimental validation

A brazed prototype made from low carbon steel with the corresponding optimal microstructure has been provided to us by CellTech Metals (San Diego, CA). The average core relative density of the sample is $\rho^* = 0.29$. It is extremely difficult to measure the shear modulus of sandwich core structures in this density range. Most experimental techniques have been designed for core structures that are both softer and thicker than the present material. Because of its high shear stiffness and small thickness, the overall shear displacement (i.e. the relative displacement between the top and bottom face sheets) prior to failure is very small. An attempt was made to measure this relative displacement through digital image correlation in a shear lap experiment (see ASTM C273) using two sandwich prototypes glued to each other with inner and outer cuts (Fig. 2.6), but inconclusive results were obtained because of the lack in displacement measurement accuracy. In addition to the shear lap test, we performed eigenfrequency measurements and used the identification method of Rebillat and Boutillon (2010) to determine the shear modulus. However, as for the shear lap test, no satisfactory results could be obtained since the shear deformation of the core structure contributed only little to the overall deflection of the vibrating sandwich plate (which was the goal of the optimization).



Fig. 2.6 : Shear-lap test experiment specimen.

As an alternative to the above two testing techniques, we make use of a bending experiment with high shear loads (i.e. a narrow support point spacing). In this experiment, the shear modulus determination can be affected by the local indentation of the face sheets, the underlying sandwich theory and the effect of the face sheet stiffness on the effective core shear stiffness (e.g. Lebee and Sab, 2010). In order to omit any simplifying assumptions throughout the experimental analysis, we perform a large scale finite element analysis of the entire sandwich structures which is subject to bending and compare the computed load-deflection curve with the experimental result.

2.3.1 Four-point bending experiment

Four-point bending experiments are performed on 25mm wide and 120mm long sandwich beam specimens. All specimens are extracted from CellTech sandwich sheets. The thickness varies not only from specimen to specimen (see Table 2.2), but also within each specimen. The thickness measurements at three different locations along the beam axis reveal thickness variations of up to 0.12mm within the specimen; the average thickness of the specimen is $(C + 2t_f) = 1.72\text{mm}$.

Figure 2.7 shows a photograph along with a technical drawing of the four-point bending experiment. The specimen is supported through two cylindrical rollers. Two rollers of the same diameter (15.8mm) are used to apply the loading. The distance of the upper rollers is $a = 25\text{mm}$ in all experiments, while the two different lower support point distances are considered ($b_1=88.7\text{mm}$ and $b_2=73.7\text{mm}$) to vary the ratio of the shear force and bending moment in the four-point bending experiment. The displacement loading is applied through a ball seed using a hydraulic universal testing machine (Model 318.10,MTS). The vertical force is measured using a 2kN load cell, while the position LVDT of the vertical actuator is used to record the applied displacement. There is no need for a machine stiffness correction since the effective specimen stiffness is much smaller than the stiffness of the experimental set-up. The experiments are performed under displacement control at an actuator velocity of 0.125mm/min.

All bending experiments are performed in the elastic range. Thus, the experimental results are characterized by the measured slope of the force-displacement curves, $K = dF/du$. The stiffness K is determined from the linear interpolation of the measured force-displacement curve for a displacement interval of about $\Delta u = 0.5\text{mm}$. Table 2.2 summarizes the experimental results for four different specimens and the two support point distances.

The measured stiffness values vary by -17%/+24% and -11%/+17% around the average for the small and large support point spacing. These variations are primarily attributed to variations in sample thickness as well as the thickness variations within each specimen. However, there are many other sources of experimental uncertainty which are worth mentioning. For example, the specimen is not perfectly flat and the axes of all four roller axes are not perfectly parallel; as a result, the specimen is loaded in an uneven manner which would reduce its apparent stiffness. Even though large diameter rollers have been chosen, the local indentation of the sandwich beam may contribute to an experimental error.

Note that the indentation stiffness of the sandwich specimen depends also on the location of the support point with respect to the contact points between the face sheet and the dimpled core structure. Variations in the shear stiffness may also be due to defects in the braze joints as well as poor alignment of the core layers with respect to each other

Sample	C_{moy} mm	K_1 N.mm^{-2}	K_2 N.mm^{-2}
1	1.38	5.36	9.90
2	1.40	5.50	9.12
3	1.25	4.67	8.69
4	1.49	6.96	11.50
Average	1.38	5.62	9.80

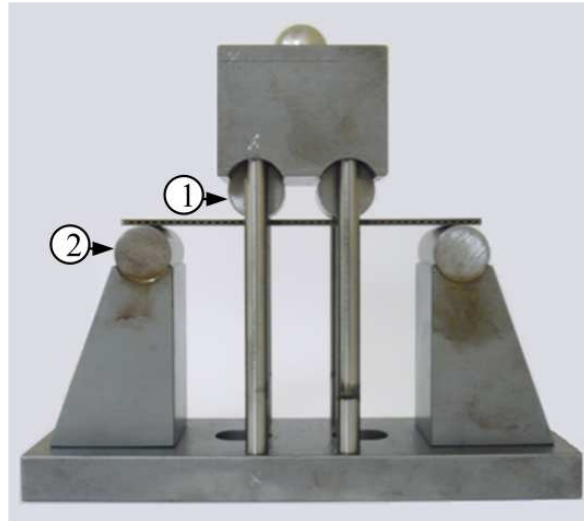
Table 2.2 : Four point bending experiment results. K_1 and K_2 respectively the stiffness per unit width for the cylinders spacing b_1 and b_2 .

2.3.2 Model for the bending of the sandwich structure

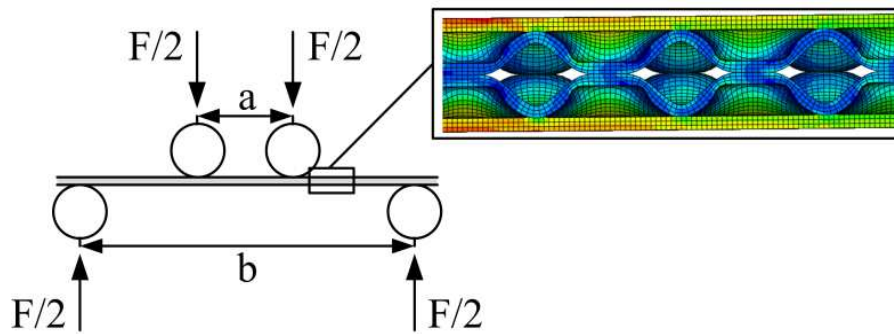
Using the same procedure as for the above unit cell computations (stamping, flattening, joining), we built a computational model of the four-point bending material. Due to the symmetry of the experimental set-up, only one half of the specimen is modeled. The boundary condition $u_L = 0$ is applied to all nodes located on the W-T-symmetry plane. Furthermore, we assume a wide beam (plane strain conditions along the W-direction) and make use of the periodicity of the core structure to reduce our computational model to a 1.91mm wide beam with periodic boundary conditions along the W-direction ($u_W = 0$ on all L-T-boundary planes). 44 punches and dies are required for the stamping process. The modeled core structure has a height of $C = 1.31\text{mm}$, which corresponds to a relative density of $\rho^* = 0.31$. The support and loading rollers are modeled as analytical rigid surfaces. All degrees of freedom of the rollers are fixed except for the vertical motion of the upper loading roller. Explicit time integration is used because of the size of the computational model ($>100,000$ elements) and the modeling of contact. To guarantee quasi-static loading conditions, the upper cylinder velocity is increased linearly from 0 to 5mm/s over a time period of $100\mu\text{s}$ and

from 5 to 100mm/s over another period of 100 μ s, before keeping the loading velocity constant. The contact between the tool and the sandwich surfaces is modeled using a kinematic contact model with a friction coefficient of 0.1.

After completing the finite element analysis for a support point spacing of $b_1 = 88.7mm$ and $b_2 = 73.7mm$, the specimen stiffnesses $K_1 = 5.5N/mm^2$ and $K_2 = 10.5N/mm^2$ are obtained from the linear load-deflection curves. The numerical results are remarkably close to the average stiffnesses measured experimentally: K_1 is underestimated by 3%, while K_2 is overestimated by 7%. Recall that the experimental results feature significant scatter (as explained above) and that the thickness of the numerical model is slightly smaller than the average for all samples.



(a)



(b)

Fig. 2.7 : Four-point bending of wide sandwich beams: (a) photograph of the experimental set-up, (b) schematic of the finite element model. The detail depicts a small portion of the deformed finite element mesh.

Despite the known experimental and computational uncertainty, the good agreement of the simulations and the experimental results is seen as a partial validation of the computational model. The mesh used in the bending simulations (three solid elements through the sheet thickness) is coarser than that used for the unit cell analysis (five elements through the thickness). However, the simulation of a unit cell under shear loading revealed that the differences in the shear modulus estimates are less than 1%.

2.4. Conclusions

The transverse shear stiffness of the bi-directionally corrugated core structure is analyzed both experimentally and numerically using a detailed finite element model. A parametric study is performed to choose the stamping tool geometry such that the resulting core structure provides maximum shear stiffness for a given relative density. It is found that the optimal geometries for relative densities ranging from 0.2 to 0.35 all feature the same dome shape with the same height-to-width ratio, i.e. a small dome width to dome height ratio and a large bonding land diameter to dome width ratio. The simulation results also show that the estimated transverse shear strength of the proposed core structure is the same as that of hexagonal honeycombs of the same weight for high relative densities (greater than 0.35), but up to 30% smaller for low relative densities (lower than 0.2). However, unlike for hexagonal honeycombs, the shear stiffness is approximately the same for both in-plane directions.

Chapter III : Plasticity of Formable All-metal Sandwich Sheets: Virtual Experiments and Constitutive Modeling

Performing numerical simulations using a detailed model of the core unit cell as defined in the previous chapters is reasonable as it features about 105 000 elements. However, numerical difficulties would be found for more complex experiments on wider surfaces. Hence, for numerical efficiency, the analysis of cellular structures with numerical tools is preferably performed in terms of effective properties rather than using a detailed model of the given microstructure. The goal of the present chapter is to define a macroscopic phenomenological constitutive model of the sandwich structure in the perspective of modeling forming and draw bending experiments on wide surfaces. First, the behavior of the bi-directionally corrugated sandwich structure under different uniaxial loadings is investigated. Finite element experiments are carried out using the detailed unit cell model of the “optimal” core geometry, as defined in chapter II, for a relative density of $\rho^* = 0.31$. Then, based on biaxial tensile experiment simulations and a plastic work yield criterion, a constitutive model using distortional hardening is proposed and is used in conjunction with a layered shell element formulation to represent the sandwich structure.

The main results of this chapter have been summarized in the form of a journal paper under the title “Plasticity of Formable All-metal Sandwich Sheets: Virtual Experiments and Constitutive Modeling”, International Journal of Solid and Structures (*under revision*).

3.1. Models for virtual experiments

The virtually manufactured unit cell model of the bi-directionally corrugated sandwich sheet, as described in chapter I, is used for the virtual experiments. We use the geometry presenting the highest shear stiffness-to-weight ratio, as defined in chapter II, with

$$D = 2.06mm, d_m = 1.23mm, r_m = r_f = 0.31mm \text{ and } d_f = 1.44mm.$$

Here we have the initial face sheet $t = 0.2mm$ and the core thickness $C = 1.31mm$, hence, the sandwich structure height is $H = 1.71mm$ and the relative density $\rho^* = 0.31$.

The model includes the residual stress and plastic strain fields due to manufacturing. Here, we briefly describe the boundary conditions and output variables that have been used to characterize the effective mechanical behavior of the sandwich material. In fig 3.1, we recall the colored dashed lines marking the boundary of the unit cell used for the different virtual experiments. All simulations results are presented in Section 3.2.

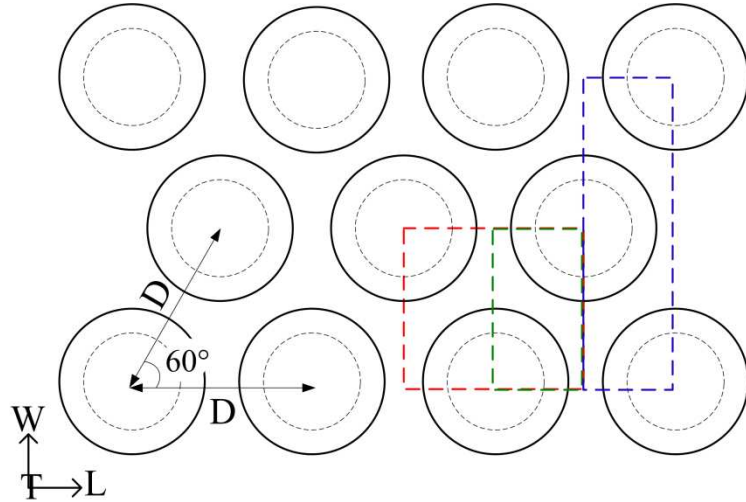


Fig. 3.1 : The colored dashed lines mark the boundary of the unit cell used for selected virtual experiments.

3.1.1 Out-of-plane compression

The red unit cell model is positioned between two flat rigid plates (of normal \mathbf{e}_T). The upper plate moves along the T-axis, while the lower plate is fixed in space. To guarantee

quasi-static conditions throughout the simulation (with explicit time integration), the loading velocity increases linearly from 0 to 0.003m/s maximum over a time interval of 5ms and is kept constant until the end of the virtual experiment. A kinematic contact formulation with a friction coefficient of 0.1 is employed to model the contact between the tools and the sheet surfaces. Periodic boundary conditions are defined for all nodes positioned on the lateral boundaries (of normal \mathbf{e}_W and \mathbf{e}_L).

The effective engineering out-of-plane normal stress is defined as

$$\Sigma_T^c = \frac{F_T^c}{A_T} \quad (3.1)$$

with the initial cross-sectional area $A_T = \frac{\sqrt{3}}{2} D^2$.

The corresponding out-of-plane engineering normal strain is defined as

$$E_T = \frac{u_T}{C} \quad (3.2)$$

where u_T and F_T define the displacement and force applied by the moving upper plane.

3.1.2 Out-of-plane shear

The red unit cell model is used for shear in the (L,T)-plane, while the blue unit cell model is used for shear in the (W-T)-plane. The boundary conditions for shear loading in the (L,T)-plane are:

- Periodicity of the structure along the L-direction: the displacements of a node on a first (W,T)-boundary plane are identical to the displacements of the corresponding node with the same x_W and x_T coordinate on the second (W,T)-boundary plane.
- Symmetry of the mechanical problem along the W-direction: the in-plane displacement u_W of all nodes on the (L,T)-boundary planes is set to zero.

Analogously, for virtual shear testing in the (W,T)-plane, the boundary conditions are:

- Periodicity of the structure along the W-direction: the displacements of a node on a first (L,T)-boundary plane are identical to the displacements of the corresponding node with the same x_L and x_T coordinate on the second (L,T)-boundary plane.
- Symmetry of the mechanical problem along the L-direction: the in-plane displacement u_L of all nodes on the (W,T)-boundary planes is set to zero.

The shear load is introduced by a displacement u_L along the L-direction applied to all nodes on the (W,T)-boundary planes of the top face or by displacement u_W along the W-direction applied to all nodes on the (L,T)-boundary planes of the top face for shearing on the other direction. To guarantee quasi-static conditions throughout the shearing simulations, the loading velocity increases linearly from 0 to 0.003m/s maximum over a time interval of 5ms and is kept constant until the end of the step. Denoting the corresponding reaction forces as F_L^c and F_W^c , we define the out-of-plane engineering shear stresses and strains as

$$T_{LT}^c = \frac{F_L^c}{A_T} \quad \text{and} \quad T_{WT}^c = \frac{F_W^c}{A_T} \quad (3.3)$$

and

$$\Gamma_{LT} = \frac{u_L}{C} \quad \text{and} \quad \Gamma_{WT} = \frac{u_W}{C} . \quad (3.4)$$

3.1.3 Uniaxial in-plane loading

The green model is used for in-plane loading. Due to the symmetry of the mechanical problem with respect to the L-W-plane, a green model with one core layer and one face sheet is used for in-plane simulations. The specific boundary conditions are:

- The in-plane displacement along the L-direction of all nodes on the first (W,T)-boundary plane is set to zero. A kinematic constraint is imposed on all nodes on the

second (W,T)-boundary plane to guarantee that the plane remains flat. The displacement of these nodes is denoted as u_L .

- Analogously, the in-plane displacement along the W-direction of all nodes on the first (L,T)-boundary plane is set to zero. A kinematic constraint is imposed on all nodes on the second (L,T)-boundary plane to guarantee that the plane remains flat. The displacement of these nodes is denoted as u_W .
- The out-of-plane displacement u_T of a set of nodes located on top of the core dimples (i.e. the center of the sandwich core) is set to zero.

For uniaxial tension and compression along the L-direction, we prescribe u_L while u_W is free (Fig. 3.2a). Conversely, we prescribe u_W and leave u_L free for uniaxial loading along the W-direction (Fig. 3.2b).

In the case of in-plane loading, the engineering stresses for the face sheets, core layer and the entire sandwich material are

$$\Sigma_L^c = \frac{F_L^c}{A_L^c}, \Sigma_L^f = \frac{F_L^f}{A_L^f} \quad \text{and} \quad \Sigma_L^s = \frac{F_L^c + F_L^f}{A_L^c + A_L^f} \quad (3.5)$$

$$\Sigma_W^c = \frac{F_W^c}{A_W^c}, \Sigma_W^f = \frac{F_W^f}{A_W^f} \quad \text{and} \quad \Sigma_W^s = \frac{F_W^c + F_W^f}{A_W^c + A_W^f} \quad (3.6)$$

with the initial cross-sectional areas $A_L^f = \frac{\sqrt{3}}{2}Dt$, $A_L^c = \frac{\sqrt{3}}{4}DC$, $A_W^f = \frac{D}{2}t$ and $A_W^c = \frac{DC}{4}$.

The corresponding macroscopic engineering strains read

$$E_L = \frac{u_L}{\left(\frac{D}{2}\right)} \quad \text{and} \quad E_W = \frac{u_W}{\left(\frac{\sqrt{3}D}{2}\right)}. \quad (3.7)$$

3.1.4 Combined in-plane loading

The same unit cell and boundary conditions as for uniaxial in-plane loading are used to perform virtual experiments for combined in-plane loading. We introduce the biaxial loading angle to describe the ratio of in-plane strains,

$$\tan\beta = \frac{dE_W}{dE_L} = \frac{du_w}{\sqrt{3}du_L}. \quad (3.8)$$

The virtual experiments are then carried out for radial loading (i.e. monotonic loading with constant β).

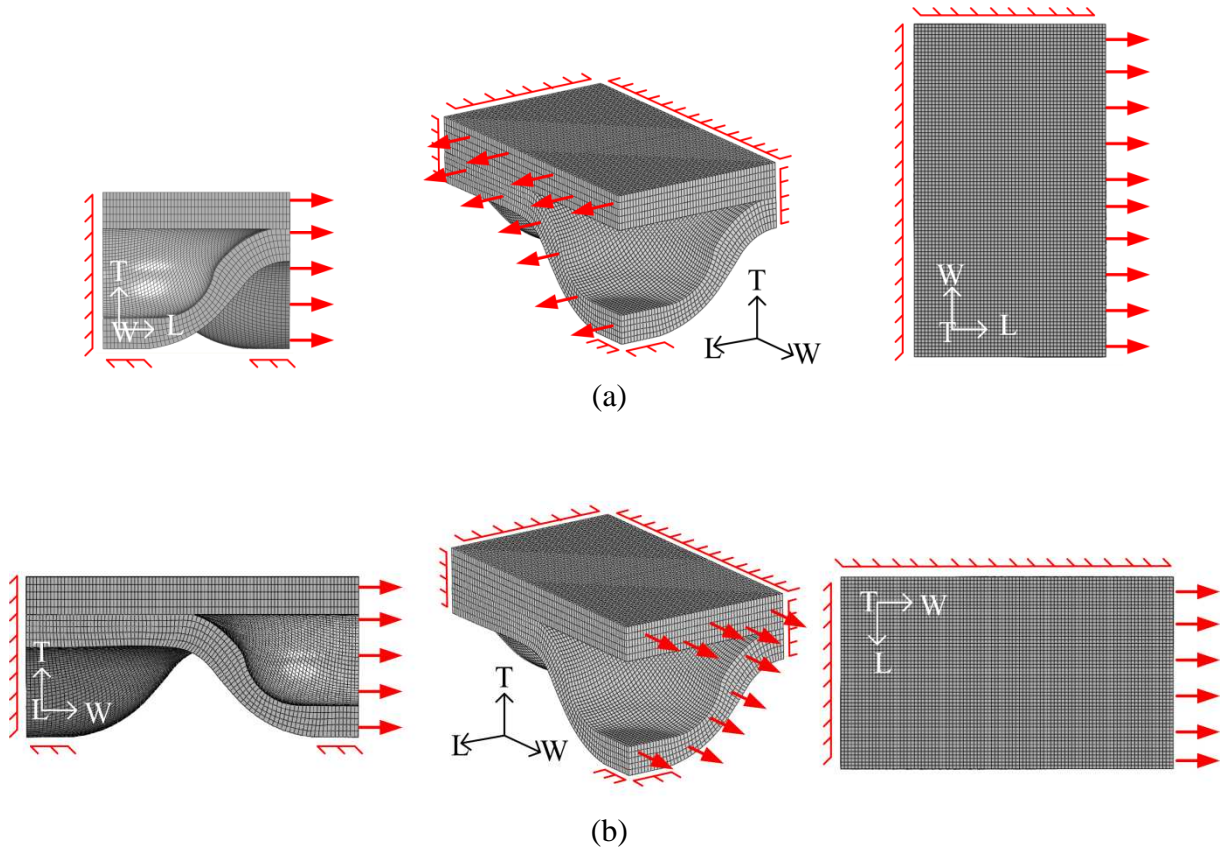


Fig. 3.2 : Illustration of the displacement boundary conditions for uniaxial tension (a) in the L-direction and (b) in the W-direction.

3.2. Results from virtual experiments

The program of virtual experiments includes both out-of-plane and in-plane loading. The emphasis of the present work is on in-plane loading. Selected results for out-of-plane loading are included to shed some light on the overall mechanical behavior of this new material.

3.2.1 *Uniaxial out-of plane compression*

The macroscopic response for out-of-plane loading is shown in Fig. 3.3. The curve starts with a linear elastic regime followed by a monotonically hardening plastic response as the stress exceeds 30MPa. Observe from the deformation snapshots taken throughout different stages of loading that the dome height is progressively reduced during loading. This induces a state of compression in the flat bonding land area in the center of the core structure where regions of very high plastic strains develop. It is important to note that the out-of-plane compressive response of the present material is very different from that of traditional cellular materials. We observe

- no peak stress (which indicates the absence of plastic collapse of the cellular microstructure);
- no plateau regime (which indicates the absence of progressive folding of the cellular microstructure).

However, as for traditional cellular materials, densification is expected to occur for the present material. The simulations were stopped too early to see the effect of densification on the stress-strain curve. The careful comparison of snapshots #2 and #3 reveals that a contact zone develops between the upper and lower domes which corresponds to an increase of the apparent size of the bonding lands.

3.2.2 *Out-of-plane shear*

Virtual experiments for out-of-plane shear loading are performed in the L-T- and W-T- planes. The corresponding engineering shear stress-strain curves (Fig. 3.4) are almost the same (stress level is about 3% higher for L-direction). We observe an initial yield point at

around 15MPa. Thereafter, the stress continues to increase monotonically. Careful inspection of the deformed shapes shows a distortion on the dome structure due to out-of-plane shear.

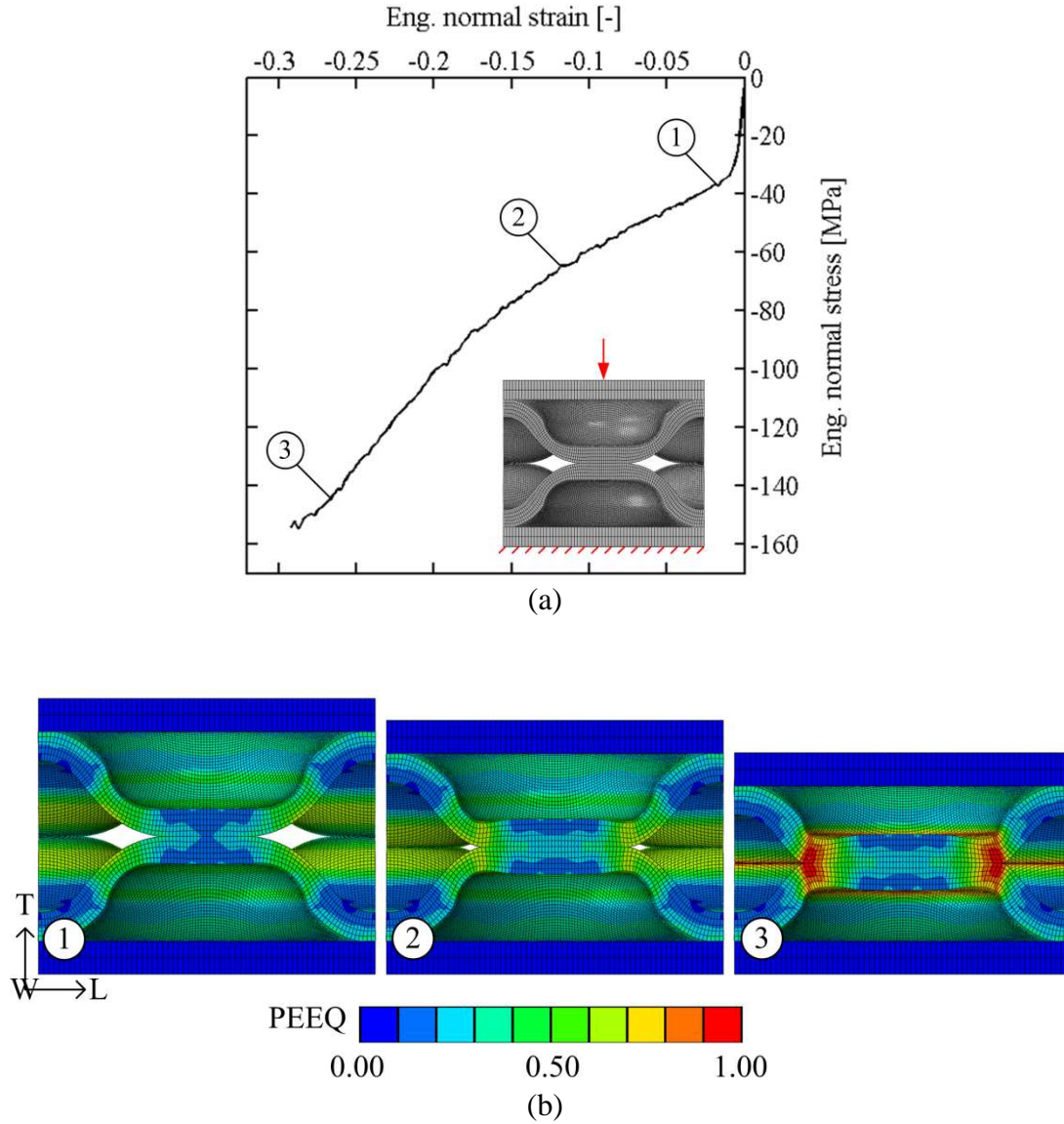
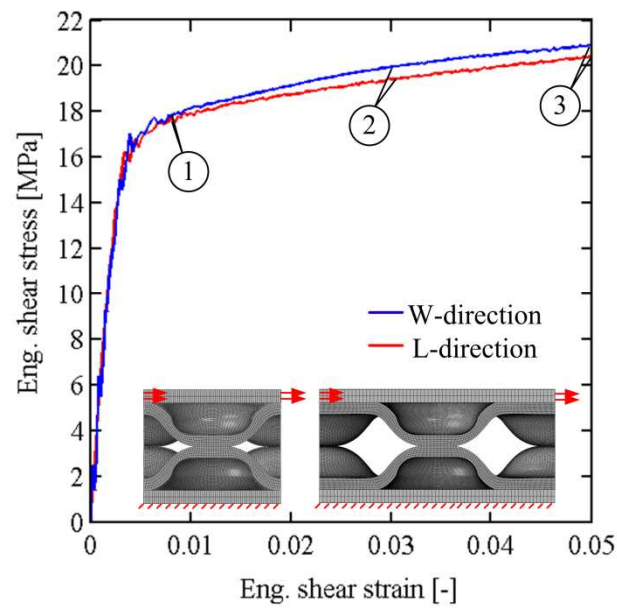


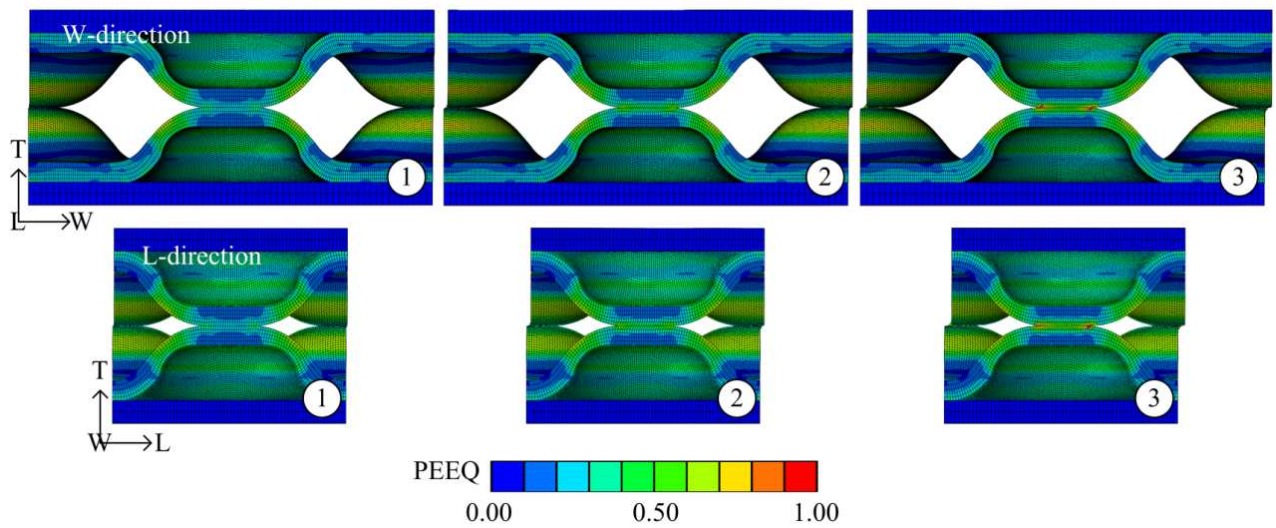
Fig. 3.3 : Out-of-plane compression: (a) macroscopic engineering stress-strain curve; (b) deformed configurations corresponding to the points labeled in the stress-strain curve.

Observe the apparent jump in the displacement field near the center of the vertical unit cell boundaries. This is a three-dimensional effect. For example, for shear along the W-direction, the u_W -displacement field is continuous and satisfied the periodicity conditions along the boundaries, but it varies along the L-direction which gives the impression of a jump when

looking at the projection on the W-T-plane. The highest strains are observed near the braze joints which is expected as the net cross-section is the smallest in that area.



(a)



(b)

Fig. 3.4 : Out-of-plane shear: (a) macroscopic engineering shear stress-strain curves; (b) side views of deformed configurations corresponding to the points labeled in the stress-strain curves.

3.2.3 Uniaxial in-plane tension

Figure 3.5 shows the engineering stress-strain curves for uniaxial in-plane tension. The red curves show the results for tension along the L-direction, while the blue curves correspond to tension along the W-direction. The effective stress-strain curves are monotonically increasing and their shapes resemble that of a conventional metal. For tension in the L-direction, the initial yield stress is about 130MPa for the entire sandwich material and reaches a value of about 160MPa at an engineering strain of 0.15.

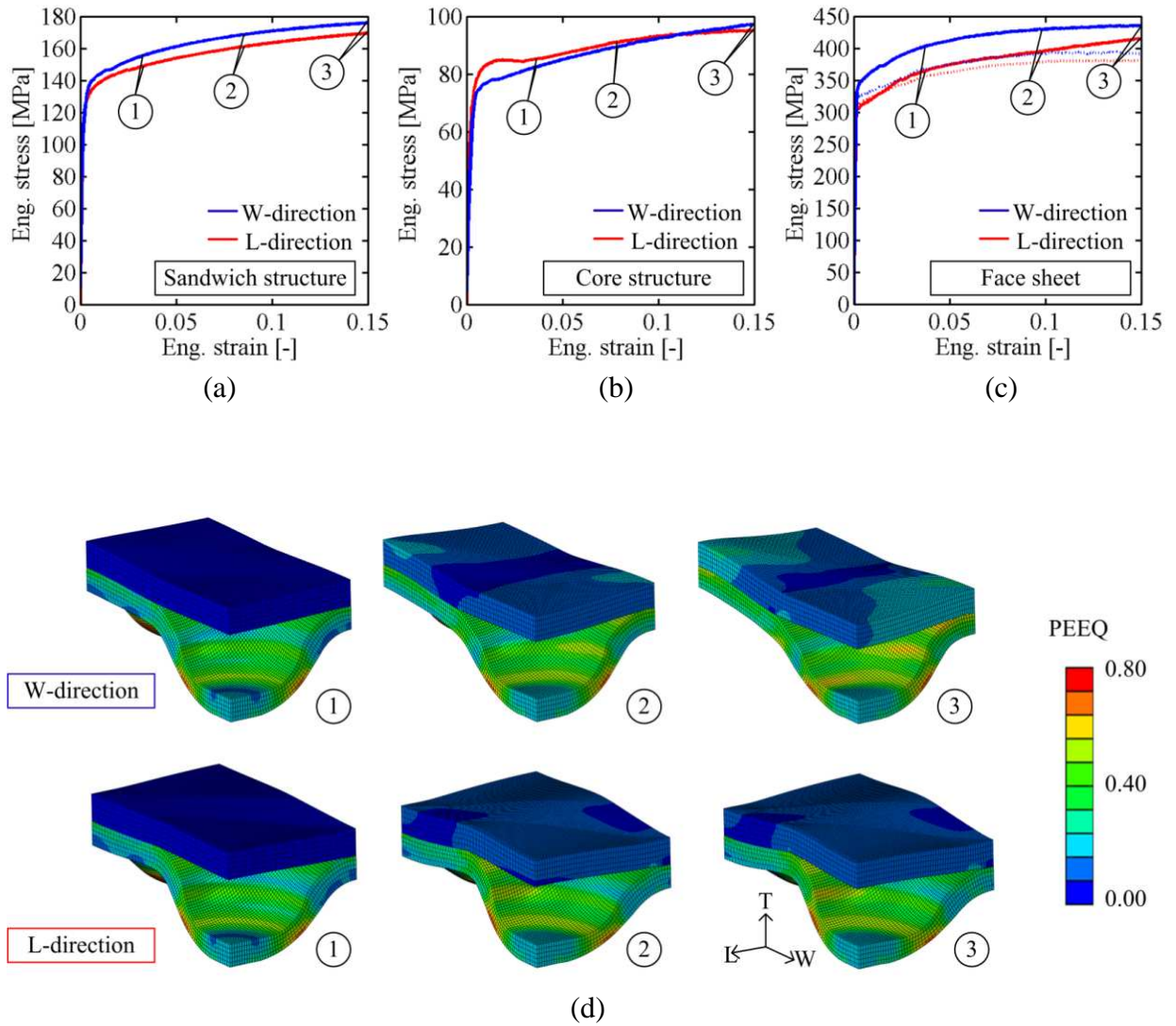


Fig. 3.5 : Uniaxial in-plane tension: engineering stress-strain curves for (a) entire sandwich cross-section, (b) the core structure, and (c) the face sheets; (d) 3D views of the deformed configurations corresponding to the points labeled in the stress-strain curves.

Figure 3.6a) elucidates the contribution of the face sheets and the core layers to the overall axial force of the sandwich material. For tension along the L-direction, the face sheets contribute about 57% to the overall force level, while the core layers contribute the other 43%. This strong contribution of the core layer to the in-plane deformation resistance of the sandwich material is a very special feature of the bi-directionally corrugated core structure. Note that for most traditional sandwich material it is assumed that the contribution of the core layer to the in-plane stiffness and strength is negligible.

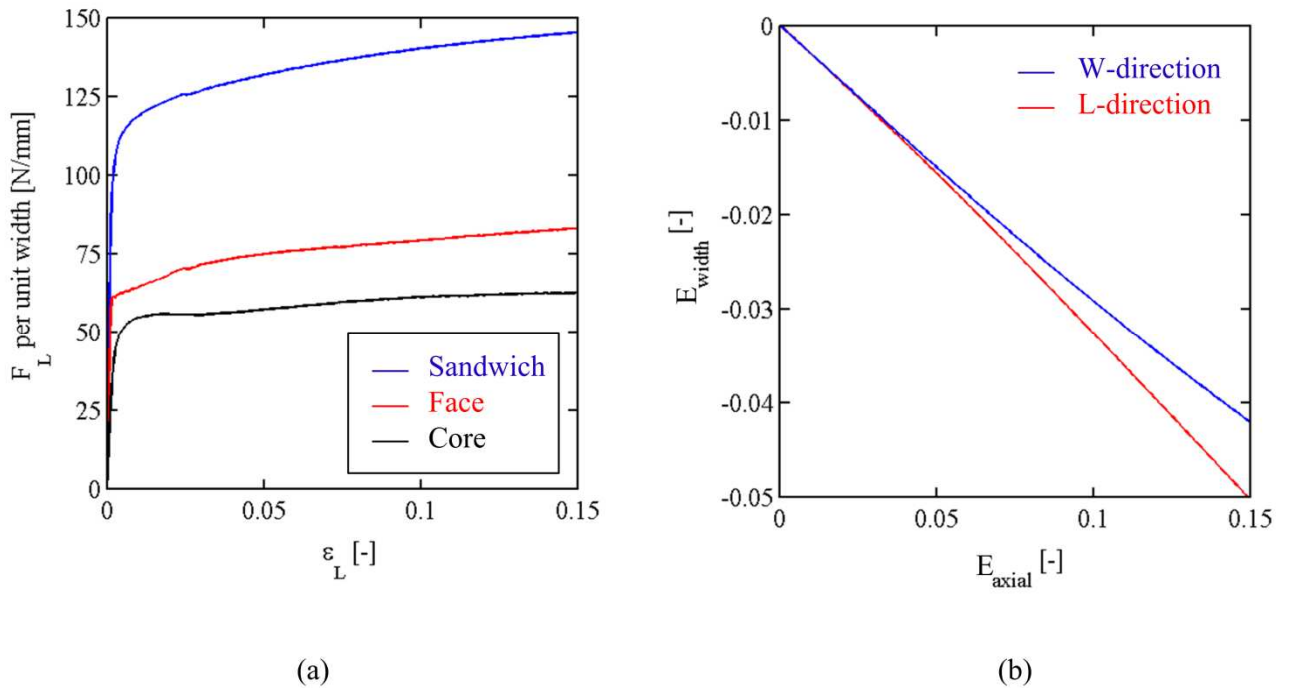


Fig. 3.6 : (a) Decomposition of the section force (per unit width) for uniaxial tension along the L-direction into the contributions of the core structure (black) and the face sheets (red); (b) Engineering strain along the width direction as a function of the axial engineering strain for uniaxial tension along the L- and W-directions.

It is worth noting that the same basis material (alloy and thickness) is used for the face sheets and the core structure. This also implies that the overall weight of the sandwich material is equally split between the face sheets and the core structure. Therefore, the weight-specific response of the face sheets is more effective than that of the core structure (for uniaxial tension), but nonetheless the latter may still be seen as very high for a cellular material. In Fig. 3.5c, we also plotted the stress-strain response of the basis material for reference (dashed lines). The comparison of the dashed and solid curves reveals that a higher

effort is needed to deform the face sheets in the sandwich material as compared to testing these independently from the core structure. The coupling with the core structure results in non-uniform deformation fields (see contour plots in Fig. 3.5d) which increases the plastic work required for axial straining of the face sheets.

The small differences between the two curves shown in Fig. 3.5a indicate some anisotropy in the sandwich material response. The breakdown into the contributions of the faces and core layers (Figs. 3.5b and 3.5c) demonstrates that this anisotropy may be attributed to the face sheet response. However, as shown by the dashed lines in Fig. 3.5c, this anisotropy is not only due to the original (texture related) anisotropy in the basis material. It is also due to the interaction with the core structure.

The core structure is compressible (from a macroscopic point of view) and hence the definition of an r-value is not very meaningful to describe the anisotropy. Instead, we determine an apparent plastic Poisson's ratio from a plot of the width versus axial strain (Fig. 3.6b). For the present material, we obtain $\nu_{LW}^p = -0.33$ and $\nu_{WL}^p = -0.28$ for uniaxial tension along the L- and W-directions, respectively.

3.2.4 Uniaxial in-plane compression

The effective engineering stress-strain curves for uniaxial compression are shown in Fig. 3.7a. They both exhibit a maximum in stress followed by a slightly decreasing stress level. The initial small strain response is very similar to that for uniaxial tension and we observe an initial yield stress of about 130MPa. The shallow peak in stress is associated with the out-of-plane deformation of the face and core sheets which may be considered as a local collapse mode of the sandwich microstructure. This deformation mode is local in the sense that the sandwich mid-plane remains flat (as imposed by the symmetry conditions). The local bending stiffness of the core sheet is determined by the dimple pattern. In the case of compressive loading along the W-direction, less effort (as compared to the L-direction) is required to initiate an out-of-plane deformation mode as a plastic hinge can easily form perpendicularly to the loading direction (which corresponds to the expected orientation of a plastic hinge). This is due to the fact that the domes are positioned such that this hinge line can form between the domes i.e. in the area where the corrugated sheets exhibit the lowest plastic bending resistance. In the case of compression along the L-direction, the dome positioning prohibits the formation of a hinge line perpendicularly to the loading direction. This explains as to why the unit cell is more distorted for compression along the L-direction as compared to the W-

direction. Figure 3.7 indicates that the decrease in stress level is mostly due to the folding of the core structure for W-compression. In the case of L-compression, the macroscopic deformation resistance of the core structure remains more or less constant which is consistent with the described plastic hinge mechanism.

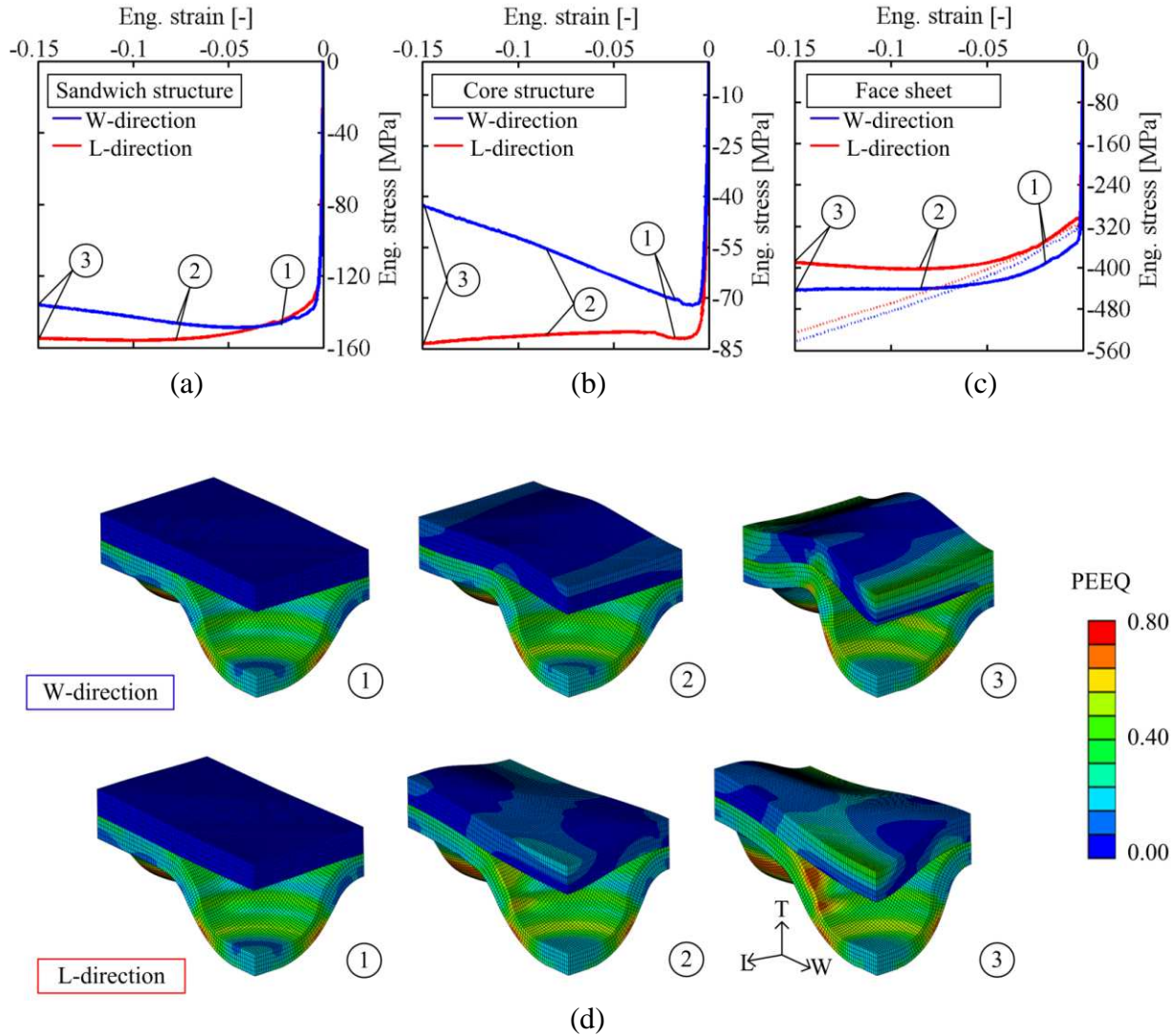


Fig. 3.7 : Uniaxial in-plane compression: engineering stress-strain curves for (a) entire sandwich cross-section, (b) the core structure, and (c) the face sheets; (d) 3D views of the deformed configurations corresponding to the points labeled in the stress-strain curves.

3.2.5 Biaxial in-plane behavior

We limit our attention to states of loading that are of interest to sheet metal forming. Moreover, we assume that the effect of in-plane anisotropy on the mechanical properties is

small and focus on bi-axial in-plane loadings of positive strain along the W-direction ($0^\circ \leq \beta \leq 180^\circ$). In particular, we consider

- $\beta = 0^\circ$ (transverse plane strain tension along L-direction)
- $\beta = 180^\circ$ (transverse plane strain compression along L-direction)
- $\beta = 45^\circ$ (equi-biaxial stretching)
- $\beta = 135^\circ$ (in-plane shear, i.e. equal L-compression and W-stretching)

In addition, in view of constructing an isotropic macroscopic yield surface, three intermediate loading angles are considered:

- $\beta = 11.3^\circ$
- $\beta = 101.3^\circ$, i.e. $\frac{dE_L}{dE_W} = \frac{1}{\tan(101.3)} = -0.2$ which is close to uniaxial tension along the W-direction
- $\beta = 168.7^\circ$, $\frac{dE_W}{dE_L} = -0.2$

Figure 3.8a summarizes all measured engineering stress–strain curves for the different loading cases of the biaxial experiments for the sandwich structure, the core structure and the face sheet. The red dotted lines recall the results for uniaxial tension. All curves for the L-direction are in hierarchical order with respect to β as expected for a conventional engineering material. The stress level for transverse plane strain tension ($\beta = 0^\circ$) is the highest which is a common feature of materials with a convex yield surface and an associated flow rule. Similarly, the stress level for transverse plane strain compression ($\beta = 180^\circ$) is the lowest. The stress along the L-direction is almost zero for $\beta = 101.3^\circ$ which is consistent with the observation that the corresponding stress-strain curve for the W-direction coincides with that for uniaxial tension (Fig. 3.8a).

The contributions of the core structure and face sheet to the overall material response are also shown in Fig. 3.6a. A hierarchical order of the stress-strain curves for the L-direction is observed at this level. However, we note that the W-stress-strain curves for $\beta = 45^\circ$ (tension-tension) and $\beta = 135^\circ$ (compression-tension) do intersect when considering the core structure

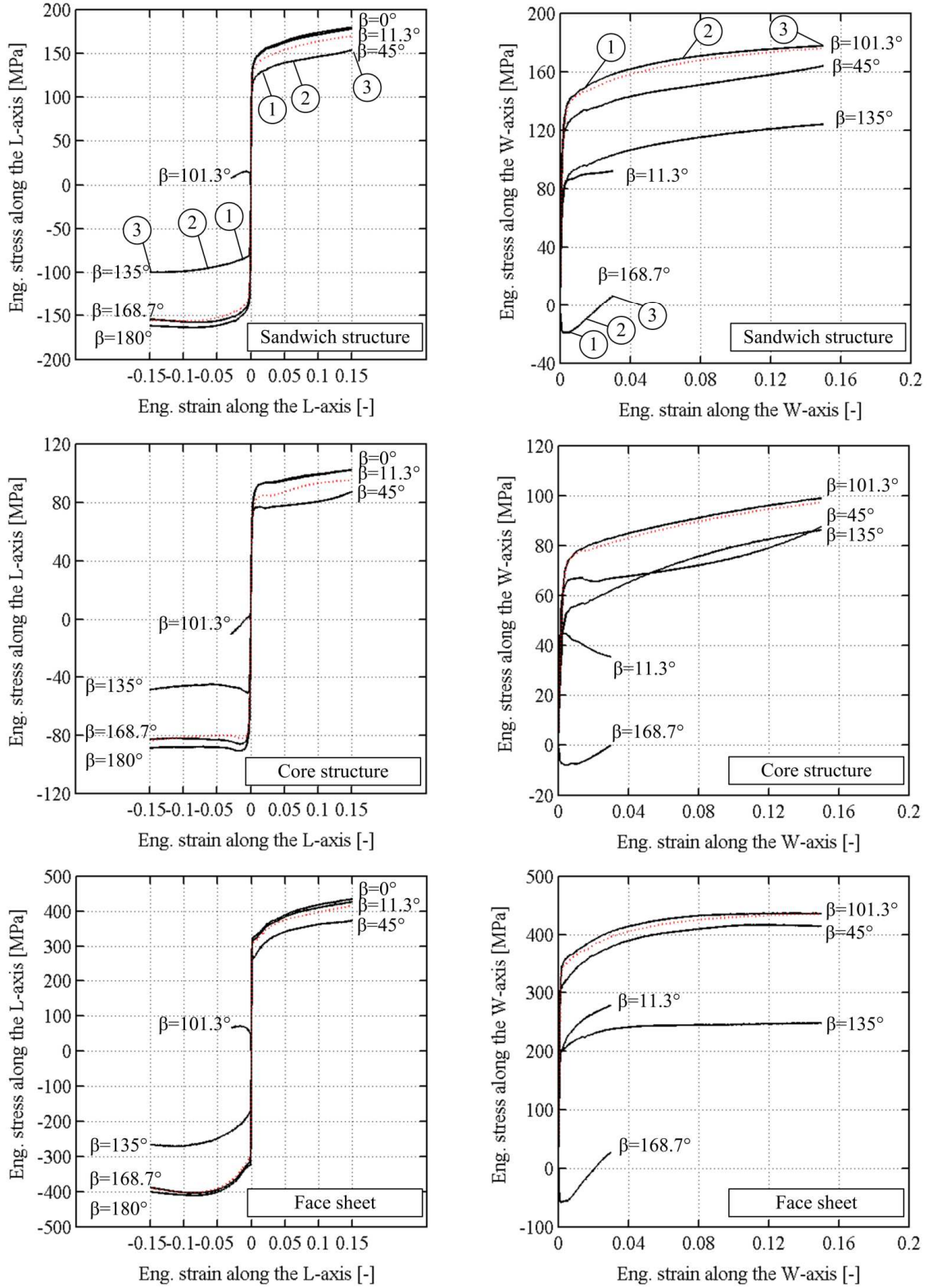
only. The snapshots of various stages of loading in Fig.3.8 b reveal that the sandwich structure is distorted for $\beta = 135^\circ$ which might explain the lower apparent strain hardening of the core layer as compared to $\beta = 45^\circ$ where the core layer appears to be stretched (and flattened) in a more uniform manner. It is worth noting that the face sheets remain approximately flat (i.e. the waviness is smaller than the face sheet thickness) when both in-plane normal stresses are positive. As the second principal stress becomes negative (i.e. compression along the L-direction), we observe local out-of-plane deformation modes (see deformed configurations for $\beta > 101.3^\circ$).

3.2.6 Volume change of core structure

The volume change is determined from the displacement u_T along the T-direction of the nodes located on the inner surface of the face sheets. At a given time step, the average surface displacement u_T is determined and used to compute the engineering thickness strain. The corresponding plastic volume change is expressed through the volumetric strain

$$E_V^p = (1 + E_L^p)(1 + E_W^p)(1 + E_T^p) - 1 \quad (3.9)$$

Figure 3.9 shows a plot of the plastic volumetric strain as a function of the plastic work for all virtual in-plane experiments performed. Except for the initial phase of uniaxial compression and $\beta = 180^\circ$, we observe a volume reduction (compaction). This is expected for tensile loading conditions, but negative volumetric strains are also observed for compression-dominated loading such as $\beta = 135^\circ$ and $\beta = 168.7^\circ$. It is tentatively explained by the distortion of the compressed face sheet which can accommodate a local increase in core thickness, while the increase of the average core thickness is much smaller.



(a)

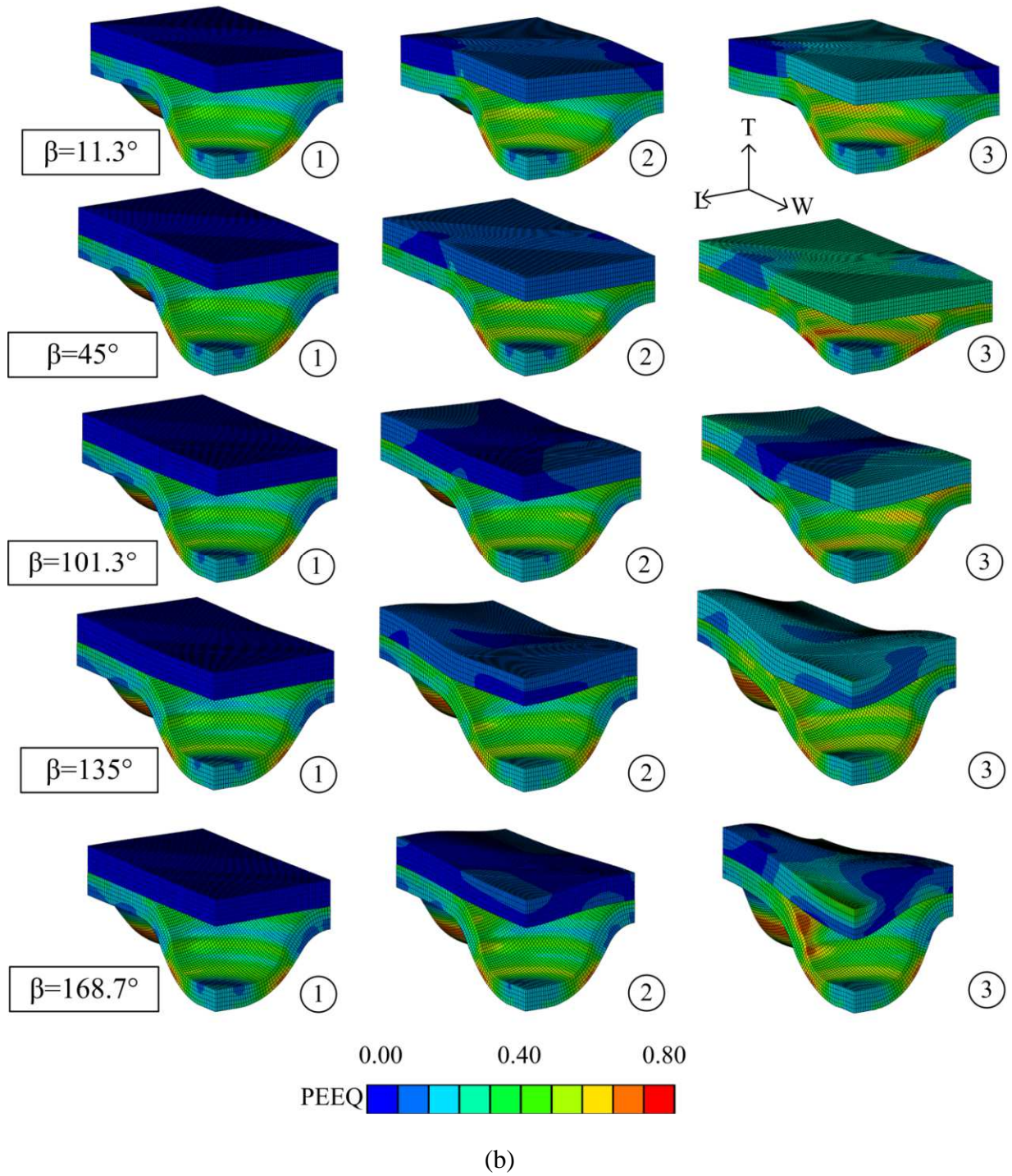


Fig. 3.8 : Bi-axial in-plane loading: (a) Engineering normal stress-strain curves for the L-direction (left column) and W-direction (right column) for the full sandwich cross-section (first row), the core structure (second row), and the face sheets (third row); the label β indicates the bi-axial loading angle; (b) 3D views of the deformed configurations corresponding to the points labeled in the stress-strain curves.

3.3. Phenomenological macroscopic constitutive model

3.3.1 Modeling approach

The goal is to describe the macroscopic behavior of the sandwich sheet material using a composite shell model. A composite shell model assumes that the effect of the out-of-plane normal stress is negligible which is a strong but typical assumption made in the context of thin-walled structures. Different constitutive models are assigned to the thickness integration points of the composite shell element. We therefore need to provide constitutive models that describe the effective behavior of the face sheets and the core structure when built into a sandwich structure. As an alternative, one could consider the entire sandwich sheet as a homogeneous medium and develop a single constitutive model only. However, such a description would be suitable for membrane loading only whereas it is expected to break down in the case of bending loading. The constitutive model for the face sheet basis material is known, but it provides only a poor approximation of the effective behavior of the face sheets when these are integrated into a sandwich structure.

3.3.2 Notation and kinematics

The constitutive equations are written in the material coordinate system which is defined through the longitudinal in-plane direction (L), the width in-plane direction (W) and the thickness direction (T). The Cauchy stress vector summarizes the non-zero stress components in that coordinate frame, $\boldsymbol{\sigma} = \{\sigma_{LL} \quad \sigma_{WW} \quad \tau_{LW}\}^T$, while a standard co-rotational formulation is used to update the orientation of the material coordinate frame as the shell element is subject to large rotations and distortions (Abaqus, 2008). The work-conjugate logarithmic strain components are summarized by the strain vector, $\boldsymbol{\varepsilon} = \{\varepsilon_{LL} \quad \varepsilon_{WW} \quad \gamma_{LW}\}^T$. A superscript ‘p’ is used to denote the corresponding plastic strains, $\boldsymbol{\varepsilon}^p$. Bold lower case letters are used to denote vectors, while second-order tensors are denoted by bold letters. Square brackets are used exclusively to indicate the argument of a function, e.g. $f = f[x]$.

3.3.3 Elastic constitutive equation

The core structure features hexagonal in-plane symmetry. Neglecting possible elastic anisotropy in the basis material, we can therefore use an isotropic elasticity model to describe the effective in-plane behavior, for the core structure as well as for the face sheets,

$$\boldsymbol{\sigma} = \mathbf{C}(\boldsymbol{\varepsilon} - \boldsymbol{\varepsilon}^p) \quad (3.10)$$

with

$$\mathbf{C} = \frac{E}{1-\nu^2} \left(\mathbf{e}_1 \otimes \mathbf{e}_1 + \mathbf{e}_2 \otimes \mathbf{e}_2 + \nu \mathbf{e}_1 \otimes \mathbf{e}_2 + \nu \mathbf{e}_2 \otimes \mathbf{e}_1 + \frac{1-\nu}{2} \mathbf{e}_3 \otimes \mathbf{e}_3 \right) \quad (3.11)$$

E_m and ν denote the elastic modulus and Poisson's ratio for uniaxial in-plane loading, while $\mathbf{e}_1 = \{1 \ 0 \ 0\}^T$, $\mathbf{e}_2 = \{0 \ 1 \ 0\}^T$ and $\mathbf{e}_3 = \{0 \ 0 \ 1\}^T$.

3.3.4 Macroscopic yield surface

The yield function will be chosen such that it defines the envelopes of equal plastic work. We thus computed the plastic work per initial unit volume for each virtual experiment and plotted the corresponding true stress data points (σ_W, σ_L) for selected amounts of plastic work in Fig. 3.10 (face sheets) and Fig. 3.11 (core structure). Note that we assumed plastic incompressibility for the face sheets ($\varepsilon_V = 0$), while the volumetric strains reported in Fig. 3.9 are used when calculating the true effective stresses for the core structure.

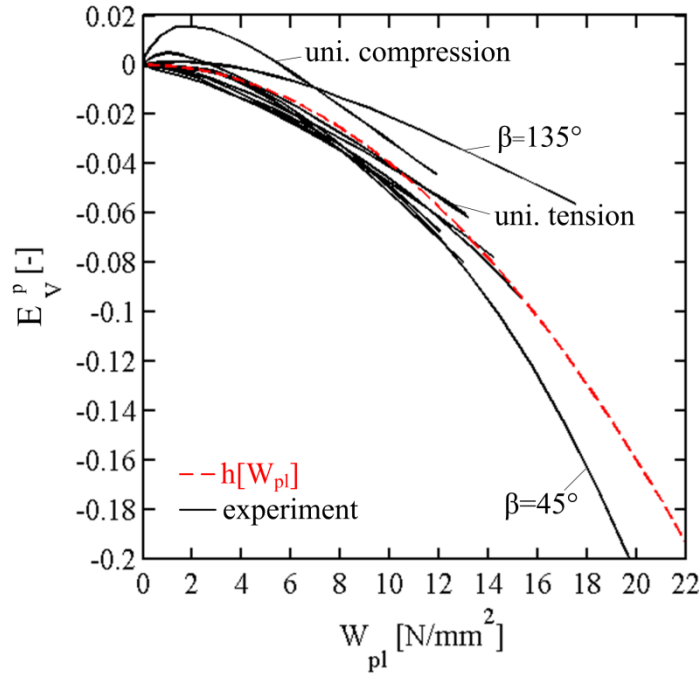


Fig. 3.9 : Plastic volume change during in-plane loading for all virtual experiments performed as a function of the plastic work per initial volume. The red dashed line shows the model approximation according to Eq. (3.23).

Both the core structure and the face sheets are made from a Hill'48 material and it is hence natural to choose the Hill'48 yield function as a starting point for the construction of a yield function for the cellular material. However, the data for the core structure shows a pronounced tension/compression asymmetry which cannot be represented by the Hill'48 function. As a first approximation, the tension/compression difference in our study is attributed to a linear pressure dependency of the effective inelastic material behavior. We therefore define the yield condition as,

$$f = \bar{\sigma} - k = 0 \quad (3.12)$$

where the equivalent stress depends both on the deviatoric and diagonal terms of the Cauchy stress tensor,

$$\bar{\sigma} = \bar{\sigma}_{Hill} + \alpha \sigma_m \quad (3.13)$$

With

$$\bar{\sigma}_{Hill} = \sqrt{F(\sigma_L - \sigma_T)^2 + G(\sigma_W - \sigma_T)^2 + H(\sigma_L - \sigma_W)^2 + 2L\tau_{WT}^2 + 2M\tau_{TL}^2 + 2N\tau_{LW}^2} \quad (3.14)$$

and

$$\sigma_m = \frac{\sigma_L + \sigma_W + \sigma_T}{3}. \quad (3.15)$$

Note that the above yield function preserves the convexity of the original Hill'48 criterion as the associated Hessian matrix is not affected by the linear pressure term. In the case of plane stress, the yield function reduces to

$$f[\boldsymbol{\sigma}] = \sqrt{\sigma_L^2 + G\sigma_W^2 + H(\sigma_L - \sigma_W)^2 + 2N\tau_{LW}^2} + \frac{\alpha}{3}(\sigma_L + \sigma_W) - k = 0. \quad (3.16)$$

We fitted the above expression to our virtual experimental data. The solid envelopes in Figs. 3.10a,d and 3.11a,d show the fit to the data using the parameters listed in Table 3.1.

3.3.5 Distortional-isotropic hardening

Figures 3.10d and 3.11d shows the yield envelopes for two distinct plastic work densities in a single plot. The comparison of the calibrated yield envelopes demonstrates that the elastic domain is not increasing in a self-similar manner. Instead, the shape of the yield surfaces changes substantially (distortional hardening). In Eq. (3.12), changes of k represent isotropic hardening, while changes in the coefficients F, G, H, N and α would represent distortional hardening. As an alternative to modeling the evolution of the yield surface coefficients (e.g. Aretz (2005)), we describe the yield surface evolution through a linear combination of two distinct yield functions $f_1[\sigma]$ and $f_2[\sigma]$,

$$f[\sigma] = (1 - \delta)f_1[\sigma] + \delta f_2[\sigma], \quad (3.17)$$

where the isotropic-distortional hardening factor $\delta = \delta[W_{pl}]$ is defined as a function of the plastic work density. Denoting the plastic work density associated with the yield functions f_1 and f_2 as W_{pl}^1 and W_{pl}^2 , respectively, we impose the order $W_{pl}^2 > W_{pl}^1$.

Note that the linear combination (with positive weights) of two convex functions is still convex. Furthermore, the corresponding weighted equivalent stress,

$$\bar{\sigma} = (1 - \delta)\bar{\sigma}_1 + \delta\bar{\sigma}_2 \quad (3.18)$$

is still a homogeneous function of degree one. For plastic work densities smaller than W_{pl}^1 and greater than W_{pl}^2 , we assume isotropic hardening only. The yield function evolution law may thus be written as

$$f[\sigma] = \begin{cases} \bar{\sigma}_1[\sigma] - (1 + \delta)k_1 & \text{for } W_{pl} \leq W_{pl}^1 \\ (1 - \delta)(\bar{\sigma}_1[\sigma] - k_1) + \delta(\bar{\sigma}_2[\sigma] - k_2) & \text{for } W_{pl}^1 < W_{pl} < W_{pl}^2 \\ \bar{\sigma}_2[\sigma] - \delta k_2 & \text{for } W_{pl} \geq W_{pl}^2 \end{cases} \quad (3.19)$$

where the isotropic-distortional hardening function $\delta > -1$ defines a monotonically increasing function of the plastic work density which fulfills the constraints $\delta[W_{pl}^1] = 0$ and $\delta[W_{pl}^2] = 1$.

3.3.6 Flow rule and volume change

An associated plastic flow rule is adopted to describe the evolution of the plastic in-plane strains. Formally, we write

$$d\boldsymbol{\varepsilon}_p = d\lambda \frac{\partial f}{\partial \boldsymbol{\sigma}} \quad (3.20)$$

with the plastic multiplier $d\lambda \geq 0$. The increment in plastic work density (per initial volume) can be written as

$$dW_{pl} = (1 + E_V^p) \boldsymbol{\sigma} \cdot d\boldsymbol{\varepsilon}_p. \quad (3.21)$$

where a constitutive equation needs to be specified to determine the evolution of the plastic (engineering) volumetric strain E_V^p . Plastic incompressibility is assumed as a first approximation for the face sheets, i.e. $E_V^p = 0$. The core layer on the other hand is considered as compressible. The change in volumetric strain is directly defined as a function of the plastic work density,

$$dE_V^p = h[W_{Pl}]dW_{Pl}. \quad (3.22)$$

In particular, the linear function

$$h[W_{Pl}] = -\kappa W_{Pl} \quad (3.23)$$

with $\kappa = 0.0008 MPa^{-1}$ provides a reasonable approximation of the present experimental data for the core structure (see red dashed curve in Fig. 3.9). Note that the above expression is only valid up to the theoretical densification strain of $E_V^p = \rho^* - 1$.

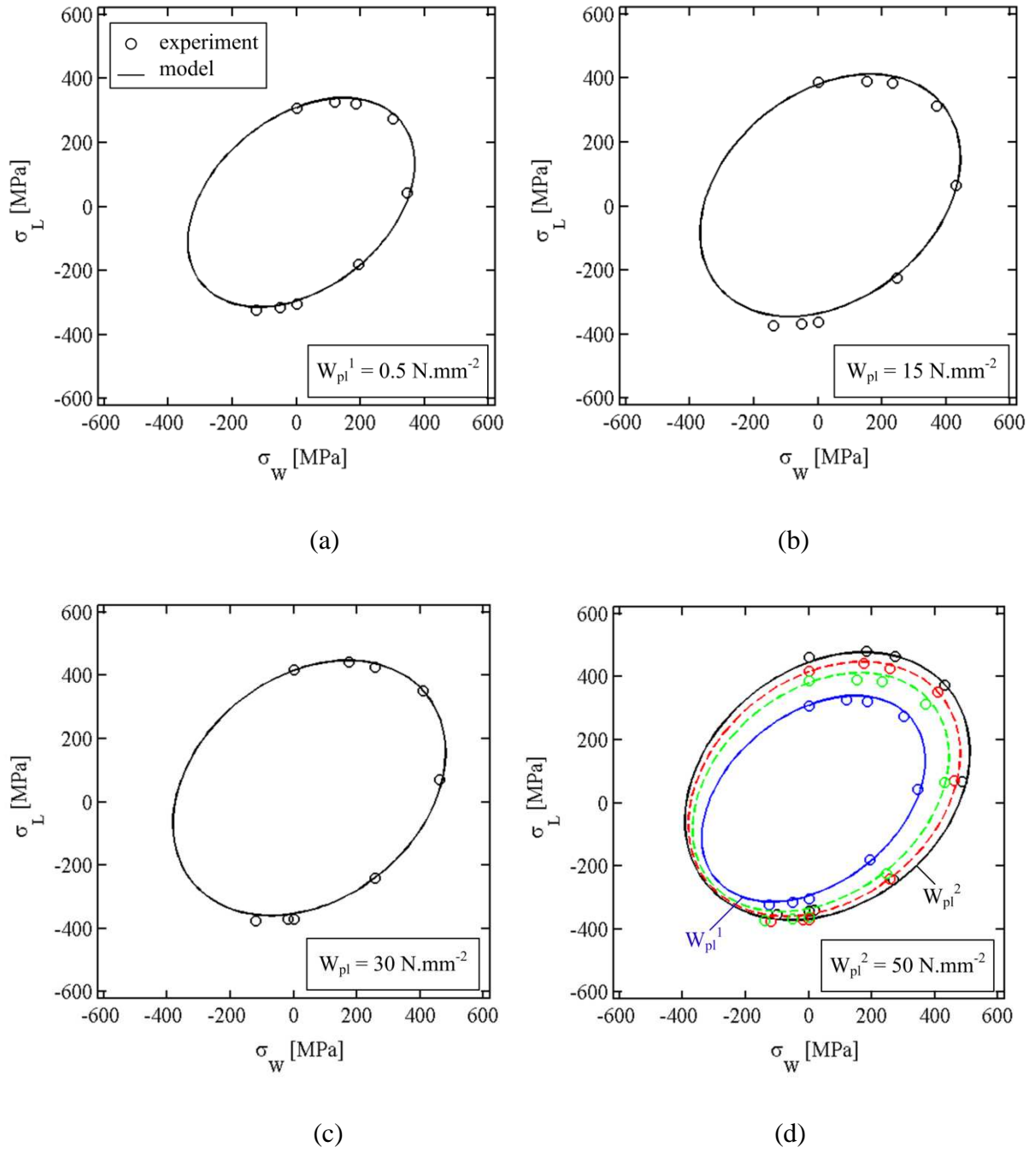
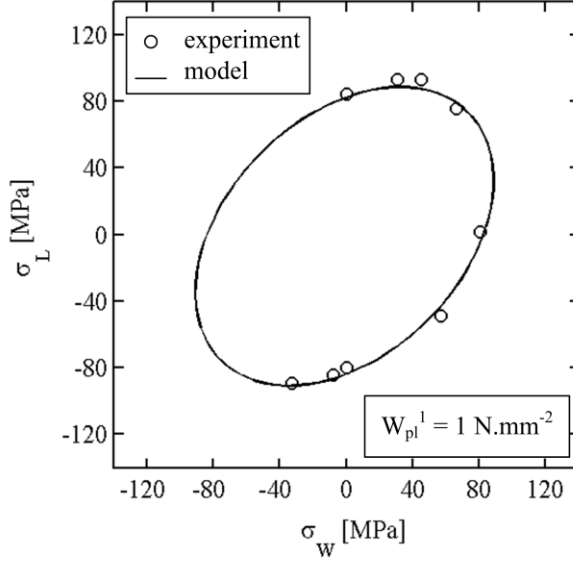
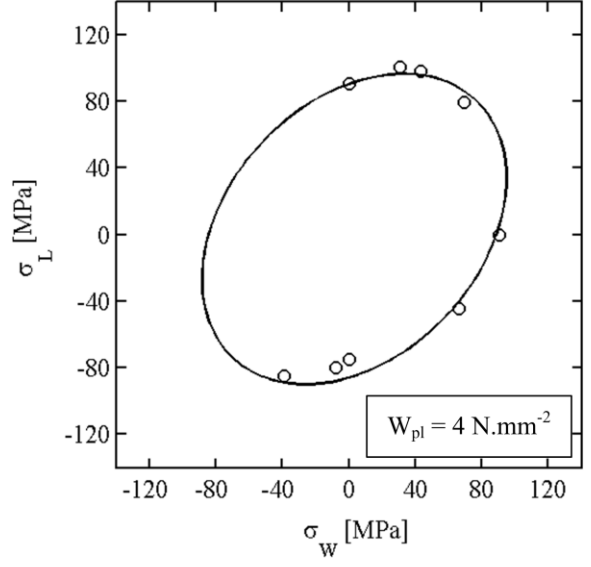


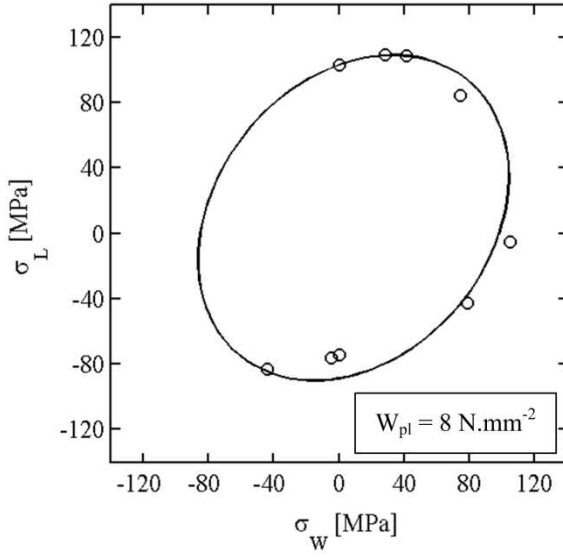
Fig. 3.10 : Envelopes of equal plastic work (per unit initial volume) for the face sheets in the true stress plane (σ_W, σ_L). The open dots present the results from virtual experiments, the black solid lines in (a) and (d) represent the least square fit of the yield function given by Eq. (3.16). The solid envelopes in (b) and (c) have been computed based on the isotropic-distortional hardening model given by Eq. (3.24).



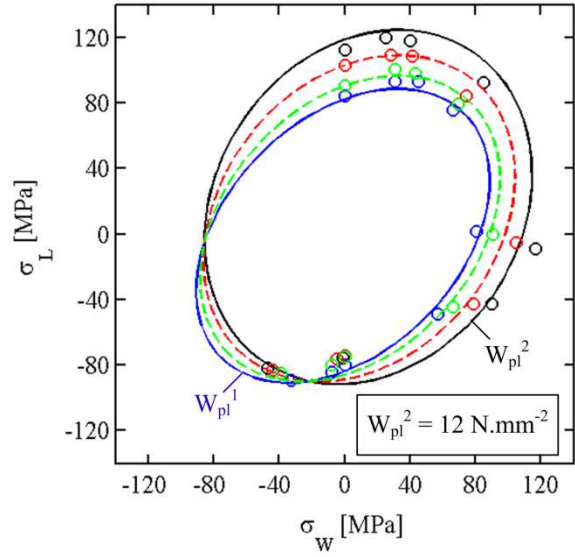
(a)



(b)



(c)



(d)

Fig. 3.11 : Envelopes of equal plastic work (per unit initial volume) for the core structure in the true stress plane (σ_W, σ_L). The open dots present the results from virtual experiments, the black solid lines in (a) and (d) represent the least square fit of the yield function given by Eq. (3.16). The solid envelopes in (b) and (c) have been computed based on the isotropic-distortional hardening model given by Eq. (3.25).

3.3.7 Summary of material model parameters

The proposed material model is specified through the following parameters:

- The elastic parameters, Young's modulus E and Poisson's ratio ν , that describe the planar isotropic elastic behavior;
- The yield functions f_1 and f_2 ; each function f_i is specified through five parameters: G_i, H_i, N_i, α_i and k_i ;
- The isotropic-distortional hardening function $\delta[W_{pl}]$ which describes combined isotropic-distortional hardening.

The isotropic-distortional hardening function may be presented as a parametric or non-parametric function. For the present sandwich material, the parametric function

$$\delta_f[W_{Pl}] = \begin{cases} \log \left\{ 1 + \delta_1^f \left(\frac{W_{Pl} - W_{pl,f}^1}{W_{pl,f}^2} \right) \right\} & \text{for } W_{pl} < W_{pl,f}^2 \\ 1 + \delta_2^f \left\{ \left(\frac{W_{Pl}}{W_{pl,f}^2} \right) - 1 \right\} & \text{for } W_{pl,f}^2 \leq W_{pl} \end{cases} \quad (3.24)$$

provides a good approximation of the face sheet response. The yield envelopes for $W_{pl} = 15N/mm^2$ and $W_{pl} = 30N/mm^2$ shown in Fig. 3.10 have been computed using the above expression for the isotropic-distortional hardening function.

For the core structure, we propose the function

$$\delta_c[W_{Pl}] = \begin{cases} \delta_1^c \left(\frac{W_{Pl} - W_{pl,c}^1}{W_{pl,c}^2} \right) & \text{for } W_{pl} < W_{pl,c}^2 \\ 1 + \delta_2^c \left\{ \left(\frac{W_{Pl}}{W_{pl,c}^2} \right) - 1 \right\} & \text{for } W_{pl,c}^2 \leq W_{pl} \end{cases} \quad (3.25)$$

to describe the apparent strain hardening. Figure 3.11 includes the intermediate yield envelopes for $W_{pl} = 4N/mm^2$ and $W_{pl} = 8N/mm^2$ that have been determined using Eq. (3.17) in combination with Eq. (3.25). All model parameters as calibrated for the present face sheet and core materials are summarized in Tables 3.1 and 3.2.

	W_{pl}^1	G_1	H_1	N_1	α_1	k_1
	N/mm^2	-	-	-	-	MPa
Core	1	1	0.6	1.5	0.03	105
Face	0.5	0.77	0.53	1.5	-0.1	373

	W_{pl}^2	G_2	H_2	N_2	α_2	k_2
	N/mm^2	-	-	-	-	MPa
Core	12	1.2	0.22	1.5	-0.43	114
Face	50	0.85	0.3	1.5	-0.33	459

Table 3.1 : Yield function parameters.

	δ_1	δ_2
Core	1.09	0.26
Face	9.09	0.09

Table 3.2 : Isotropic-distortional hardening function parameters

3.4. Validation and discussion

The constitutive model is implemented into the finite element software Abaqus/explicit through its VUMAT user material subroutine interface. In the VUMAT code, we adopt a standard return mapping algorithm with a backward-Euler time integration scheme (Simo and Hughes, 1998). It is subsequently used in conjunction with a composite shell element. The cross-section of the composite shell element is composed of three layers representing the top and bottom face sheets (each 0.2mm thick) along with a 1.2mm thick core layer. Three thickness integration points (for numerical integration with the Simpson rule) are employed per layer.

3.4.1 Comparison: macroscopic model versus virtual experiments

All in-plane experiments are simulated using the composite shell model. The results are reported in terms of the section normal forces F_L and F_W as a function of the corresponding engineering normal strains E_L and E_W . The solid blue lines in Fig. 3.12 depict the results for the composite shell element while the dashed blue lines show the corresponding results from the virtual experiments. In addition, we also computed the individual contributions of the face sheets (red curves) and the core structure (black curves).

We observe good overall agreement of the force-strain curves for most loading cases. The best agreement of model and virtual experiments is observed for transverse plane strain loading ($\beta = 0^\circ$ and $\beta = 180^\circ$). For uniaxial tension and compression, the predicted force agrees well with that of the virtual experiment, but it is underestimated by up to 15% at large strains. The model predictions are less accurate for combined loading. However, the force level predictions are still reasonable when quantifying the error in absolute terms. For example, the relative error in F_L exceeds 100% for $\beta = 101.3^\circ$, but the absolute difference is less than $20N/mm$. The comparison of the force-strain curves for the face sheets demonstrates a good agreement for almost all experiments. The observed differences in force level for the sandwich may thus be attributed to deficiencies in the model predictions of the effective behavior of the core structure. The plots of the yield envelopes in Fig. 3.11 demonstrate that the error in the core model predictions are not due to the yield functions. Instead, it is speculated that the flow rule is not very accurate. Note that all biaxial experiments are strain-driven and the flow rule therefore determines the loading path in stress space.

3.4.2 Discussion

An attempt was made to come up with a simple micromechanics-based two-scale finite element model of the core structure. For example, a simplified three-dimensional shell element model of the unit cell could be assigned to each thickness integration point of macroscopic composite shell model (see for instance Mohr (2006)). However, our preliminary results have shown that a three-dimensional shell element model (at the micro-scale) provides only a poor quantitative prediction of the effective stress-strain response obtained from our virtual experiments (that make use of fine solid elements). Similarly, analytical solutions of strongly simplified mechanical models of the core structure (e.g. a truncated cone of uniform thickness) turned out to be inadequate from both a qualitative and quantitative point of view. Here, we proposed a simple phenomenological modeling framework to describe the effective behavior of the face sheets and core layers, respectively. Such models are only of little value as far as their predictive capabilities outside the range of calibration are concerned. However, at this stage, where the sandwich material itself is still under development, it appears to be reasonable to propose a phenomenological model to evaluate the mechanical performance of three-dimensional structures made from this sandwich sheet material. The modeling of the effective behavior of constructed cellular materials is particularly challenging due to the evolution of the material microstructure. This evolution causes the distortion of the macroscopic yield surface which is described through a phenomenological isotropic-distortional hardening model in the present work. The introduction of two fixed yield surfaces f_1 and f_2 results in a rather simple model which can be easily calibrated based on experiments. Note that the plastic work density is the only internal state variable of the model. This is a very strong simplifying assumption which is expected to break down in case of non-radial loading paths. The final deformed configurations for $\beta = 11.3^\circ$ and 101.3° shown in Fig. 3.8b have been subject to approximately the same amount of plastic work density ($W_{pl} = 25 \text{ N/mm}^2$). Clearly, the state of the material is very different among these configurations. Further improvements of the above model would therefore not only require a modified flow rule, but also the introduction of additional state variables to provide a more accurate description of the microstructural evolution.

3.5. Conclusions

In this chapter, the focus is made on the plastic behavior of the bi-directionally corrugated sandwich structure under different loadings. Finite elements experiments are carried out using a full meshing of the core geometry. Uniaxial loadings such as out-of plane compression and shearing, in-plane traction and compression revealed a different behavior from that of traditional cellular materials. A very special feature of this new material is the strong contribution of the core layer to the in-plane deformation resistance of the sandwich material. The core structure contributes up to 43% of the effective yield strength of the sandwich sheet material for in-plane loading. Besides, the out-of-plane compressive response shows no collapse or progressive folding of the cellular microstructure. In addition, anisotropy in the sandwich material response is observed.

Based on the results from biaxial tensile experiment simulations, a phenomenological constitutive model is proposed for both the face sheets and the core structure. The yield function is chosen such that it defines the envelopes of plastic work density. The equivalent stress depends both on the deviatoric and diagonal terms of the Cauchy stress tensor in order to take into account the anisotropy of the structure and the pronounced tension/compression asymmetry of its behavior. Furthermore, a new isotropic-distortional hardening modeling framework is proposed to provide a first approximation of the stress-strain response for radial loading paths. The constitutive model is implemented into a commercial finite element software and used in conjunction with a composite shell element model to describe the effective in-plane behavior of the sandwich sheet material.

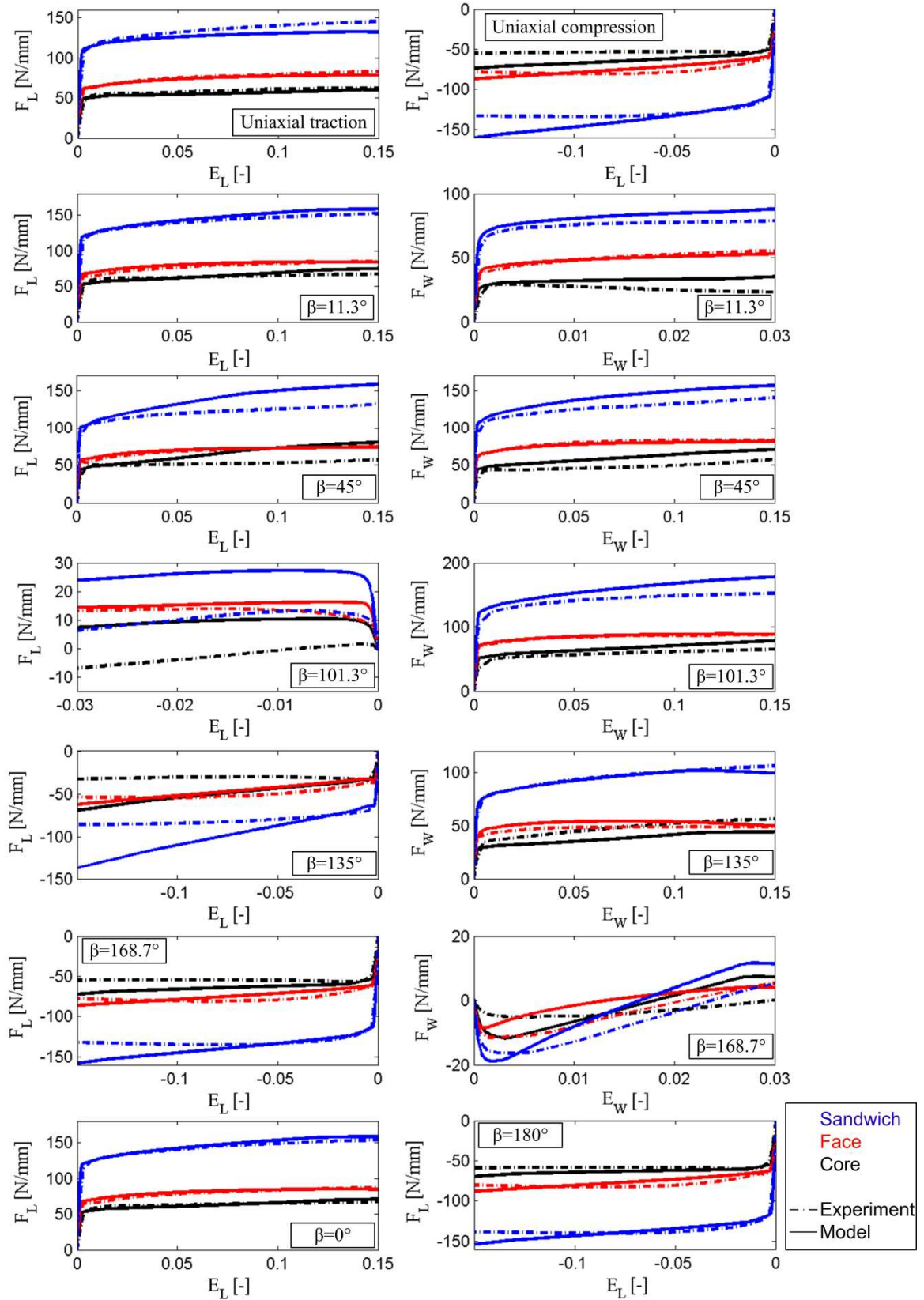


Fig. 3.12 : Comparison of the force (per unit width) versus engineering strain curves for all virtual experiments. Different colors show the force for the entire sandwich section (blue), the face sheets (red) and the core structure (black). Dashed lines depict the results from virtual experiments, while the solid lines correspond to the macroscopic models.

Chapter IV : Model Parameter Identification and Application to Draw Bending

The use of the phenomenological constitutive model presented in chapter III requires the identification of the effective behavior of the face sheets and that of the core structure. The main outstanding challenge is the identification of the model parameters based on experimental data. We have shown that the mechanical response of the face sheets is altered through the coupling with the periodic core structure. Similarly, the behavior of the core structure depends strongly on the mechanical coupling with the face sheets. Consequently, it is not possible to identify the respective material model parameters from separate experiments on the face sheets and the core structure.

In the present chapter, a procedure is developed to identify the plastic material model parameters based on tension and bending experiments on the entire sandwich material. Extensive work make use of an inverse method to determine material properties for instance hardening parameters of metal sheets have been identified thanks to three-point bending experiments (Omerspahic et al., 2006, Eggertsen et al., 2010) and vibration analysis were used to identify the different layers properties of sandwich structures (Lauwagie et al., 2004, Shi et al., 2006, Rébillat et al., 2011).

Finally, draw bending experiments will allow for a structural validation and discussion on the constitutive model.

The main results of this chapter have been summarized in the form of a journal paper under the title “Composite Shell Element Model of Bi-directionally Corrugated Sandwich Sheets: Model Parameter Identification and Application to Draw Bending”, Journal of the Mechanics of Solids and Structures, (*submitted for publication*).

4.1. Calibration experiments

As an alternative to real physical experiments, virtual experiments are used throughout this study. This is mainly done because of the limited availability of bi-directionally corrugated prototype material of consistent properties (with regards to face sheet-to-core layer joint quality, thermal treatment and thickness variations).

Two different virtual experiments are performed to characterize the mechanical properties of the sandwich material: (1) uniaxial in-plane tension, and (2) four-point bending. In this section, all the virtual experiments are performed on specimens made from the virtually manufactured unit cell model of the bi-directionally corrugated sandwich sheet, as described in chapter I. We use the same geometric characteristics as in chapter III, corresponding to the structure offering the highest shear stiffness-to-weight ratio. Note that for computational efficiency, we use coarser meshing for large specimen models (three solid elements through the sheet thickness). However, the simulation of a unit cell under uniaxial in-plane tension revealed a less than 1% difference load.

4.1.1 Calibration experiment #1: Uniaxial tension

This uniaxial in-plane tension experiment along the L-direction is described in Subsection 3.1.1 of chapter III.

The computed engineering stress versus engineering strain curve is shown as a black solid line in Fig. 4.2. The material response becomes inelastic at an average stress of about 110MPa. The stress-strain curve increases monotonically under uniaxial tension until a stress of 160MPa is reached at a strain of 0.15.

4.1.2 Calibration experiment #2: Four-point bending

The same experimental set-up as described in Subsection 2.3.1 of chapter II and illustrated by figure 4.1 is used to perform four-point bending experiments. The specimen will be positioned such that it is bent around the W-axis. Due to the symmetry of the mechanical system, the finite element model comprises only one half of the 100 mm-long specimens and the boundary condition $u_L = 0$ is applied to all nodes located on the W-T-symmetry plane. We assume a wide beam (plane strain conditions along the W-direction) and make use of the periodicity of the core structure to reduce our computational model to a 1.784 mm wide beam

(corresponds to the width of the unit cell) with plane strain boundary conditions along the W-direction ($u_W = 0$ for all nodes on L-T-boundary planes).

All degrees of freedom of the rollers are fixed except for the vertical motion of the upper loading roller. A total displacement of $u_T = 5\text{mm}$ is applied.

The monotonically increasing punch force versus displacement curve is shown in Fig. 4.3 (black curve), while Fig. 4.3 shows the deformed sandwich beam at various stages of the virtual experiment. The superposed color contours shows the equivalent plastic strain in the face sheets only. It is worth noting that the sandwich beam exhibits a similar response as conventional homogeneous materials: the cross-sections remain flat and perpendicular to the beam mid-axis. Unlike in conventional sandwich materials, the shear deformation of the core layer is negligible. This “shear-rigid” behavior is a characteristic feature of the bi-directionally sandwich sheet material and is critical for the successful forming of three-dimensional structures from flat sheets (Mohr, 2005).

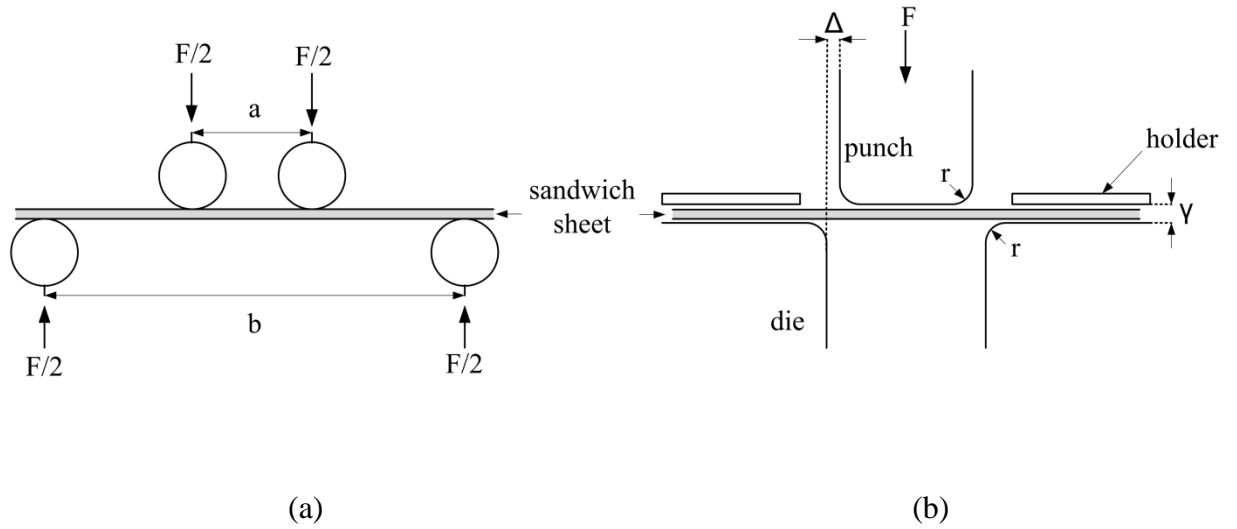


Figure 4.1 : Technical drawing of the experimental set-ups: (a) four-point bending experiment, (b) draw bending experiment.

4.2.. Material model parameter identification

4.2.1 Summary of material model parameters

We recall that the material model is determined through the following parameters and functions:

- Two elastic constants, E and ν
- Ten yield surface shape parameters $\{G_1, H_1, N_1, \alpha_1, W_{pl}^1\}$ and $\{G_2, H_2, N_2, \alpha_2, W_{pl}^2\}$
- Isotropic-distortional hardening function $\delta[W_{pl}]$
- Thickness change parameter κ

The determination of the material model parameters based on the experimental results for uniaxial tension and four-point bending is shown. The constants of the isotropic elasticity model are easily obtained from a uniaxial tension experiment. The eight yield surface shape parameters on the other hand need to be determined from multi-axial experiments. However, it is postulated that these depend on the geometry of the core structure only. In a first approximation, it is assumed that these are independent of the choice of the basis material. We thus make use of the same parameters as proposed in chapter III, see Tab. 3.1. An inverse method is used to identify the distortional hardening functions parameters.

4.2.2 Elastic constants and thickness change parameter

The linear elastic range of the average engineering stress versus strain curve for uniaxial tension exhibits a modulus $E_s = 73 \text{ GPa}$ and a Poisson's ratio $\nu \approx 0.3$ (determined from in-plane width strain versus in-plane axial strain curve). The same Poisson's ratio is assumed for the core and face sheets. Furthermore, it is assumed that the face sheets remain flat in the elastic range and exhibit the basis material modulus $E_f = 210 \text{ GPa}$. Using the rule of mixtures,

$$E_c = \frac{2t_f + c}{c} E_s - \frac{2t_f}{c} E_f. \quad (4.1)$$

we can compute the homogeneous-equivalent Young's modulus of the core layer as $E_c = 31.2 \text{ GPa}$.

The thickness change parameter can also be determined from the uniaxial experiments. We assign the volume change of the sandwich material to the core structure only by plastic incompressibility of the face sheets ($\kappa = 0$). A fit to the plot of the volumetric strain for the core layer as a function of the plastic work under uniaxial tension leads to $\kappa = 0.0008 \text{ MPa}^{-1}$ (Fig. 4.2b).

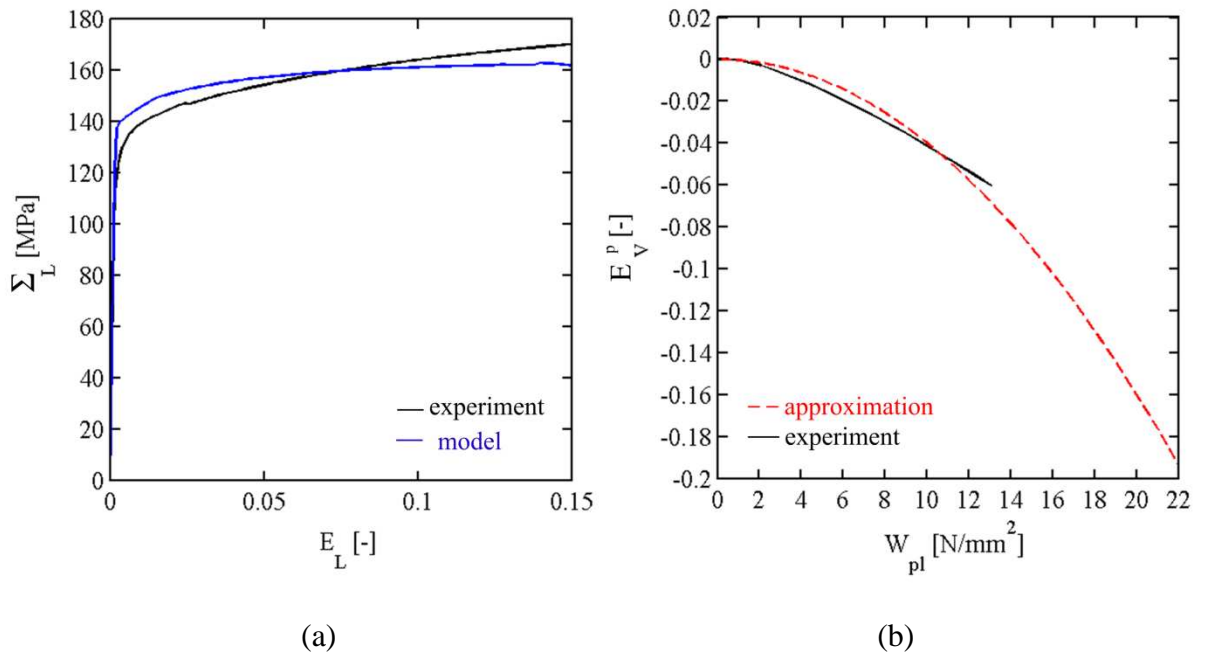


Figure 4.2 : (a) Stress-strain curves for the uniaxial tensile experiment (in black the “virtual” experiment results, in blue the model results) along with (b) the plastic volume change as a function of the plastic work density.

4.2.3 Isotropic-distortional hardening functions

The current size of the elastic domain is controlled by the deformation resistances $\{k_1^i, k_2^i\}$ and the isotropic-distortional hardening function $\delta[W_{pl}]$. This function needs to be identified

for the core structure and the face sheets. Since the plasticity models for the core structure and the face sheets describe the respective homogeneous equivalent behavior as built into the sandwich material, it is impossible to perform separate experiments for the core and face sheets. The hardening functions are thus determined through inverse analysis of the results from uniaxial tension and four-point bending instead. For this, it is useful to introduce parametric forms of $\delta[W_{pl}]$. Based on the work presented in Chapter III, and keeping in mind the condition on the isotropic-distortional hardening function $\delta[W_{pl}^1] = 0$ and $\delta[W_{pl}^2] = 1$, the parameters δ_0^i are defined as functions of the parameters δ_1^i and we use the form

$$\delta_f[W_{pl}] = \begin{cases} \log \left\{ 1 + \delta_1^f \left(\frac{W_{pl} - W_{pl,f}^1}{W_{pl,f}^2} \right) \right\} & \text{for } W_{pl} < W_{pl,f}^2 \\ 1 + \delta_2^f \left\{ \left(\frac{W_{pl}}{W_{pl,f}^2} \right) - 1 \right\} & \text{for } W_{pl,f}^2 \leq W_{pl} \end{cases} \quad (4.2)$$

for the face sheets (along with the constraint $\delta_f[W_{pl,f}^1] = 0$). It is entirely defined by the parameter set $\{\delta_1^f, \delta_2^f\}$. For the core structure, we propose the parametric form

$$\delta_c[W_{pl}] = \begin{cases} \delta_1^c \left(\frac{W_{pl} - W_{pl,c}^1}{W_{pl,c}^2} \right) & \text{for } W_{pl} < W_{pl,c}^2 \\ 1 + \delta_2^c \left\{ \left(\frac{W_{pl}}{W_{pl,c}^2} \right) - 1 \right\} & \text{for } W_{pl,c}^2 \leq W_{pl} \end{cases} \quad (4.3)$$

to describe the combined isotropic-distortional hardening using the parameters $\{\delta_1^c, \delta_2^c\}$.

In sum, four parameters need to be identified for each layer of the sandwich structure:

- For the face sheets: $\{k_1^f, k_2^f, \delta_1^f, \delta_2^f\}$, and
- For the core layer: $\{k_1^c, k_2^c, \delta_1^c, \delta_2^c\}$

These eight parameters will be identified through an inverse procedure.

4.2.4 Composite shell element models

The execution of the inverse parameter identification procedure requires shell element models of the tension and four-point bending experiments. The composite shell element is composed of three layers: (1) 0.2mm thick top face sheet, (2) 1.31mm thick core structure, and (3) 0.2mm thick bottom face sheet. One thickness integration point is used per face sheets and five thickness integration points for the core structure (for numerical integration with the Simpson rule). We use a first-order element with reduced integration. In total, the constitutive model needs to be evaluated at seven integration points per composite shell element.

4.2.4.1. Shell model for uniaxial tension

The strain fields are homogeneous prior to necking in a uniaxial tension experiment. The analysis of a single element FE mesh is therefore sufficient to simulate the material behavior under uniaxial tension. The simulation results for uniaxial tension are reported in terms of the section normal engineering stress Σ_L as a function of the corresponding engineering strain E_L .

4.2.4.2. Shell element model for four-point bending

A 50mm-long and 1mm-wide composite shell model is used to simulate the four-point bending experiment. As for the virtual experiments, the support points are represented as cylindrical rigid surfaces. The contact between the rigid support points the respective shell upper and lower surfaces is modeled as kinematic contact with a friction coefficient of 0.1. To improve the modeling of the effect of the support point curvature, 5.5mm-long areas underneath the rigid cylinders are meshed with 0.2mm-wide elements while the rest of the composite shell is meshed with 2mm-wide elements. The results are reported in terms of the sandwich normal force per unit width F_T as a function of the upper support point displacement u_T .

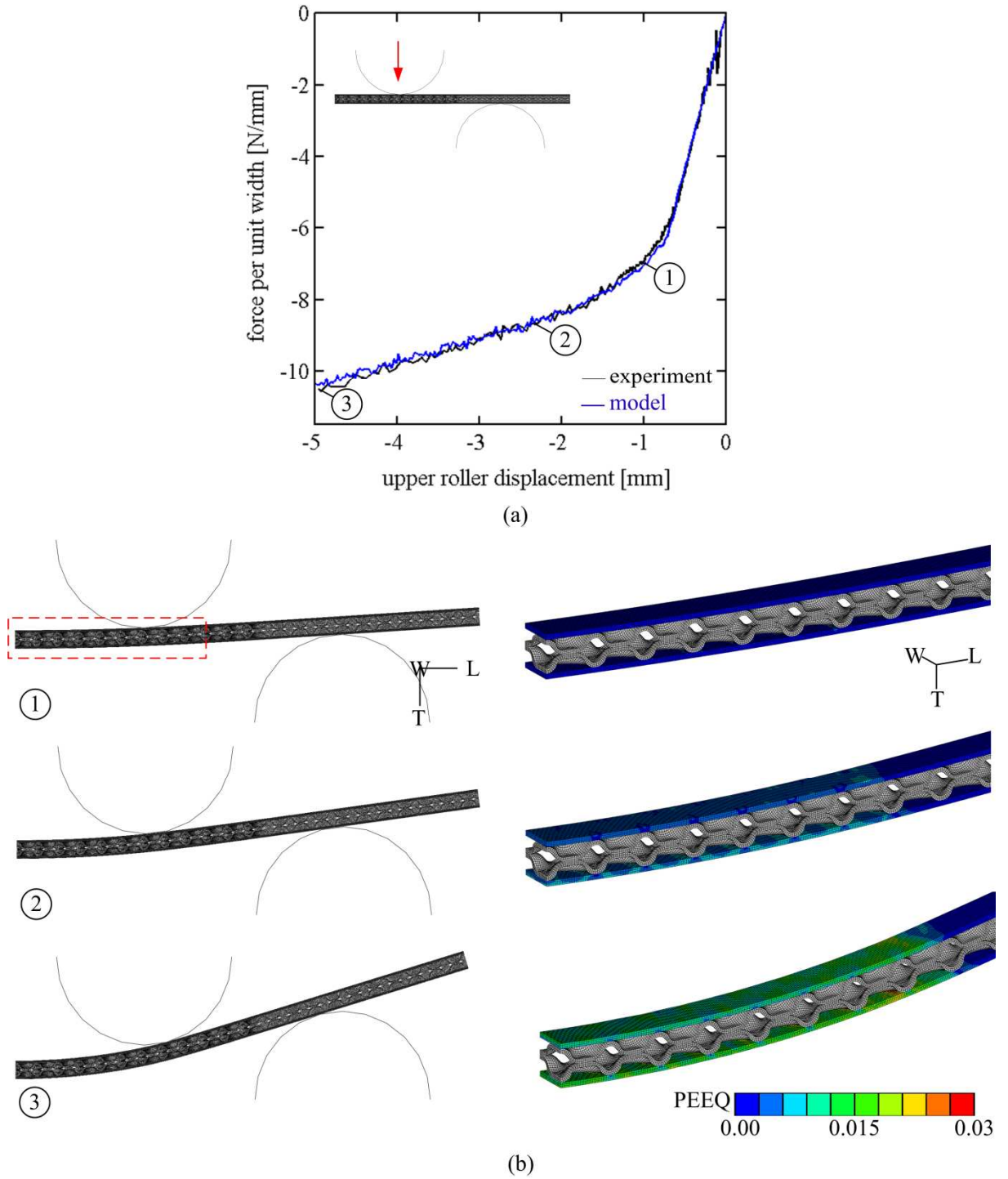


Figure 4.3 : (a) Force per unit width-displacement curves for the four-point bending experiment (in black the “virtual” experiment results, in blue the model results) along with (b) sequence of the “virtual” experiment.

4.2.5 Inverse model parameter identification

The inverse identification of the model parameters $\{k_1^f, k_2^f, \delta_1^f, \delta_2^f\}$ and $\{k_1^c, k_2^c, \delta_1^c, \delta_2^c\}$ is formulated as a minimization problem. For this, we define a cost function Γ to quantify the difference between the shell element model predictions and the experimental results,

$$\Gamma = \frac{1}{n_t} S_t + \frac{1}{n_b} S_b \quad (4.4)$$

with the residuals for uniaxial tension,

$$S_t = \sum_{i=1}^{n_t} \left(\frac{\Sigma_{sim}[E_{exp}^i]}{\Sigma_{exp}[E_{exp}^i]} - 1 \right)^2 \quad (4.5)$$

and for four-point bending,

$$S_b = \sum_{i=1}^{n_b} \left(\frac{F_{sim}[u_{exp}^i]}{F_{exp}[u_{exp}^i]} - 1 \right)^2 \quad (4.6)$$

The subscripts “exp” and “sim” are used to differentiate between experimental and simulation results. A total of $n_t = 200$ and $n_b = 223$ data points has been used to represent the respective experimental curves.

	k_1	k_2	δ_1	δ_2
	<i>MPa</i>	<i>MPa</i>	-	-
Core	107.45	113.9	1.056	0.264
Face	413.54	495.75	8.960	0.087

Table 4.1 : Calibrated hardening parameters.

A Nelder-Mead optimization algorithm (Matlab, 2010) is employed to perform the optimization without calculating the gradient of the cost function in the parameter space. The final set of parameters after 430 optimization runs is reported in Tab. 4.1. The corresponding error is $\Gamma = 0.0091$. A plot of the corresponding isotropic-distortional hardening functions for the core structure as well as for the face sheet is shown in Fig. 4.4.

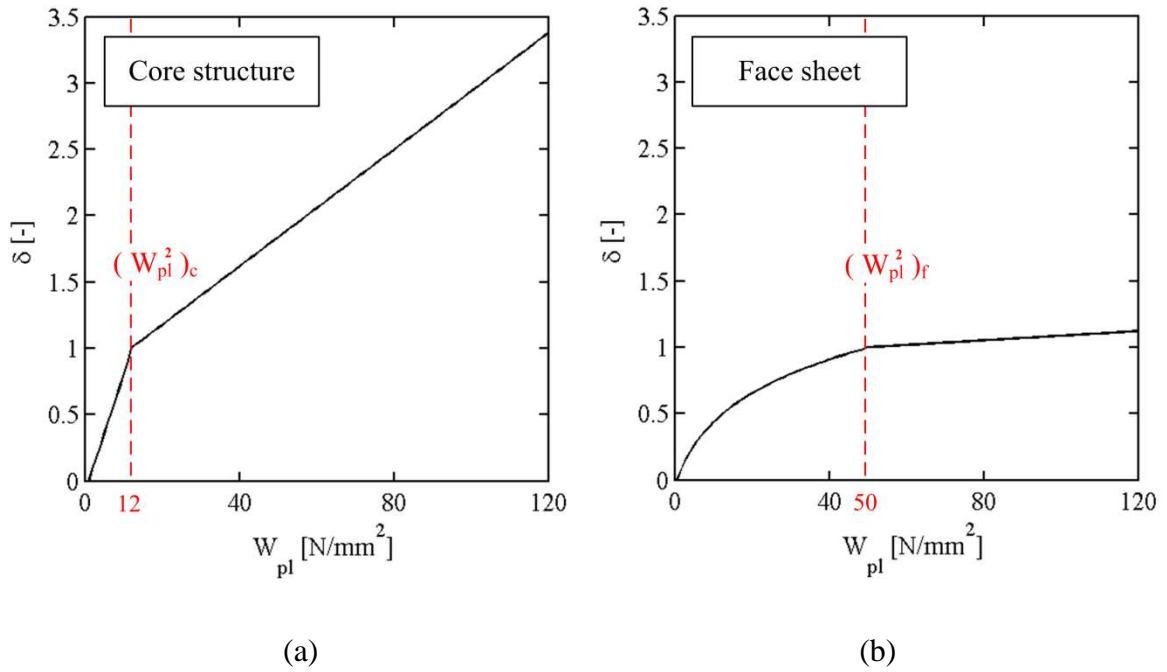


Figure 4.4 : Distortional hardenings function as a function of the plastic work per initial volume for the core structure (a) and the face sheet (b). Note that the curves start near the origin (0,0) since the plastic work densities W_{pl}^1 are almost zero (see Table 3.1).

The blue line in Fig. 4.2 depicts the results for the composite shell model while the black line shows the corresponding result from the virtual experiment. Note the good overall agreement of the stress-strain curve with a maximum difference of 5% for $E_L = 0.15$. The comparison of the results for four-point bending is shown in Fig. 4.3. We observe an excellent overall agreement of the force-displacement curves with a maximum difference of 1.5% for $u_T = 5mm$. After an initial linear macroscopic elastic response up to $u_T = 1mm$, the load per unit width rises monotonically.

4.3. Structural validation: draw bending

Draw bending is chosen as basic forming experiment to validate the composite shell model at the structural level. As compared to more complex deep drawing operations, this particular forming experiment has the advantage that virtual experiments on detailed finite element models can still be performed without access to super computers. Further validations for more complex geometries need to be performed in the future once prototype sandwich sheets become available.

4.3.1 Virtual experiment

A 70mm-long sandwich sheet specimen of a total thickness of $H = 1.71mm$ is used for draw bending. Figure 4.1b shows a picture of the experimental set up. The specimen is supported between a U-shaped die and a passive back holder. The black holder is positioned at a distance of $0.05H$ above the sheet. The edge radii r of the die and the 27mm-wide punch are the same. The validation experiments are performed for two different tool geometries,

1. $r = 12\text{ mm}$ and $\Delta = 2H$
2. $r = 13\text{ mm}$ and $\Delta = 3.5H$

with Δ denoting the distance between the punch and the vertical die wall. All degrees of freedom of the rigid surfaces are fixed except for the vertical motion of the punch. Explicit time integration is used because of the size of the computational model (>300000 elements) and the modeling of contact. The contact between the tool and the sandwich surfaces is modeled using a kinematic contact model with a friction coefficient of 0.1. A total displacement of $u_T = 40mm$ is applied to the punch.

Figure 4.5b presents the deformed configurations at various stages throughout the experiment for the first tool configuration. Initially, the sandwich sheet is bent around the punch and the die. Traction of the bottom face sheet and compression of the top face sheet under the punch and traction of the top face sheet and compression of the bottom face sheet above the die are dominant deformation modes. Once the sandwich sheet has taken the shape of the punch, the draw bending experiment enters a steady-state regime as the sandwich structure is consecutively bent and unbent. The comparison of the top and bottom plots in

Fig.4.5a reveal that a lower force is required for the draw bending when using the second tool configuration.

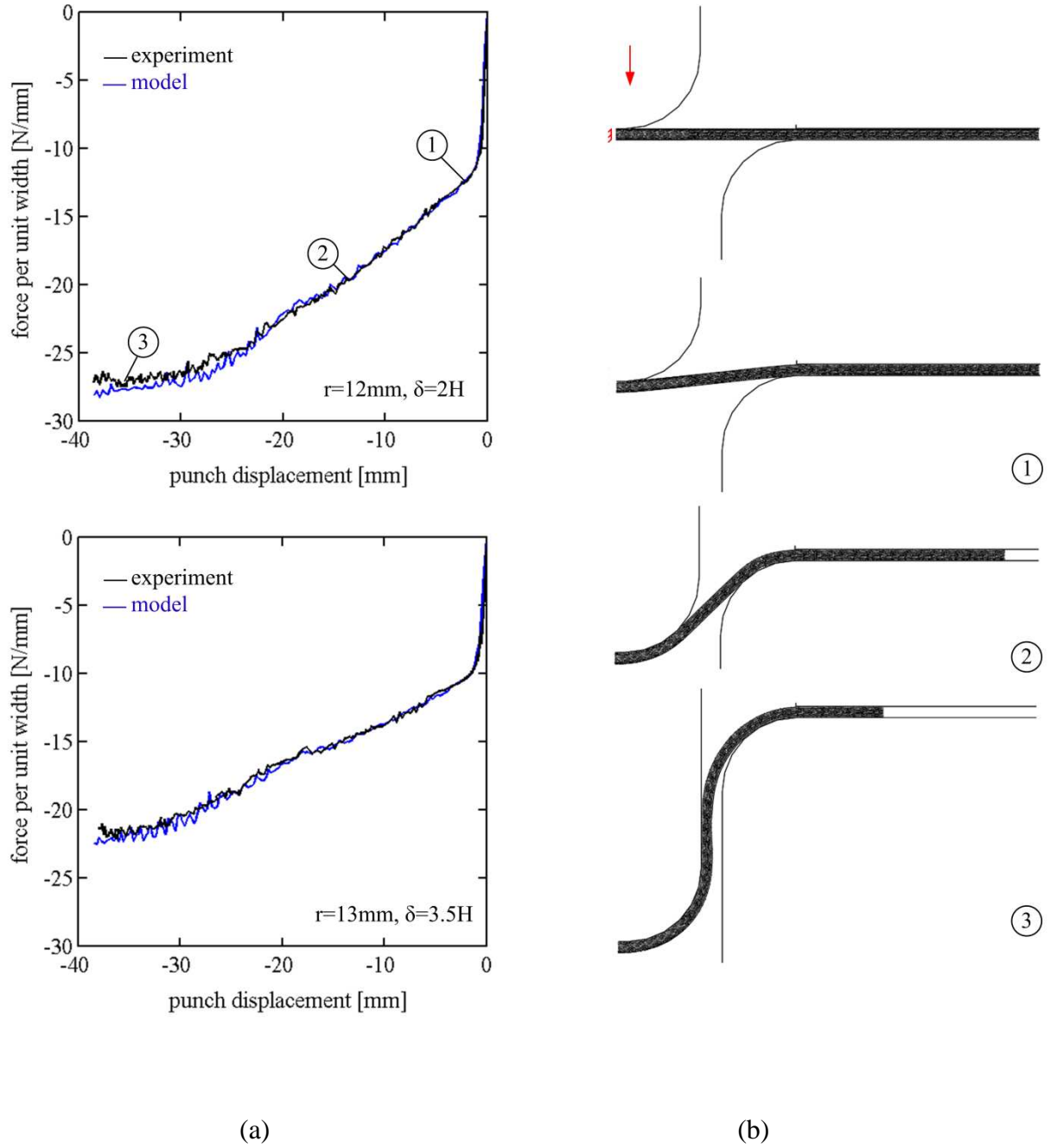


Figure 4.5 : (a) Force per unit width-displacement curves for the draw bending experiments (in black the “virtual” experiment results, in blue the model results) along with (b) sequence of the first “virtual” experiment.

4.3.2 *Composite shell model predictions and discussion*

The same boundary conditions as in the virtual experiments are used for the finite element simulation with composite shell elements of an edge length of 1mm. The blue lines in Fig.4.5a show the results for the composite shell model while the black lines show the corresponding result from the virtual experiment. A very good agreement of the force-displacement curves is observed for both tool geometries.

This good agreement is seen as a first promising step towards the modeling of the forming of sandwich sheet materials with shell elements. This task is very challenging from the point of view of constitutive modeling due to the variety and complexity of deformation mechanisms at the microstructural level. The evolution of the microstructure is taken into account through a phenomenological combined isotropic-distortional hardening model. In the present chapter, we assume the same basic yield surface shape as that for a similar sandwich material which has been characterized through multi-axial experiments in the previous Chapter. The conduct of virtual multi-axial experiments appears to be a necessary step in identifying a material model for sandwich sheet materials with constructed core structures even if the real material is available. In the present study, we avoided the confrontation with real experimental data due to the unavailability of suitable samples. However, once “real” material becomes available, a two-step identification procedure is recommended:

1. Multi-axial virtual experiments to determine all material model parameters including those describing the shape of the yield surface. Note that the virtual experiments will only be able to represent the real material behavior in an approximate manner.
2. Uniaxial and four-point bending experiments on the real material and subsequent determination of the material model parameters as described in this paper. The results from the previous step will provide the yield surface shape parameters, while all other parameters will serve as starting values for the inverse procedure.

Another important issue in modeling the forming of sandwich sheets is the prediction of their forming limits. In addition to conventional sheet metal forming limits such as pronounced necking and fracture, sandwich sheets are prone to delamination failure and local

wrinkling (dimpling) of a compressed face sheet. However, it is worth noting that a successful draw bending experiment could be performed on a small prototype strip (Fig.3 and Fig. 4.6) using a similar experimental set-up as that assumed above.

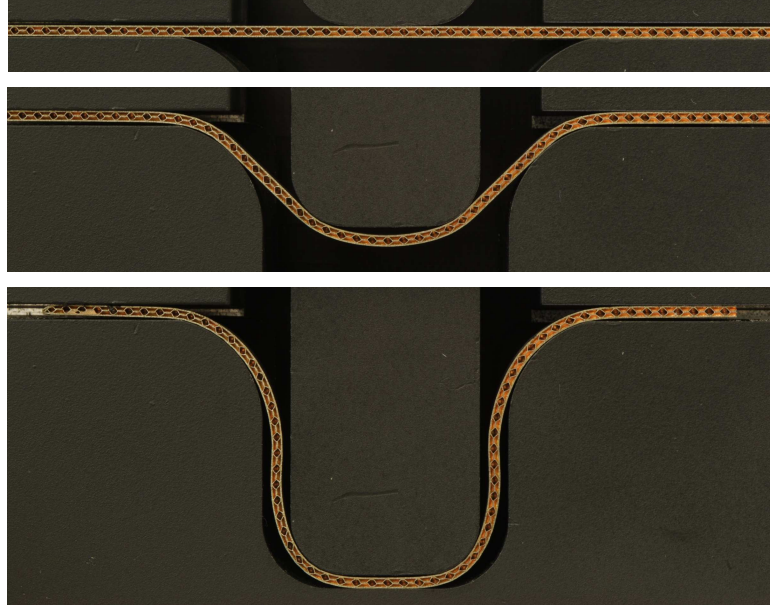


Figure 4.6 : Draw bending of a prototype sandwich sheet demonstrating the formability of the sandwich sheet material.

4.4. Conclusions

The present chapter discusses the identification of the parameters of the isotropic-distortional hardening model that describes the elasto-plastic deformation response of the bi-directionally corrugated sandwich sheet material. In a first approximation, we consider that the yield surface shape parameters depend on the geometry of the core structure only and are independent of the choice of the basis material. The focus is made on calibrating the distortional hardening parameters. An inverse method is used to identify the parameters where uniaxial tensile and four-point bending virtual experiments are compared to a composite shell model. The resulting set of parameters is validated thanks to draw-bending experiments.

Conclusion

The focus of this thesis is the investigation of the mechanical behavior of a newly-developed all-metal sandwich sheet material for forming applications. The structure is composed of two flat face sheets and two bi-directionally corrugated core layers. In order to study its behavior we make use of virtual experiments using a detailed finite element model of the unit cell of the periodic material microstructure. This approach allows us to gain an insight into the behavior of an idealized material which is free from imperfection.

The first part of this thesis deals with the design of an optimized core structure that offers the highest shear stiffness-to-weight ratio. A parametric study is performed where the computational model of the sandwich material is used to investigate the effect of the stamping tool geometry on the effective transverse shear modulus of the resulting sandwich core structure. It is found that the highest shear stiffness per unit weight is provided by core structures that feature (1) a small dome width to dome height ratio, and (2) a large bonding land diameter to dome width ratio. The results also reveal that the transverse shear stiffness of the bi-directionally corrugated core structure is up to 30% lower than that of a hexagonal honeycomb of the same density (for relative densities ranging from 0.2 to 0.35). However, unlike for hexagonal honeycombs, the shear stiffness is approximately the same for both in-plane directions.

The plastic behavior of the “optimal” sandwich structure is investigated and special characteristics of the material are outlined. It is found that the core structure is used very efficiently, contributing up to 43% of the effective yield strength of the sandwich sheet material for in-plane loading; furthermore a different behavior from that of traditional cellular materials is found for its out-of-plane compressive response. Based on the results from virtual experiments for biaxial tension, a phenomenological constitutive model is proposed. The experimental data are used to determine the macroscopic yield surfaces based on an equal plastic work definition for both the core structure and the face sheets. The severe changes of the microstructural geometry become apparent as distortional hardening at the macroscopic level. A new isotropic-distortional hardening modeling framework based on a linear combination of two distinct yield functions is introduced to provide a first approximation of the stress-strain response of the sandwich structure for radial loading paths.

In addition, a method for identifying the parameters of the isotropic-distortional hardening model is proposed. While virtual multi-axial experiments are recommended to determine the exact shape of the yield surface, the elastic properties and the isotropic-distortional hardening functions can be determined based on the results from uniaxial tension and four-point bending experiments. A gradient-free optimization method is employed to identify the material model parameters through inverse analysis. Finally, detailed finite element simulations of a draw bending experiment are carried out to validate the composite shell element model at the structural level.

Future work

The present thesis work is a first step towards the modeling of the plasticity of metallic sandwich sheet materials. However, in order to ensure the validity of the developed model, additional experimental and numerical studies are needed.

It is recommended to characterize the limits of the applicability of the proposed constitutive model in future work. For instance, the hypothesis of isotropic hardening needs to be validated for very large strains. The model also needs to be validated for complex process experiments as it has been developed for radial loading paths only. As highlighted in Chapter III of this thesis, a more elaborate flow rule and the introduction of additional state variables would allow for a more precise description of the microstructural evolution. The confrontation of the model predictions with experimental results on real prototype sheets is also an important task that needs to be addressed in the future.

Apart from validating the plasticity model further, future research needs to investigate the forming limits of metallic sandwich sheet materials. Once the prototype material becomes available in the form of large sheets, Nakazima or Hasek tests could be performed. It will be of particular interest to identify sandwich sheet specific damage mechanisms (such as face sheet dimpling and delamination) and formulate the corresponding forming limit diagrams.

Journal publications related to this work

[1] “Optimization of the Effective Shear Properties of a Bi-directionally Corrugated Sandwich Core Structure”, Journal of Applied Mechanics (*in press*).

[2] “Plasticity of Formable All-metal Sandwich Sheets: Virtual Experiments and Constitutive Modeling”, International Journal of Solid and Structures (*in press*).

[3] “Composite Shell Element Model of Bi-directionally Corrugated Sandwich Sheets: Model Parameter Identification and Application to Draw Bending”, Journal of the Mechanics of Solids and Structures, (*submitted for publication*).

References

- Abaqus, Reference manuals v6.8-3, Abaqus Inc, 2008.
- Akisanya A.R., Fleck N.A. 2006. Plastic collapse for thin-walled frusta and egg-box material under shear and normal loading. *International Journal of Mechanical Sciences*, 48, 799-808.
- Allen, H.G. 1969. Analysis and design of structural sandwich panels. Pergamon Press, Oxford.
- Aretz H. 2004. Applications of a new plane stress yield function to orthotropic steel and aluminum sheet alloys. *Modeling and Simulation in Materials Science and Engineering*, 12, 491–509.
- Aretz H. 2005. A non-quadratic plane stress yield function for orthotropic sheet metals. *J. Mater. Process. Technol.*, 168, 1–9.
- Aretz H. 2008. A simple isotropic-distortional hardening model and its application in elastic–plastic analysis of localized necking in orthotropic sheet metals. *International Journal of Plasticity*, 24, 1457–1480.
- Ashby M.F., Evans A.G., Fleck N.A., Gibson L.J., Hutchinson J.W. and Wadley H.N.G. 2000. *Metal Foams: A Design Guide*. Butterworth Hamilton.
- Bart-Smith H., Bastawros A.F., Mumm D.R., et al. 1998. Compressive deformation and yielding mechanisms in cellular Al alloys determined using X-ray tomography and surface strain mapping. *Acta Materialia*, 46, 10, 3583-3592.
- Bastawros A.F., Bart-Smith H., Evans A.G. 2000. Experimental analysis of deformation mechanisms in a closed cell Al alloy foam. *J. Mech Phys. Solids*, 48, 301-322.
- Basily B.B., Elsayed E.A. 2004. A continuous folding process for sheet materials. *International Journal of Materials and Product Technology*, 21, 217–238.
- Basily B.B., Elsayed E.A. 2004. Dynamic axial crushing of multi-layer core structures of folded chevron patterns. *International Journal of Materials and Product Technology*, 21, 169–185.
- Besse C., Mohr D., Optimization of the Effective Shear Properties of a Bi-directionally Corrugated Sandwich Core Structure, *submitted to publication*.
- Besse C., Mohr D., Plasticity of Formable All-metal Sandwich Sheets: Virtual Experiments and Constitutive Modeling, *submitted to publication*.
- Bitzer T. 1997. *Honeycomb Technology*. Chapman & Hall.
- Cantwell W.J., Davies P. 1996. A study of skin-core adhesion in glass fiber reinforced sandwich materials. *Applied Composite Materials*, 3, 6, 407-420.

- Carrado A., Faerber J., Niemeyer S., et al. 2011. Metal/polymer/metal hybrid systems: Towards potential formability applications. *Composite Structures*, 93, 2, 715-721.
- Caty O., Maire E., Youssef S., Bouchet R. 2008. Modeling the properties of closed-cell cellular materials from tomography images using finite shell elements. *Acta Materialia*, 56, 19, 5524–5534.
- Chiras S., Mumm D.R., Evans A.G., Wicks N., Hutchinson J.W., Dharmasena K., et al. 2002. The structural performance of optimized truss core panels. *International Journal of Solids and Structures*, 39, 4093–4115.
- Demiray S., Becker W., Hohe J. 2007. Numerical determination of initial and subsequent yield surfaces of open-celled model foams. *International Journal of Solids and Structures*, 44, 7-8, 2093-2108.
- Deshpande V.S., Fleck N.A. 2000. Isotropic constitutive models for metallic foams. *Journal of the Mechanics and Physics of Solids*, 48, 1253-1283.
- Deshpande V.S., Fleck N.A. 2001. Collapse of truss core sandwich beams in 3-point bending. *International Journal of Solids and Structures*, 38, 6275–6305.
- Dillard T., NGuyen F., Maire E., Forest S., Bienvenu Y., Bartout J.D., Croset M., Salvo L., Dendievel R., Cloetens P. 2005. 3D quantitative image analysis of open-cell nickel foams under tension and compression loading using X-ray microtomography. *Philos. Mag.*, 85, 2147–2175.
- Eggertsen P-A., Mattiasson K. 2010. An efficient inverse approach for material hardening parameter identification from a three-point bending test. *Engineering with Computers*, 26, 2, 159-170.
- Evans A.G., Hutchinson J.W., Ashby M.F. 1998. Multifunctionality of cellular metal systems, *Progress in Mtls. Sci.*, 43, 3, 171-221.
- Evans A.G., Hutchinson J.W., Fleck N.A., Ashby M.F., Wadley H.N.G. 2001. The topological design of multifunctional cellular metals. *Progress in Materials Science*, 46, 309–327.
- Gibson L. and Ashby M. 1988. *Cellular solids: Structure and properties*, Pergamon, Oxford, U.K.
- Gibson L.J. and Ashby M.F. 1997 *Cellular Solids, Structure and properties*, Cambridge University Press, Cambridge.
- Gong L., Kyriakides S., Jang W.Y. 2005. Compressive response of open-cell foams. Part I: Morphology and elastic properties. *Int. J. Solids Struct.* 42, 1355–1379.
- Grediac M. 1993. A finite element study of the transverse shear in honeycomb cores. *International Journal of Solids and Structures*, 30, 17, 77-88.
- Gurson A.L. 1977. Continuum theory of ductile rupture by void nucleation and growth: Part I - Yield criteria and flow rules for porous ductile media. *Engrg. Materials and Technology*, 99, 2-15.

- Gustafsson R.N.G. 2000. Ultralight stainless steel sandwich materials-HSSA. In: Meyer-Piening, H.R., Zenkert, D. (Eds.), *Sandwich construction* 5, EMAS, 169–176.
- Hale 1960. Anticlastic cellular core structure having biaxial rectilinear truss patterns.
- Heimbs S., Middendorf P., Kilchert S., Johnson A., Maier M. 2007. Experimental and numerical analysis of composite folded sandwich core structures under compression. *Applied Composite Materials*, 14 (5), 363–377.
- Hutchinson R.G., Fleck N.A. 2006. The structural performance of the periodic truss. *J. Mech. Phys. Solids*, 54, 756–782.
- Jackson K.R., Allwood J.M., Landert M. 2008. Incremental forming of sandwich panels. *Journal of Materials Processing Technology*, 204(1-3), 290-303.
- Kelsey S., Gellatly R.A. and Clark B.W. 1958. The shear modulus of foil honeycomb cores, *Aircraft Engineering*, 294-302.
- Kim K.J., Kim D., Choi S.H., Chunga K., Shin K.S., Barlat F., Oha K.H., Youn J.R. 2003. Formability of AA5182/polypropylene/AA5182 sandwich sheets, *Journal of Materials Processing Technology*, 139, 1–7.
- Kintscher M., Karger L., Wetzel A., Hartung D. 2007. Stiffness and failure behavior of folded sandwich cores under combined transverse shear and compression. *Composites Part A: Applied Science and Manufacturing*, 38 (5), 1288–1295.
- Lauwagie T., Sol H., Heylen W., Roebben G. 2004. Determination of the in-plane elastic properties of the different layers of laminated plates by means of vibration testing and model updating. *Journal of Sound and Vibration*, 274, 529–546.
- Lebée A., Sab K. 2010. Transverse shear stiffness of a chevron folded core used in sandwich construction. *International Journal of Solids and Structures*, 47(18-19), 2620-2629.
- Luxner M.H., Stampfl J., Pettermann H.E. 2009. Nonlinear simulations on the interaction of disorder and defects in open cell structures. *Computational Materials Science*, 47, 2, 418-428.
- Liu J.S., Lu T.J. 2004. Multi-objective and multi-loading optimization of ultralight weight truss materials. *International Journal of Solids and Structures*, 41, 618–635.
- Liu T., Deng Z.C., Lu T.J. 2006. Design optimization of truss-cored sandwiches with homogenization. *International Journal of Solids and Structures*, 43, 7891–7918.
- Markaki, A.E., Clyne, T.W., 2003. Mechanics of thin ultra-light stainless steel sandwich sheet material Part I. Stiffness. *Acta Materialia* 51, 1341–1350.
- McFarland R.K. 1963. Hexagonal Cell Structures Under Post-Buckling Axial Load, *AIAA Journal*, 1, 6.
- Miller W.K. 1981. Metal-Plastic Laminates for Vehicle Weight Reduction. *Society of Automotive Engineers*, 800077, 481–490.

- Mohr D., Doyoyo M. 2004. Large Plastic Deformation of Metallic Honeycomb: Orthotropic Rate-Independent Constitutive Model, *International Journal of Solids and Structures*, 41(16-17), 4435-4456.
- Mohr D. 2005. Mechanism-based multi-surface plasticity model for ideal truss lattice materials. *International Journal of Solids and Structures*, 42, 11–12, 3235–3260.
- Mohr D. 2005. On the role of shear strength in sandwich sheet forming. *International Journal of Solids and Structures*, 42(5-6), 1491-1512.
- Mohr D., Straza G. 2005. Development of formable all-metal sandwich sheets for automotive applications. *Advanced engineering materials*, 7 (4), 243-246.
- Mohr D. 2006. Multi-scale Finite-strain Plasticity Model for Stable Metallic Honeycombs Incorporating Microstructural Evolution, *International Journal of Plasticity*, 22(10), 1899-1923.
- Omerspahic E., Mattiasson K., Enqvist B. 2006. Identification of material hardening parameters by the three-point bending of metal sheets. *International Journal of Mechanical Sciences*, 48, 1525–1532
- Ortiz M., Popov E.P. 1983, Distortional hardening rules for metal plasticity, *J. Engrg. Mech*, 109, 1042-1057.
- Palkowski H., Lange G. 2007. Production and forming behavior of austenitic steel sandwich composites with a polymer core layer. *Materialwissenschaft und Werkstofftechnik*, 38, 2, 85-89.
- Papka S.D., Kyriakides S. 1994. Inplane compressive response and crushing of honeycomb. *Journal of the Mechanics and Physics of Solids*, 42, 10, 1499-1532.
- Parsa M.H., Nasher al ahkami S., Ettehad M. 2010, Experimental and finite element study on the spring back of double curved aluminum/polypropylene/aluminum sandwich sheet, *Materials and Design*, 31, 4174–4183
- Pearce R. 1991. *Sheet Metal Forming*. Adam Hilger, Bristol.
- Queheillalt D.T., Wadley H.N.G. 2005. Cellular metal lattices with hollow trusses. *Acta Mater*, 53, 303–313.
- Rébillat M. and Boutillon X. 2010. Identification of elastic and damping properties of sandwich structures based on high resolution modal analysis of point measurements, ISMA, Leuven, Belgium.
- Rébillat M., Boutillon X. 2011. Measurement of relevant elastic and damping material properties in sandwich thick plates. *Journal of Sound and Vibration*, 330, 6098–6121.
- Ridha M., Shim V.P.W. 2008. Microstructure and Tensile Mechanical Properties of Anisotropic Rigid Polyurethane Foam, *Experimental Mechanics*, 48(6), 63-776.
- Savoie J., Jonas J.J., MacEwen S.R., Perrin R. 1995. Evolution of r-value during the tensile deformation of aluminium. *Textures and Microstructures*, 23, 149–171.

- Seong D.Y., Jung C.G., Yang D.Y., Ahn J., Na S.J., Chung W.J., Kim J.H. 2010. Analysis of core shear stress in welded deformable sandwich plates to prevent de-bonding failure during U-bending, *Journal of Materials Processing Technology*, 210, 1171–1179
- Seong D.Y., Jung C.G., Yang D.Y., Kim J.H., Chung W.J., Lee M.Y. 2010. Bendable metallic sandwich plates with a sheared dimple core, *Scripta Materialia*, 63, 81–84.
- Seong D.Y., Jung C.G., Yang D.Y., Moon K.J., Ahn D.G. 2010. Quasi-isotropic bending responses of metallic sandwich plates with bi-directionally corrugated cores. *Materials and Design*, 31(6), 2804-2812.
- Shi Y., Sol H., Hua H. 2006. Material parameter identification of sandwich beams by an inverse method. *Journal of Sound and Vibration*, 290, 1234–1255.
- Simo J.C., Hughes T.J.R. 1998. *Computational Inelasticity*, Springer, Berlin.
- Stoughton T.B., Yoon J.W. 2009. Anisotropic hardening and non-associated flow in proportional loading of sheet metals. *Int. J. Plasticity*, 25, 1777–1817.
- Straza G.C.P. 2007. Formed core sandwich structure and method and system for making same, Patent US7648058.
- Tan P.J., Reid S.R., Harrigan J.J., Zou Z., Li S. 2005. Dynamic compressive strength properties of aluminium foams. Part 1—Experimental data and observations. *J. Mech. Phys. Solids*, 53, 10, 2174-2205.
- Tan P.J., Reid S.R., Harrigan J.J., Zou Z., Li S. 2005. Dynamic compressive strength properties of aluminum foams. Part II—‘shock’ theory and comparison with experimental data and numerical models. *J. Mech. Phys. Solids*, 53, 10, 2206-2230.
- Tokura S., Hagiwara I. 2010, A study for the influence of work hardening on bending stiffness of truss core panel, *Journal of Applied Mechanics*, 77(3), 1-6.
- Triantafyllidis N., Schraad M.W. 1998. Onset of failure in aluminum honeycombs under general in-plane loading. *J. Mech. Phys. Solids*, 46, 1089–1124.
- Vural M., Ravichandran G. 2003. Microstructural aspects and modeling of failure in naturally occurring porous composites, *Mechanics of Materials*, 35(3-6), 523-536
- Wicks N., Hutchinson J.W. 2001. Optimal truss plates. *International Journal of Solids and Structures*, 38, 5165-5183.
- Wierzbicki T., Abramowicz W. 1983. On the crushing mechanics of thin-walled structures. *Journal of Applied Mechanics-Transactions of the ASME*, 50, 4A, 727-734.
- Xue Z., Hutchinson J.W. 2004. Constitutive model for quasi-static deformation of metallic sandwich cores, *Int. J. Numer. Meth. Engng*, 61, 2205-2238.
- Xue Z., Vaziri A., Hutchinson J.W. ; 2005. Non-uniform hardening constitutive model for compressible orthotropic materials with application to sandwich plate cores. *Comput. Model. Eng. Sci.*, 10, 1, 79–96.
- Youssef S., Maire E., Gaertner R. 2005. Finite element modeling of the actual structure of cellular materials determined by X ray tomography. *Acta Materialia*, 53, 3,719–730.

- Zenkert D. 1995. An Introduction to Sandwich Construction, Engineering Materials Advisory Services Ltd, UK.
- Zupan M., Chen C., Fleck N.A. 2003. The plastic collapse and energy absorption capacity of egg-box panels, International Journal of Mechanical Sciences, 45, 851-871.